

UNIVERSITÉ DE GENÈVE

Département de Physique Nucléaire et Corpusculaire

Institute of Translational Molecular Imaging

FACULTÉ DES SCIENCES

Professeur Giuseppe Iacobucci

FACULTÉ DE MÉDECINE

Professeur Osman Ratib

---

# Development of the Thin TOF-PET Scanner Based on Fast Timing Monolithic Silicon Pixel Sensors

THÈSE

présentée à la Faculté des Sciences de l'Université de Genève  
pour obtenir le grade de Docteur ès Sciences, mention Physique

par

**Daiki Hayakawa**

de

Tokyo (Japon)

Thèse N°5433

GENÈVE

Atelier d'impression ReproMail

2020







**UNIVERSITÉ  
DE GENÈVE**

**FACULTÉ DES SCIENCES**

**DOCTORAT ÈS SCIENCES, MENTION PHYSIQUE**

**Thèse de Monsieur Daiki HAYAKAWA**

intitulée :

**«Development of the Thin TOF-PET Scanner Based on Fast  
Timing Monolithic Silicon Pixel Sensors»**

La Faculté des sciences, sur le préavis de Monsieur G. IACOBUCCI, professeur ordinaire et directeur de thèse (Département de physique nucléaire et corpusculaire), Monsieur R. OSMAN, professeur titulaire et codirecteur de thèse (Faculté de médecine, Institute of Translational Molecular Imaging (ITMI)), Monsieur O. RATIB, professeur (Département de médecine génétique et laboratoire, Hôpital Riviera-Chablais, Rennaz, Suisse), Monsieur F. SANCHEZ NIETO, professeur ordinaire (Département de physique nucléaire et corpusculaire), Madame A. SFYRLA, professeure assistante (Département de physique nucléaire et corpusculaire), Monsieur M. WEBER, professeur (LHEP - Laboratory for High Energy Physics, University of Bern, Switzerland), autorise l'impression de la présente thèse, sans exprimer d'opinion sur les propositions qui y sont énoncées.

Genève, le 29 janvier 2020

**Thèse - 5433 -**

**Le Décanat**



# Acknowledgements

First, I would like to express my gratitude to Prof. Giuseppe Iacobucci, for his support and guidance throughout everything of my PhD work.

I would like to express the deepest appreciation to Dr. Lorenzo Paolozzi, for his generous support of sensor developments. I owe my deepest gratitude to Dr. Emanuele Ripiccini, for his cooperation works of Monte-Carlo simulation and image reconstruction studies. Dr. Pierpaolo Valerio gives me constructive comments for my papers and my thesis regarding to electronics. Special thanks also to Fulvio Martinelli, Daniele Vitturini, Davide Ciucci, Dr. Francesco Di Bello, Ettore Zaffaroni and the other members in the TT-PET project, for their supports to my research activities. I also would like to offer my thanks to our secretary, Catherine Blanchard, for her kind helps.

Finally, I thank my family for their kind and continuous supports and encouragements.



# Contents

<b>1</b>	<b>Outline of the Thesis and Personal Contributions</b>	<b>1</b>
<b>I</b>	<b>The TT-PET Scanner</b>	<b>3</b>
<b>2</b>	<b>Positron Emission Tomography Imaging</b>	<b>5</b>
2.1	Positron Emission Tomography . . . . .	5
2.2	Hybrid Imaging . . . . .	6
2.3	Principles of PET imaging . . . . .	8
2.3.1	Annihilation Coincidence Detection . . . . .	8
2.3.2	Signal-to-Noise Ratio . . . . .	8
2.3.3	Time-of-Flight . . . . .	10
2.3.4	Spatial Resolution . . . . .	11
<b>3</b>	<b>The TT-PET Scanner</b>	<b>17</b>
3.1	Conventional PET Scanner . . . . .	17
3.2	Multi Layer Photon Detection with Pixel Sensor . . . . .	18
3.3	The Scanner Layout . . . . .	18
3.4	Data Acquisition and Trigger System . . . . .	23
<b>4</b>	<b>Expected Performance of the TT-PET scanner</b>	<b>25</b>
4.1	Simulation of the TT-PET Scanner . . . . .	25
4.1.1	Monte Carlo Simulation . . . . .	25
4.1.2	Hit Processing . . . . .	26
4.1.3	Coincidence Selection . . . . .	29
4.2	Simulation Results . . . . .	29
4.2.1	TOF Resolution . . . . .	29
4.2.2	Sensitivity . . . . .	29
4.2.3	Noise Equivalent Count Rate and Count Loss . . . . .	30
4.3	Image Reconstruction . . . . .	32

4.3.1	Iterative Reconstruction with a Statistical Model . . . . .	33
4.3.2	System Matrix with TOF information . . . . .	35
4.3.3	Maximum A Posteriori Probability Estimation . . . . .	35
4.3.4	Normalization . . . . .	37
4.3.5	Spatial Resolution . . . . .	38
4.3.6	Derenzo Phantom . . . . .	38
4.4	Discussion . . . . .	40

## **II Development of Annihilation Photon Detection with Fast Timing Monolithic Silicon Pixel Sensors 45**

### **5 Fundamental Semiconductor Sensor Properties 47**

5.1	Charged Particle Interactions in Matter . . . . .	47
5.1.1	Bethe-Bloch Formula . . . . .	47
5.1.2	$\delta$ Electron . . . . .	48
5.2	Semiconductor Physics and Devices . . . . .	49
5.2.1	Intrinsic Charge Carrier Concentration . . . . .	49
5.2.2	The pn-Junction . . . . .	49
5.2.3	Charge Carrier Transportation . . . . .	50
5.2.4	Avalanche Breakdown . . . . .	52
5.2.5	Guard Ring . . . . .	53
5.3	Time Resolution of Silicon Pixel Detectors . . . . .	53
5.3.1	Jitter . . . . .	55
5.3.2	Time Walk . . . . .	57
5.3.3	Charge Collection Noise . . . . .	58
5.3.4	Distortion . . . . .	58
5.3.5	TDC . . . . .	58
5.4	Semiconductor Technologies . . . . .	59
5.4.1	Amplifier . . . . .	59
5.4.2	Monolithic Process . . . . .	61
5.5	Sensor Design . . . . .	62
5.5.1	TCAD Simulation . . . . .	63
5.5.2	Physics Models and AC analysis . . . . .	63

### **6 Analog Prototype Developments 65**

6.1	Design . . . . .	65
6.1.1	TCAD Simulation for Guard Ring Design . . . . .	65
6.1.2	TCAD Simulation of Weighting Potential . . . . .	66

6.1.3	TCAD Simulation of Pixel Capacitance . . . . .	66
6.1.4	Layout of Analog Prototype Chip . . . . .	70
6.2	Measurement . . . . .	70
6.2.1	I-V Measurement of the Thin Chip . . . . .	71
6.2.2	Edge Laser TCT Measurement of the Un-thinned chip . . .	71
6.2.3	Electronics Performance with an External Sensor . . . . .	73
6.2.4	A Testbeam Experiment of the Un-thinned Chip . . . . .	73
6.3	Discussion . . . . .	79
<b>7</b>	<b>ASIC Demonstrator Development</b>	<b>81</b>
7.1	Design . . . . .	81
7.1.1	Layout . . . . .	81
7.1.2	Readout logic . . . . .	83
7.2	Measurement . . . . .	84
7.2.1	I-V Measurement . . . . .	84
7.2.2	A Testbeam Experiment . . . . .	86
7.3	Discussion . . . . .	90
<b>8</b>	<b>Characterization of the Annihilation Photon Detection System of the TT-PET Scanner</b>	<b>91</b>
8.1	Experimental Setup . . . . .	91
8.1.1	Detector . . . . .	91
8.1.2	$^{22}\text{Na}$ Source . . . . .	92
8.1.3	Experiment . . . . .	92
8.2	Annihilation Photon Detection Efficiency . . . . .	92
8.2.1	Measurement . . . . .	92
8.2.2	Simulation . . . . .	95
8.3	Time Resolution . . . . .	98
8.4	Discussion . . . . .	104
<b>9</b>	<b>Conclusions</b>	<b>105</b>
	<b>Appendix A Analytical Image Reconstruction</b>	<b>109</b>
	<b>Appendix B Simulation results of the tagged efficiency (ratio) with horizontal positions</b>	<b>111</b>
	<b>Bibliography</b>	<b>113</b>





# Abstract

The Thin-TOF PET (TT-PET) project aims at the construction of a small-animal PET scanner based on monolithic silicon pixel sensors with 30 ps time resolution for 511 keV photons, equivalent to 100 ps time resolution for minimum ionizing particles. The research work of this PhD thesis consisted in the design of the photon detection system and in the development and test of the fast monolithic sensor. Significant part of the activity was also dedicated to the study of the performance of the scanner and to the development of image reconstruction algorithms.

The iterative image reconstruction was developed using a maximum a posteriori probability estimation (MAPS) algorithm. Reconstructed images from Monte-Carlo data show high signal-to-noise ratio with unprecedented spatial resolution throughout the whole field of view of the scanner.

The detector ASICs were designed with the support of a Technology CAD simulation framework. The ASIC demonstrator, produced during this research activity and tested with minimum ionizing particles, shows a detection efficiency greater than 99.9% and a 130 ps (RMS) time resolution. A measurement setup based on a  $^{22}\text{Na}$  radioactive source showed that the single layer detection efficiency of the demonstrator chip for 511 keV photons is approximately 0.19%, which is in good agreement with the simulations. The same setup was used to measure the time resolution, that resulted to be 70 ps (RMS). This result, although excellent for a silicon sensor, is a factor two below the specification of the TT-PET project. It is created by a systematic error in the measurement of the charge that will be corrected in future chips.



# Résumé

Le projet Thin-TOF PET (TT-PET) vise à construire un scanner PET pour petits animaux basé sur des capteurs monolithiques à pixels au silicium avec une résolution temporelle de 30 ps pour 511 keV photons, équivalente à une résolution temporelle de 100 ps pour des particules au minimum d'ionisation. Les travaux de recherche de cette thèse ont porté sur la conception du système de détection de photons ainsi que sur la mise au point et le test d'un capteur monolithique rapide. Une partie importante de l'activité a également été consacrée à l'étude des performances du scanner et au développement d'algorithmes de reconstruction d'images.

La reconstruction d'images a été développée en utilisant une méthode du maximum a posteriori (MAPS). Les images reconstruites à partir de données générées par Monte-Carlo montrent un rapport signal sur bruit élevé avec une résolution spatiale sans précédent dans tout le champ de vision du scanner.

Les ASICs de détecteurs ont été conçus avec le support d'un framework de simulation Technology CAD. Le démonstrateur ASIC produit au cours de cette activité de recherche et testé avec des particules au minimum d'ionisation montre une efficacité de détection supérieure à 99,9% et une résolution temporelle sans précédent pour un capteur monolithique jusqu'à 130 ps (RMS). Une configuration de mesure basée sur une source radioactive de Na a montré que l'efficacité de détection de la couche unique de la puce de démonstration pour les photons de 511 keV est d'environ 0,19%, ce qui est en bon accord avec les simulations avec erreurs. La même configuration a été utilisée pour mesurer la résolution temporelle, qui s'est avérée être d'une résolution temporelle de 70 ps RMS. Ce résultat, bien qu'excellent pour un capteur au silicium, est un facteur deux inférieur aux spécifications du projet TT-PET. Il est créé par une erreur systématique dans la mesure de la charge qui sera corrigée dans les futures puces.



# List of Figures

2.1	Structural formulas of tracers . . . . .	7
2.2	Examples o hybrid imaging . . . . .	7
2.3	Illustrations of annihilation coincidence detections . . . . .	9
2.4	Illustration of backprojection . . . . .	9
2.5	Illustration of backprojection with/without TOF information . . . .	10
2.6	Positron momentum effects on intrinsic spatial resolution . . . . .	12
2.7	Spatial resolution due to detector resolution . . . . .	12
2.8	Effect of photon depth-of-interaction on spatial resolution . . . . .	14
2.9	Illustrations of DOI contribution to TOF . . . . .	15
3.1	Scintillation detector . . . . .	18
3.2	Multi layer structure of the TT-PET scanner . . . . .	19
3.3	CAD image of the TT-PET scanner . . . . .	20
3.4	CAD image of the TT-PET scanner inside a RF-coil . . . . .	20
3.5	CAD images of the tower and the cooling block . . . . .	21
3.6	CAD image of the super-module . . . . .	21
3.7	Design of the TT-PET chip . . . . .	22
4.1	The geometry of the TT-PET scanner in Geant4 toolkit . . . . .	27
4.2	Total energy deposits distribution . . . . .	28
4.3	The timing resolution of the pixel sensor as a function of total energy deposit . . . . .	28
4.4	Coincidence time resolution . . . . .	30
4.5	Sensitivity of the scanner . . . . .	31
4.6	Compton scattering in the same tower . . . . .	31
4.7	NECR of the scanner with cylindrical source . . . . .	32
4.8	NECR of the scanner with spherical source . . . . .	33
4.9	Backprojection with Siddon algorithm . . . . .	36
4.10	Normalization factor map . . . . .	39
4.11	Truth position distribution of annihilations for Derenzo Phantom .	40

4.12	Reconstruction of Derenzo phantom . . . . .	41
4.13	Reconstructed images without and with TOF informaion . . . . .	42
4.14	NECR of the Hyperion IID . . . . .	43
5.1	$\delta$ electron . . . . .	48
5.2	pn-junction . . . . .	51
5.3	Drift velocity as a function of electric field in silicon . . . . .	53
5.4	Breakdown voltage and field as a function of doping concentration for an abrupt pn-junction . . . . .	54
5.5	Schematic cross section of a sensor edge. . . . .	54
5.6	Schematic cross section of guard ring design . . . . .	55
5.7	Block diagram of front-end electronics . . . . .	56
5.8	Time over threshold . . . . .	56
5.9	Jitter effect on timing resolution . . . . .	57
5.10	Time walk effect . . . . .	59
5.11	A common-emitter NPN bipolar transistor . . . . .	60
5.12	Band gap of SiGe hetero junction bipolar transistor . . . . .	61
5.13	Working point of the SiGe-HBT for the TT-PET scanner . . . . .	62
6.1	Guard ring structure . . . . .	66
6.2	Multiple guard rings for the 1st ASIC demonstrator . . . . .	67
6.3	Weighting potential . . . . .	68
6.4	Simulation of bulk and inter-pixel capacitance as a function of voltage . . . . .	69
6.5	Layout of 1st ASIC demonstrator . . . . .	71
6.6	Current measurement as a function of voltage . . . . .	72
6.7	Setup of an edge laser TCT measurement. . . . .	73
6.8	A charge collection distribution of edge laser TCT measurements . . . . .	74
6.9	Threshold scan . . . . .	75
6.10	Charge deposition from a $^{90}\text{Sr}$ source . . . . .	75
6.11	Electric field of an un-thinned sensor . . . . .	77
6.12	Setup of a test beam measurement . . . . .	77
6.13	Efficiency map of 1st ASIC demonstrator . . . . .	78
6.14	Time walk correction using ToT information for the small pixel from the upstream sensor . . . . .	79
6.15	Time difference between the small pixel on upstream sensor and the LGAD sensor . . . . .	80
7.1	Layout of the 2nd ASIC demonstrator . . . . .	82
7.2	Modification of a guard ring structure around an innermost guard ring on the ASIC demonstrator . . . . .	82

7.3	Schematic cross section of p-Stop isolation . . . . .	83
7.5	Current measurement as a function of voltage for the ASIC demonstrator . . . . .	85
7.6	Setup at the test beam measurement . . . . .	87
7.7	Microscope picture of the 2nd ASIC demonstrator chip . . . . .	87
7.8	Efficiency map of the ASIC demonstrator chip . . . . .	88
7.9	Time walk correction using ToT information . . . . .	89
7.10	Time resolution (standard deviation) of the chip 1 . . . . .	89
8.1	Schematic cross section of the annihilation photon detection system.	93
8.2	$\beta^+$ decay scheme of the $^{22}\text{Na}$ . . . . .	93
8.3	Geometry of a $^{22}\text{Na}$ source . . . . .	93
8.4	Experimental setup of the annihilation photon detection. . . . .	94
8.5	Schematic design of the experimental setup of the annihilation photon detection system . . . . .	94
8.6	Pixel matrix for the efficiency measurement . . . . .	96
8.7	Hit distribution on chip 0 with the $^{22}\text{Na}$ source positioned at $z = 80\text{ }\mu\text{m}$	96
8.8	Annihilation photon detection efficiency measurement . . . . .	97
8.9	Visualization of the simulation setup of the annihilation photon detection system . . . . .	97
8.10	Simulation results of the annihilation photon detection efficiency . .	98
8.11	Pixel matrix for the timing measurement . . . . .	99
8.12	Time difference between chip 0 and chip 1 as a function of the status measured by the TDC ring oscillator on chip 1 . . . . .	99
8.13	Time-over-threshold distribution . . . . .	101
8.14	Two dimensional time walk correction . . . . .	102
8.15	Time difference between chip 0 and chip 1 after time walk correction	103
A.1	Reconstruction of Derenzo phantom with FBP model . . . . .	110
B.1	Simulation result of the annihilation photon detection efficiency . .	112
B.2	Simulation result of the annihilation photon detection efficiency . .	112





# List of Tables

2.1	Typical radio isotopes used for PET imaging. . . . .	6
4.1	Spatial resolution for four different radial positions at the center of the axial FOV. . . . .	38
4.2	Spatial resolution for four different radial positions at z=12.5 mm of the axial FOV. . . . .	39
4.3	Comparison with the conventional small animal PET-MRI scanners.	43
6.1	Measured time resolution for the analog prototype chip . . . . .	79
7.1	Efficiency of the three demonstrator chips . . . . .	86
7.2	Time resolution (standard deviation) of the three demonstrator chips	90
8.1	Time resolution (standard deviation) of the annihilation photon detection system . . . . .	104



# Chapter 1

## Outline of the Thesis and Personal Contributions

The Thin-TOF PET (TT-PET) project aims at the construction of a positron emission tomography (PET) scanner based on fast timing monolithic silicon pixel sensors.

The research contents are collaborative works with the members of the TT-PET project. The contributions of the author are summarized in the following outline of the thesis.

### Part I The TT-PET Scanner

The first part of the thesis reports on the study of the expected performance of the TT-PET scanner using Monte Carlo simulations. Principles and techniques of PET imaging are introduced in Chapter 2. In Chapter 3, the design of the TT-PET scanner are described. The expected performance of the TT-PET scanner is discussed based on results of Monte Carlo simulations and the reconstructed images from the simulation results in Chapter 4.

The author developed the image reconstruction algorithm. The author also contributed to the simulation studies, in particular to the design of the radioactive phantom, the computing system construction, and the validation of the simulation studies.

---

## Part II Development of Annihilation Photon Detection with Fast Timing Monolithic Silicon Pixel Sensors

On the second part of the thesis, the developments of annihilation photon detection with fast timing monolithic silicon pixel sensors are studied. In Chapter 5, semiconductor physics and fundamental properties of silicon sensor are described. Technology CAD (TCAD) simulations, which were used for the design of the silicon pixel sensor, are introduced.

The designs and the developments of the analogy prototype and ASIC demonstrator will be discussed in Chapter 6 and Chapter 7, respectively. The performance and the properties of the prototypes were characterized with a probe station, a laser, radio isotopes and hadron beams at CERN SPS facility. Chapter 8 is devoted to the characterization of the annihilation photon detection system of the TT-PET scanner with a  $^{22}\text{Na}$  radioactive source.

The author performed the TCAD simulation studies of the sensor and the characterization of the prototypes.

# Part I

## The TT-PET Scanner



## Chapter 2

# Positron Emission Tomography Imaging

In this chapter, purposes, principles and techniques of positron emission tomography imaging will be introduced.

The basic imaging method and the radio isotopes used for the imaging will be discussed in Chapter 2.1. Next, the hybrid imaging method with the other medical radiation diagnostic equipments will be introduced in Chapter 2.2. Finally, the principles of imaging techniques and the reconstructed image quality will be discussed in Chapter 2.3.

### 2.1 Positron Emission Tomography

Positron emission tomography (PET) is a nuclear medicine method used to study metabolic processes, by detecting pairs of photons produced by the annihilation in tissues of positrons emitted by a  $\beta^+$  tracer.

Radio isotopes which are typically used for PET imaging are summarized in table 2.1. For example, fluorodeoxyglucose ( $^{18}\text{F}$ -FDG), which is a widely used tracer in oncology, is produced by replacing one of the hydroxy groups with Fluorine-18 ( $^{18}\text{F}$ ) in glucose as shown in figure 2.1.  $^{18}\text{F}$ -FDG inside the body is absorbed by high-glucose-using cells the same as glucose, hence the distribution of the tracer represents the distribution of the metabolic activity of the cells. Since malignant cancer tends to capture more glucose than benign cancer, PET imaging is able not only to find the cancers but also to assess the malignancy of the cancers by integrating the distribution of the  $^{18}\text{F}$ -FDG [1]. PET imaging has been used in neurology for looking into metabolic process in a brain in order to study neural activity and to diagnose Alzheimer's disease [2]. Developments of a PET scanner

for small-animals has become active since efficacy of new drugs can be confirmed by in vivo imaging.

## 2.2 Hybrid Imaging

While PET imaging excels in obtaining functional information, it is difficult to obtain morphological information of tumors compared to computed tomography (CT) or magnetic resonance imaging (MRI). To address the issue, diagnostic system for acquiring PET images simultaneously with CT or MRI, called hybrid imaging, has been developed [3, 4]. An additional advantage of this device is that the morphological information of tumors obtained in CT or MRI can be used for attenuation and scattering correction of annihilation photons in PET image reconstruction.

In order to integrate PET with MRI (PET/MRI), PET detectors must be insensitive to high magnetic field from MRI and designed to not interfere with MRI imaging. Nevertheless, PET/MRI appears to be compelling since there are some advantages using MRI compared to CT as follows:

1. contrast for soft tissue in MRI image is higher than in CT image,
2. no radiation exposure in MRI,
3. functional information can be obtained by MRI as well as by PET.

Figure 2.2 shows the reconstructed images in PET/CT and PET/MRI. Thanks to the high contrast for soft tissue in MRI, the metabolic activity concentration is more clear in the PET/MRI image than in the PET/CT image.

Table 2.1: Typical radio isotopes used for PET imaging.

RI	Half-life	$\beta_{\max}^+$ energy	Target of imaging
$^{11}\text{C}$	20.4 min.	960 keV	Neuroreceptor distribution
$^{13}\text{N}$	9.96 min.	1.19 MeV	Local blood flow
$^{15}\text{O}$	123 sec.	1.72 MeV	Local blood flow, oxygen consumption
$^{18}\text{F}$	110 min.	635 keV	Glucose metabolism



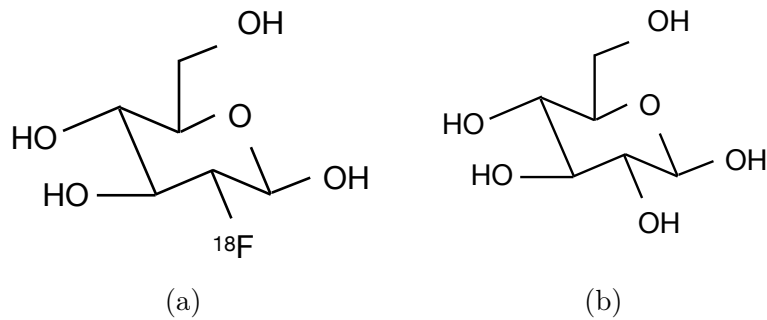


Figure 2.1: Structural formulas of  $^{18}\text{F}$ -FDG (a) and of Glucose (b)

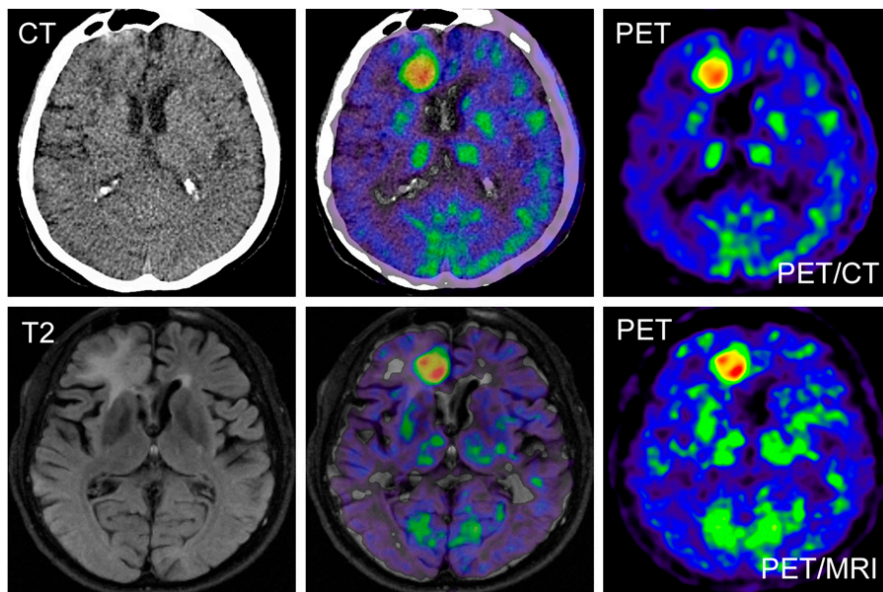


Figure 2.2: Examples of hybrid imaging (source: [5]). PET/CT (top) and PET/MRI (bottom) images of a patient with glioblastoma multiforme. PET/CT data: CT scan (left), corresponding fusion image (center), and  $^{11}\text{C}$ -methionine PET image (right). PET/MRI data: MRI image (left), fusion image (center), and PET image (right).

## 2.3 Principles of PET imaging

### 2.3.1 Annihilation Coincidence Detection

When a positron from a  $\beta^+$  tracer annihilates with an electron, their energies and masses are converted into a pair of annihilation photons. The photons have 511 keV energy and emitted simultaneously in opposite direction. The annihilation coincidence detection (ACD) mechanism, detecting the pair of annihilation photons, allows to localize the position of the emission along a line between the two detection points, which is called line-of-response (LOR). Typical PET scanners have a ring structure to surround the patient.

Since ACD mechanisms record any data within a specified coincidence timing window, background coincidences can occur within the resolving time of detector systems. Examples are described in figure 2.3 together with true coincidences. Scatter coincidences occur when one (or both) of the annihilation photons are scattered by Compton effect and the scattered photon is detected in a different detector from the one that was supposed to be hit. Random coincidences occur when two photons from two different annihilations are detected within the coincidence timing window and recorded as a single coincidence event.

### 2.3.2 Signal-to-Noise Ratio

PET images are reconstructed by projecting LORs to image elements; this operation is called backprojection. As shown in figure 2.4, the annihilation point is backprojected to the image elements with equal probability along the LOR. The backprojected image elements that do not contain the actual annihilation point contribute to the noise of the reconstructed image, hence the signal-to-noise ratio (SNR) of a reconstructed image has the following dependency:

$$\text{SNR} \propto n^{-\frac{1}{2}} , \quad (2.1)$$

where  $n$  is the number of image elements traversed by LORs.

Besides, each image element has a statistical uncertainty that depends on the number of true coincidences. The statistical error also contributes to the SNR of the reconstructed images. The contribution is approximated by

$$\text{SNR} \propto \sqrt{\text{NEC}} , \quad (2.2)$$

where NEC (noise equivalent counts) is an indicator that evaluates the effective statistical accuracy of the data [6]. The NEC is given by:

$$\text{NEC} = \frac{T^2}{T + S + R} , \quad (2.3)$$

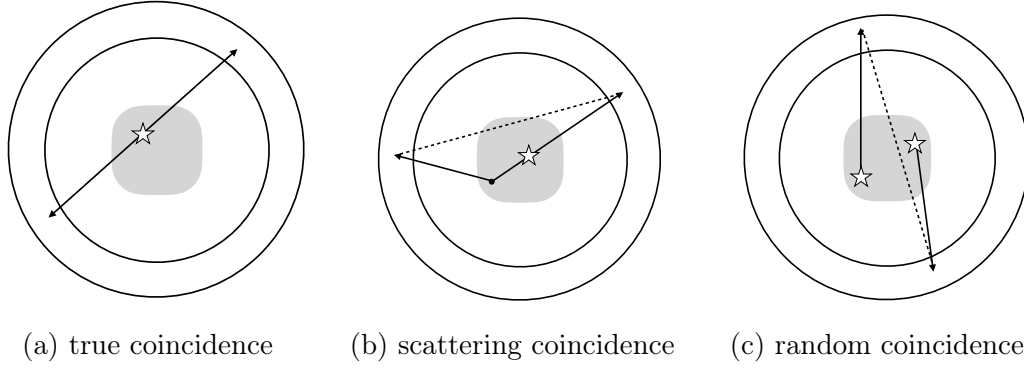


Figure 2.3: Illustrations of annihilation coincidence detections: true coincidence (a), scattering coincidence (b), and random coincidence (c). The stars represent annihilation points, arrows represent path of annihilation photons and dashed lines represent reconstructed LORs. As dashed lines do not traverse annihilation points, scattering and random coincidences generate uniform background on reconstructed images.

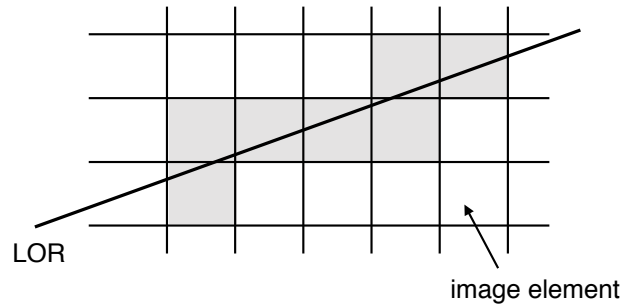


Figure 2.4: Illustration of backprojection. The annihilation point on LOR is backprojected to image elements with equal probability along the LOR.

where  $T$  represents the number of true coincidences,  $S$  are the scattered coincidences and  $R$  are the random coincidences.

According to equation 2.1 and equation (2.2), SNR of a reconstructed image can be represented by

$$\text{SNR} \propto \sqrt{\frac{\text{NEC}}{n}}, \quad (2.4)$$

which represents the effective statistical accuracy of the data in each image element.

### 2.3.3 Time-of-Flight

The time-of-flight (TOF) information of the photon detection gives position sensitivity along the LOR, hence the number of image elements involved in backprojection with TOF information is smaller than without TOF information as shown in figure 2.5. According to equation (2.4), the Signal-to-Noise Ratio (SNR) of the reconstructed images improves as follows:

$$\frac{\text{SNR}_{\text{TOF}}}{\text{SNR}_{\text{CONVENTIONAL}}} \sim \sqrt{\frac{D}{\Delta x}} = \sqrt{\frac{2D}{c\Delta t}}, \quad (2.5)$$

where  $D$  is the diameter of the scanner,  $\Delta x$  is the full width at half maximum (FWHM) of the the position resolution along the LOR and  $\Delta t$  is the FWHM of the coincidence time resolution, which is a distribution of the time difference between two hits in coincidence [7].

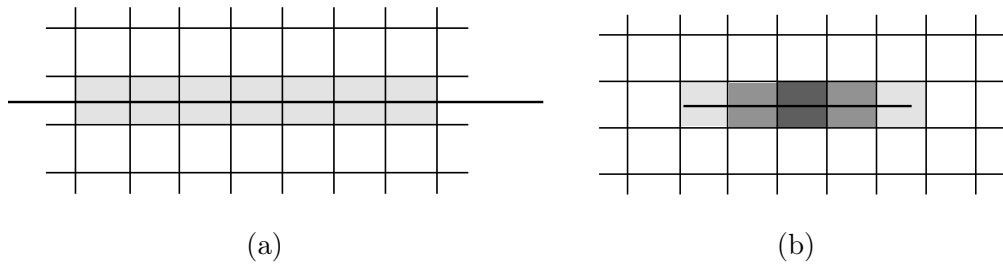


Figure 2.5: Illustration of backprojection without TOF information (a) and with TOF information (b). The LOR with TOF information is backprojected with a gaussian distribution.

### 2.3.4 Spatial Resolution

The spatial resolution of a reconstructed image is an important parameter to evaluate the ability to distinguish two objects in the image.

The intrinsic spatial resolution  $\Gamma$  [mm] (FWHM) for a point source located at the position  $r$  from the center along the radius of the scanner is given by

$$\Gamma = C \sqrt{\sigma_{\text{positron}}^2 + \sigma_{\text{detector}}^2} , \quad (2.6)$$

where  $C$  ( $\sim 1.25$ ) is a commonly used empirical multiplicative factor to describe an additional blur due to a reconstruction algorithm [8],  $\sigma_{\text{positron}}$  is determined by the momentum of the positron and  $\sigma_{\text{detector}}$  is determined by the spatial resolution of the photon detection sensor. These effects will be discussed individually in the following chapters.

#### Positron Momentum Effect

Since a positron emitted from a  $\beta^+$  tracer has some momentum, the spatial resolution  $\Gamma$  can be degraded by two factors related to the emission and the annihilation of the positron, as shown in figure 2.6.

The first factor is due to the positron path in the organic tissue before the annihilation, which is called positron range effect. The positron range  $s$  depends on its momentum. According to a Monte Carlo study, the FWHMs of the extrapolated positron distributions in water are 0.1 mm and 0.5 mm for  $^{18}\text{F}$  ( $E_{\beta}^{\text{max}} : 635 \text{ keV}$ ) and  $^{15}\text{O}$  ( $E_{\beta}^{\text{max}} : 1.72 \text{ MeV}$ ), respectively [9].

The second factor is due to the non-collinearity of the annihilation photons. For the point source located at the center of the scanner, the effect on the spatial resolution is approximated to  $0.0022D$ , where  $D$  is the diameter of the scanner, expressed in cm. The effects for a small-animal PET scanner ( $D \sim 4 \text{ cm}$ ) and a whole-body PET scanner ( $D \sim 80 \text{ cm}$ ) are approximately 0.1 mm and 1 mm, respectively.

Finally,  $\sigma_{\text{positron}}$ , expressed in cm, in equation (2.6) is given by

$$\sigma_{\text{positron}}^2 \sim (0.0022D)^2 + s^2 . \quad (2.7)$$

#### Detector Resolution

The FWHM of the spatial resolution due to the detector precision for a point source at the center of the scanner is given by

$$\sigma_{\text{detector}} \sim \frac{d}{2} , \quad (2.8)$$

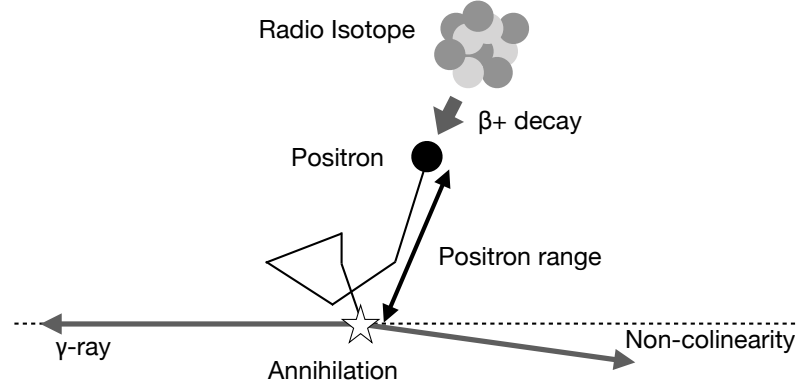


Figure 2.6: Positron momentum effects on intrinsic spatial resolution. The positron emitted from the radioisotope by  $\beta^+$  decay may travel before the annihilation. The non-colinearity of the annihilation photons arises when the positron is not at rest when it annihilates.

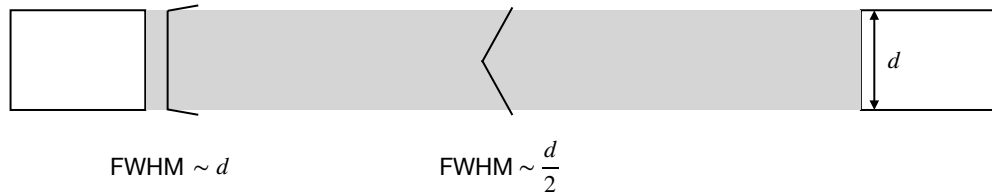


Figure 2.7: Spatial resolution due to detector resolution.  $d$  is the width of the detector and the shaded region shows the uncertainty of the LOR. The coincidence response function is a triangle with FWHM of approximately  $d/2$  at middle since both detectors contribute the spatial resolution, while the shape of the response function becomes a rectangle of width  $d$  as the source is moved closer to the one of the detectors [10].

where  $d$  is the width of the detector, as shown in figure 2.7.

As illustrated in figure 2.8, the uncertainty of the photon depth-of-interaction (DOI) degrades the spatial resolution when the annihilation does not occur at the center of the scanner. The apparent width  $d'$  is represented by

$$d' = d \cos \theta + x \sin \theta , \quad (2.9)$$

where  $x$  is uncertainty of the DOI and  $\theta$  is the angle between the LOR and the detector. The FWHM of the spatial resolution  $\sigma_{\text{detector}}$  in equation (2.7) is modified to

$$\sigma_{\text{detector}} \sim \frac{d'}{2} \quad (2.10)$$

$$= \frac{d}{2} \left( \cos \theta + \frac{x}{d} \sin \theta \right) . \quad (2.11)$$

For an annihilation at  $\theta = 30^\circ$ , the spatial resolution is degraded to factor 3.4 with  $x/d \sim 5$ , while there is no degradation with  $x/d \sim 0.5$ . In addition, a precise measurement of the DOI contributes to reducing the error of TOF measurements as well as the spatial resolution as shown in figure 2.9.

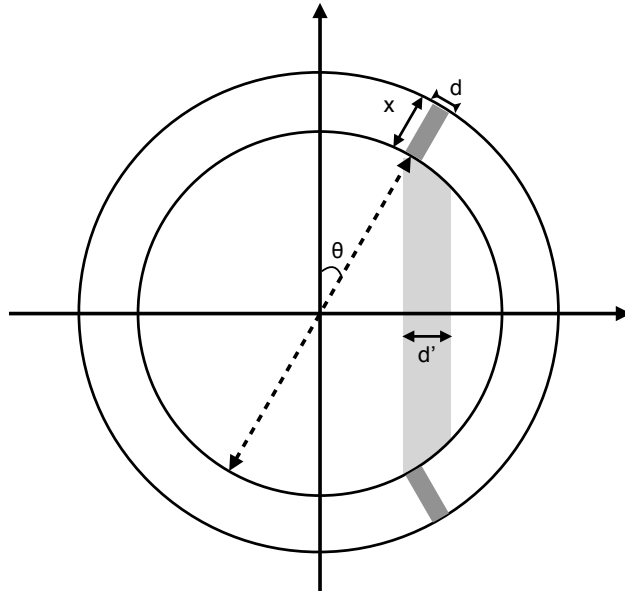


Figure 2.8: Effect of photon depth-of-interaction on spatial resolution.  $d$  represents the detector width and  $x$  represents a detector depth. The apparent detector width  $d'$  depends on the position along the radial coordinate of the scanner as well as the detector resolution:  $d$  and  $x$ .



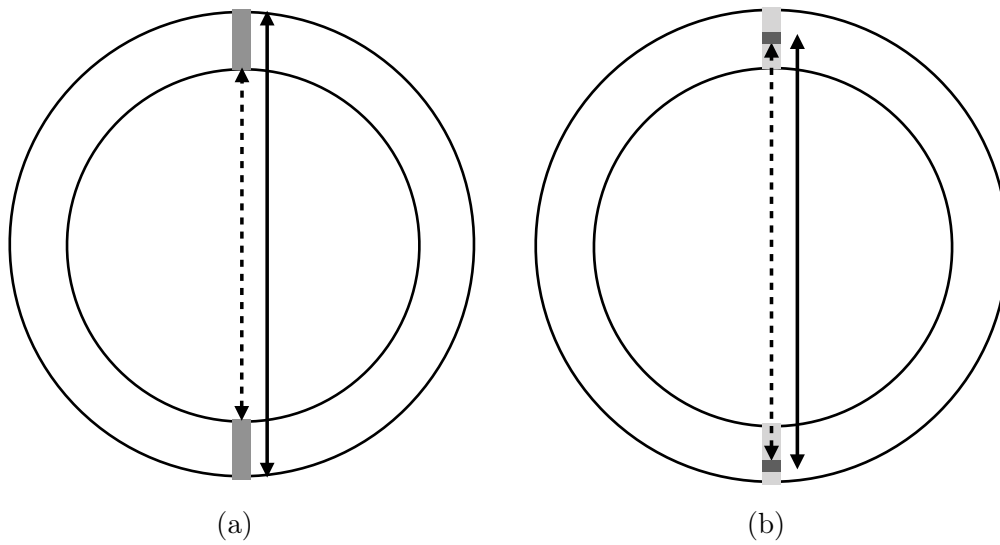


Figure 2.9: TOF uncertainty without DOI (a) and with DOI (b). The dashed line represents the minimum length of the LOR and the solid line represents the maximum length of the LOR. The difference of the two lines contribute to the uncertainty of the TOF information. A precise measurement of the DOI contributes to reducing this uncertainty.



# Chapter 3

## The TT-PET Scanner

The Thin TOF-PET (TT-PET) project [11] aims at the construction of a small-animal PET scanner, meant to be inserted in an existing MRI scanner. As discussed in Chapter 2, the targets of the small-animal PET scanner are summarized as follows:

1. The detector must be insensitive to the high magnetic field from the MRI scanner.
2. The scanner must be thin to be inserted in the existing MRI scanner.
3. The detector must have excellent time resolution for the TOF information of the photon detection and for the random coincidence removal.
4. Small detective volumes to obtain high spatial resolution (target: less than 1 mm).
5. The scanner has the sensitivity for the photon DOI to avoid the degradation of the spatial resolution throughout the whole field of view of the scanner.

### 3.1 Conventional PET Scanner

Figure 3.1 shows a conventional method of photon detection using a scintillation detector, which consists of a scintillating crystal and a photon detector. The scintillation detector is used for conventional PET scanners, but there are some issues for small-animal PET/MRI scanners:

1. The size of the crystal is limited due to the size of the photon detectors. The minimum detector width  $d$  achievable is  $\mathcal{O}(1)$  mm.

2. It is difficult to reduce the uncertainty on the DOI due to the thickness of the crystal, which is typically larger than 1 cm.
3. TOF resolution for the conventional scanners are  $\mathcal{O}(100)$  ps, hence no gain for SNR of reconstructed images.

### 3.2 Multi Layer Photon Detection with Pixel Sensor

A multi layer structure with pixel sensors was developed for the TT-PET scanner to overcome the issues of the scintillation detector. As illustrated in figure 3.2, electrons converted from annihilation photons in the lead layers (50  $\mu\text{m}$  thick) are detected in silicon monolithic pixel sensors (100  $\mu\text{m}$ ) [12]. The granularity of the detector is 500  $\mu\text{m}$  for the detector width and 220  $\mu\text{m}$  for the detector depth. Therefore, much better than 1 mm spatial resolution is expected for whole view of the scanner. The target for the time resolution of the silicon monolithic pixel sensor is 30 ps for 511 keV photons, which corresponds to a coincidence time resolution of approximately 80 ps FWHM. The expected gain for SNR of a reconstructed image in (2.5) is approximately 1.7 with the distance between the annihilation photon detectors  $D = 3.6$  cm and 2.6 with  $D = 8.4$  cm.

### 3.3 The Scanner Layout

Figure 3.3 shows the CAD image of the TT-PET scanner. The scanner is composed of 16 wedge-shaped detectors, called towers, and 16 ceramic cooling blocks in a

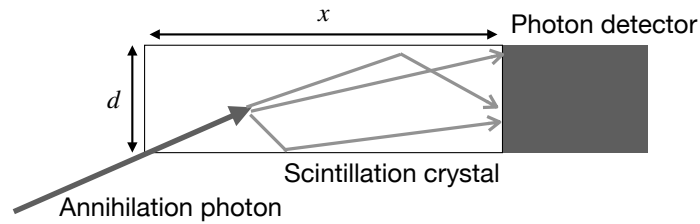


Figure 3.1: Scintillation detector. Annihilation photons are converted to visible photon in the scintillation crystal and the visible photons are collected by the photon detector. The detector width  $d$  and the depth  $x$  contribute to the spatial resolution of the scanner.

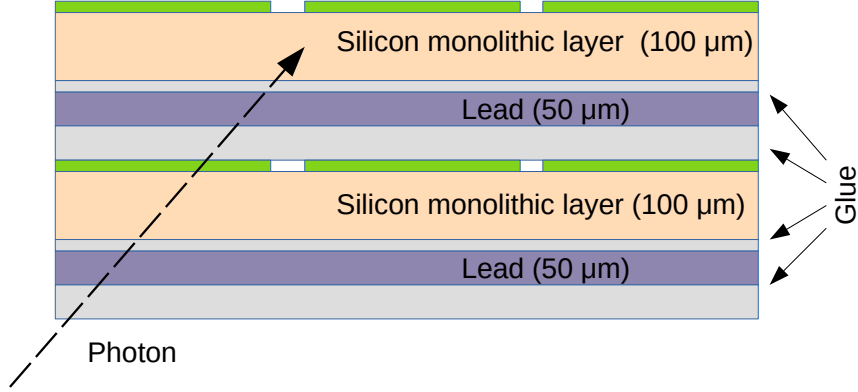


Figure 3.2: Multi layer structure of the TT-PET scanner. 2 detection layers and annihilation photons are illustrated. Each layer is formed by a lead foil for photon conversion, a dielectric spacer, adhesive tapes and a silicon monolithic pixel sensor.

cylindrical structure. The scanner can be inserted in the removable RF-coil of the nanoScan 3T MRI [13] as shown in figure 3.4. Readout electronics, power supplies and cooling services are isolated from the MRI, and the electronics are connected to the readout and power distribution by long flat shielded Kapton cables.

Figure 3.5 shows the CAD images of the tower and the cooling block. The tower is made of 12 super-modules, corresponding to 60 detection layers. The super-modules have 3 different widths, hence the tower is in the shape of a wedge. The ceramic cooling block is designed to dissipate the power from the monolithic silicon pixel sensors (approximately 20 W for a tower).

A super-module consists of 5 detection layers, as shown in figure 3.6. The 5 detection layers are interconnected by wire-bonding to the flex PCB for the signal processing and the high voltage (HV)/low voltage (LV) distribution.

The monolithic silicon layer is made of 2 ASIC chips in the axial direction. Each ASIC chip has  $12 \times 48$  (innermost),  $16 \times 48$  (middle) and  $20 \times 48$  (outermost) pixels with a size of  $500 \times 500 \mu\text{m}^2$ , front-ends, logic, TDCs and I/O pads as described in figure 3.7. The total number of the pixels in the scanner is 1'474'560.

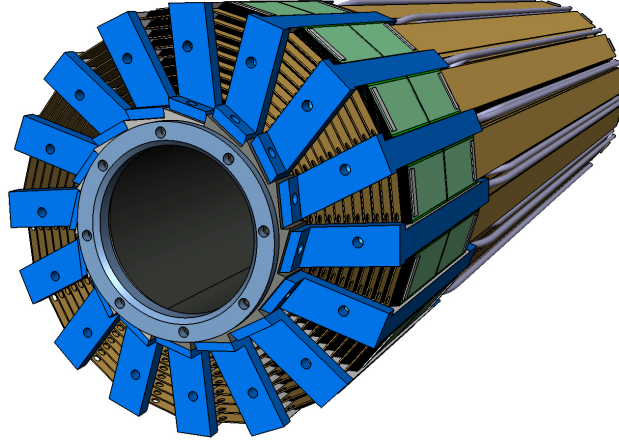


Figure 3.3: CAD image of the TT-PET scanner. 16 pairs of towers and cooling blocks with cylindrical structure consist of the scanner. The cylindrical shape of the carbon fiber, 3.6 cm diameter and 300  $\mu\text{m}$  thickness, is inserted in the scanner for the mechanical support. The external diameter of the scanner is 8.4 cm and the axial length of the area (yellow green), where annihilation photons can be detected, is approximately 5 cm.

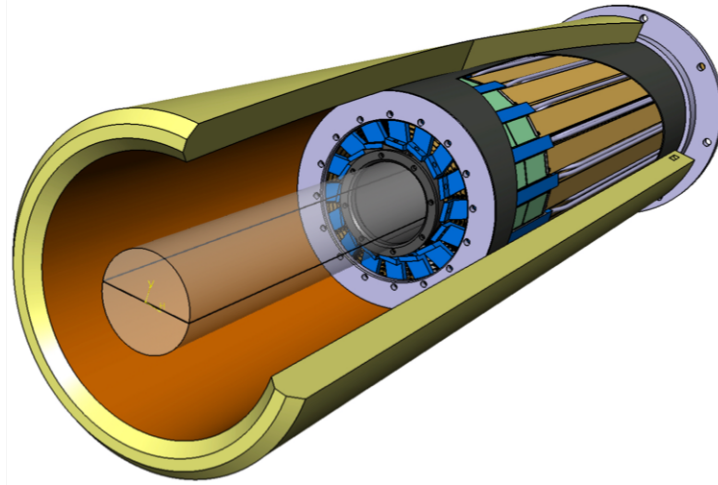


Figure 3.4: CAD image of the TT-PET scanner inside a RF-coil. Cooling and electrical services, not shown in the image, are connected by cooling pipes and Kapton flat cables, respectively.

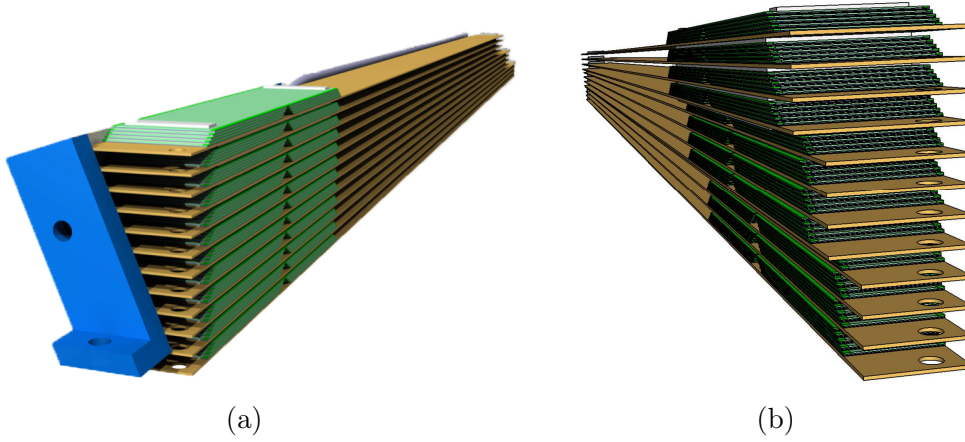


Figure 3.5: CAD images of the tower and the cooling block. The tower (green and brown) with the cooling block (blue) (a) and the tower without the cooling block (b). The wedge-shaped structure of the tower is sub-divided into 12 super-modules, which have 3 different transverse widths. The widths are 7, 9 and 11 mm for the innermost, the middle and the outermost 4 super-modules, respectively.

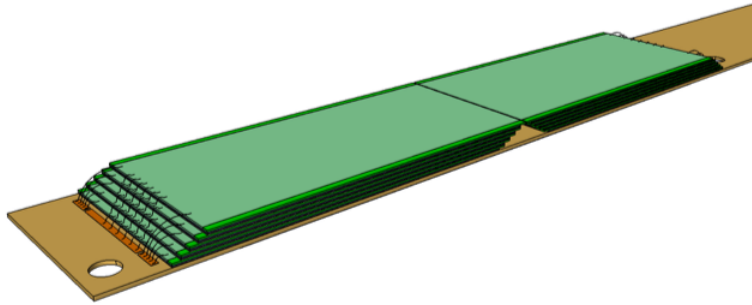


Figure 3.6: CAD image of the super-module. The 5 detection layers (green) are connected to a flex PCB (brown) at the bottom via wire bonds. The hole on the flex PCB is designed for the geometrical alignment. The monolithic silicon layer is made of 2 ASIC chips in the longitudinal direction.

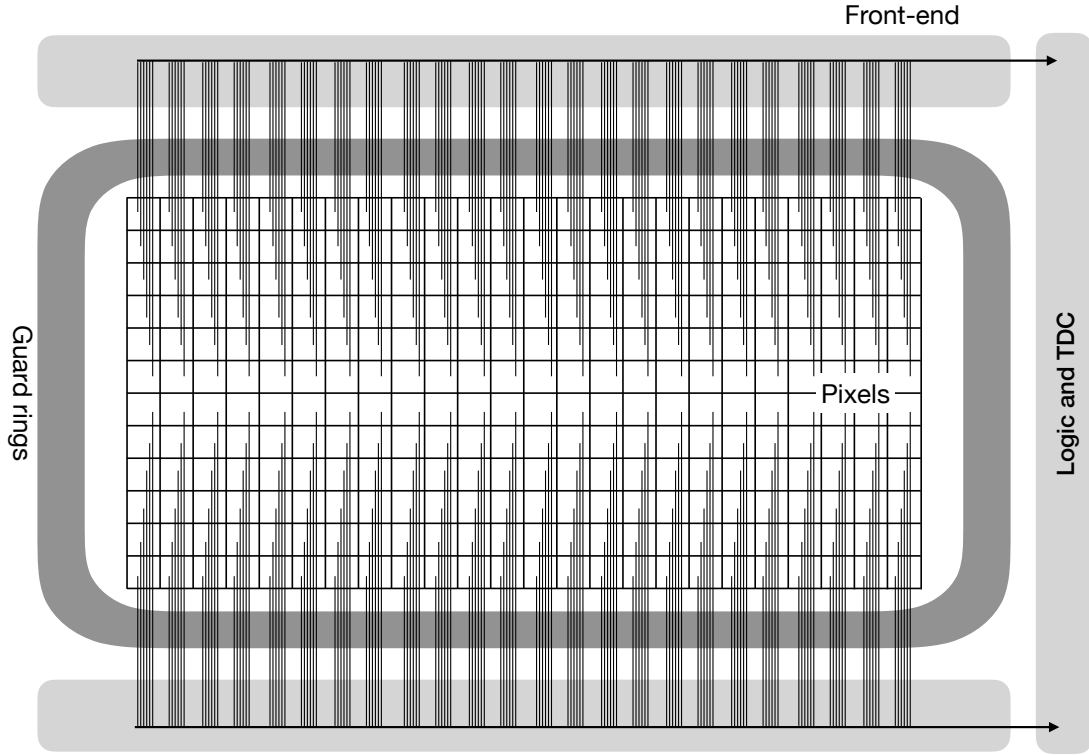


Figure 3.7: Design of the TT-PET chip (innermost). Signals from the  $12 \times 48$  pixels are routed to the front-ends in the longitudinal region outside of the guard rings. Amplified and digitized signal are sent to the logics and TDCs to the right side in the illustration. I/O pads are distributed on the right periphery in the chip for the wire-bonding.



### 3.4 Data Acquisition and Trigger System

The dedicated data acquisition (DAQ) is designed to readout data without any count loss for a 50 MBq source at the center of the scanner [14]. The DAQ system is divided into 3 stages. In the first stage, each tower, corresponding to 12 super-modules, is connected to a tower control (TC) board by Kapton flat cables. The role of the TC boards is temporary data storage/suppression, 8b10b encoding [15] and HV/LV operation for the silicon pixel sensors. In the second stage, the 16 TC boards are connected to a multiplexer board, called Versatile Link Demo Board (VLDB). The VLDB supplies the synchronization L1 clock to the TC boards, multiplexes the electrical signal from the TC boards to a single bit stream, and converts it to an optical signal. In the third stage, the optical signal is sent to a Central Trigger Processor (CTP) by an optical fiber. The CTP organizes the whole DAQ system and supplies the synchronization L0 clock.

The readout system can be run in data-driven mode, where each hit information is immediately sent to the TC boards, or in triggered mode, where hits are stored in a local buffer and are sent out only after a request from CTP.



## Chapter 4

# Expected Performance of the TT-PET scanner

A full Monte Carlo simulation of the TT-PET scanner and image reconstruction were developed to evaluate its performance.

The purpose of the study is to assess the performance of the scanner according to the standard methods for small-animal PET scanner [16] and to develop image reconstruction algorithms. Furthermore, the advantages and the characteristics of the TT-PET scanner in comparison with the conventional PET scanners will be discussed based on the simulation results and the reconstructed images.

The setup of the simulation will be described in Chapter 4.1 and the results of the simulation will be presented in Chapter 4.2. The development of the image reconstruction will be discussed in Chapter 4.3. Finally, the comparison with other small-animal PET scanners will be discussed in Chapter 4.4.

### 4.1 Simulation of the TT-PET Scanner

The material and the geometry of the multilayered structure for photon detection had been optimized by FLUKA [17] simulation with a pencil 511 keV photon beam perpendicularly incident on a tower. The prior study using Monte Carlo simulation by collaboration member shows that 50  $\mu\text{m}$  lead maximize the detection efficiency of 511 keV photons ( $\sim 27\%$ ) [18].

#### 4.1.1 Monte Carlo Simulation

A full Monte Carlo simulation was performed using GEANT4 toolkit [19] to evaluate the performance of the TT-PET scanner. GEANT4 is a toolkit developed by

CERN for the simulation of the passage of particles through matter using Monte Carlo methods. The toolkit is written object oriented in C++ and supports parallel computing so as to construct detectors flexibly in a simulation and to compute a variety of physical calculations at high speed. Originally developed for high energy physics, it can be applied to space science and medical physics, and it is used for development of various PET scanners.

## The Scanner and Phantoms

The geometry of the TT-PET scanner was precisely reproduced, as shown in figure 4.1.

Several different phantoms were used to study the expected performance of the scanner. The phantoms are made by filling radioactive water to holes in acrylic cylinder.  $^{18}\text{F}$  or  $^{22}\text{Na}$  were used as radionuclides.

## Physics

The GEANT4 EMStandard\_opt4 physics list was used to calculate interaction between photons, electrons or positrons and matters. In addition, thresholds on secondary particle productions were modified from default (0.07 mm) to 0.01 mm for photons and electrons to perform precise calculation for  $\delta$ -electrons in the silicon sensor<sup>1</sup>. Magnetic field from MRI was not reproduced in the simulation since the effect for scanner performance is expected to be negligible thanks to the insensitivity of silicon sensors to the magnetic field.

### 4.1.2 Hit Processing

The truth information of the interactions in the scanner regarding to position, time and energy deposits in the pixel sensor was reprocessed by adding the expected detector response.

## Source Intensity

In the Geant4 simulation, a disintegration of each radionuclide element in the source was simulated. The time interval between two disintegrations is distributed as  $e^{-It}$ , where  $I$  is the intensity of the source. The lifetime of the radionuclide was not implemented.

---

<sup>1</sup>SetCuts() method was used in ConstructProcess() to modify the threshold

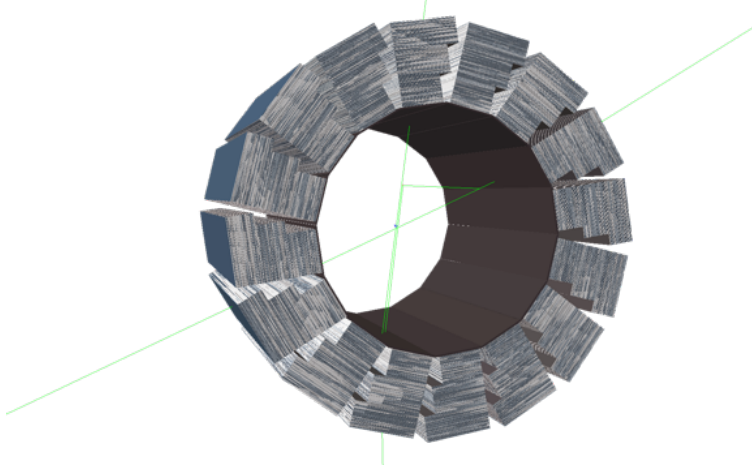


Figure 4.1: The geometry of the TT-PET scanner in Geant4 toolkit.

### Energy Deposits

The total energy deposit ( $E_{dep}$ ) in each pixel sensor was calculated by summing energy deposits of every interactions in the pixel sensor. Figure 4.2 shows the distribution of the total energy deposited in a pixel sensor. If the total energy deposit is larger than 20 keV, the pixel is regarded as "hit".

### Position

The real position of the hit was transformed to the center of gravity of the pixel sensor.

### Timing

A time smearing by gaussian function was applied to the time information according to the following expected time resolution of pixel sensor:

$$\sigma_t = \sigma_t^0 \frac{E_{dep}^{MIP}}{E_{dep}}, \quad (4.1)$$

where  $\sigma_t^0$  is the measured value ( $\sim 100$  ps) and  $E_{dep}$  is the most probable energy deposit value for minimum ionizing particles passing through pixel sensors. The  $\sigma_t$  as a function of the energy deposits obtained by the Geant simulation is shown in figure 4.3.

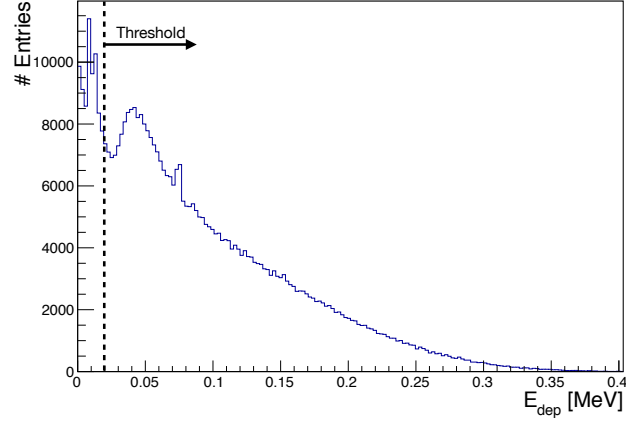


Figure 4.2: Total energy deposits distribution in the sensor.

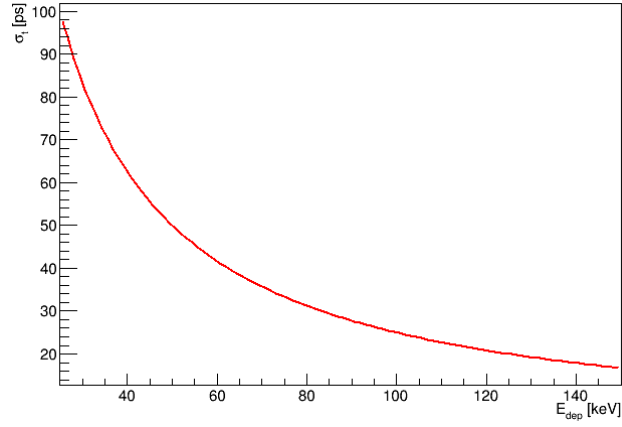


Figure 4.3: The timing resolution of the pixel sensor as a function of total energy deposits.

## Dead Time of the data acquisition system

The dead time of the data acquisition system in a data-driven mode was introduced.  $2\mu\text{s}$  was set to the time it takes to transfer the hit information from the super-modules to tower control and 8-state buffer per chip was taken into account.  $40\text{ ns}$  was also set to the dead time of the tower control systems, which corresponds to the time it takes to send one hit to the aggregator. Every hit during the dead time in the corresponding systems were discarded.

### 4.1.3 Coincidence Selection

After the hit processing, coincidence selection was done to distinguish true coincidences from random coincidences. The maximum time difference between the two hits is:

$$\frac{2R_{\text{ext}}}{c} \sim 260\text{ ps} , \quad (4.2)$$

where  $R_{\text{ext}}$  represents the external radius of the scanner and  $c$  is light speed. A  $500\text{ ps}$  coincidence window was chosen to take the time resolution of the pixel sensor into consideration. The LOR passed the coincidence selection was required to intercept the phantom.

## 4.2 Simulation Results

### 4.2.1 TOF Resolution

Figure 4.4 shows the TOF distribution of coincidences with a point-like  $^{18}\text{F}$  source in an acrylic cube of size  $10\text{ mm}$ , which corresponds to the expected coincidence time resolution approximately. The phantom was put in the center of both the axial and the transversal field of view of the scanner. The FWHM of the distribution is approximately  $80\text{ ps}$ , corresponding to  $34\text{ ps}$  gaussian standard deviation. The long tail in the TOF distribution is due to the Compton interaction in the scanner, which produces larger time uncertainty due to the low energy deposit in the sensors as described in equation (4.1).

### 4.2.2 Sensitivity

A spherical source of  $^{22}\text{Na}$  with radius  $0.3\text{ mm}$ , embedded in an acrylic cube of  $10\text{ mm}$  extent on all sides, was used to study the sensitivity of the scanner to the true coincidence photons. The activity of the source was fixed to  $1\text{ MBq}$  so that

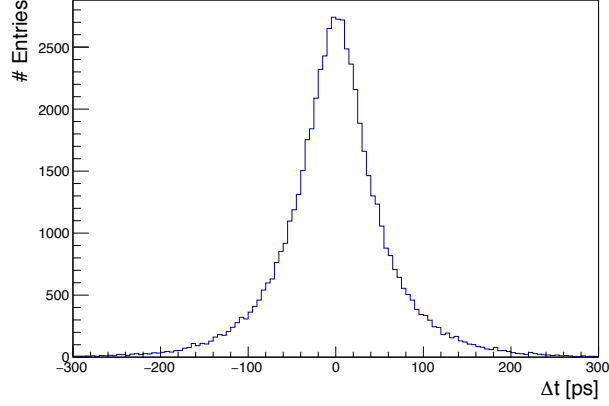


Figure 4.4: Coincidence time resolution. The 70 ps (FWHM) time resolution is expected.

the count losses and random events are suppressed enough. The source had been placed in 49 different positions along the axial direction with 1 mm intervals. The sensitivity was calculated by dividing the number of coincidence photons passed the selection criteria into the number of  $^{22}\text{Na}$  decay in each source position. Figure 4.5 shows the expected sensitivity of the scanner as a function of the position along the axial field of view. A maximum sensitivity of approximately 4% is expected.

### 4.2.3 Noise Equivalent Count Rate and Count Loss

The relative system sensitivity to scattered radiation and the effects of system dead time and the generation of random coincidence events were evaluated at several different intensity of source activity. Noise equivalent count rate (NECR) was calculated following to equation (2.3).

The true Monte Carlo information was used to tag random and scattered events to the selected coincidences. Fake coincidences due to multiple hits in the same layer or in the same tower are also included into the random coincidences. The first case is caused by electrons traveling through multiple pixels, while the second case is due to the Compton scattering in the same tower as shown in figure 4.6.

Two different geometry of mouse-like sources were used for the study. Figure 4.7 shows the coincidence rates, NECR and count loss with a cylindrical source of  $^{18}\text{F}$  with 1.6 mm in radius and 50 mm long, located to the central axis at the radial distance of 10 mm in an acrylic phantom with a radius of 12.5 mm and 50 mm long.

A spherically distributed source of  $^{18}\text{F}$  with radius 5 mm encapsulated in an



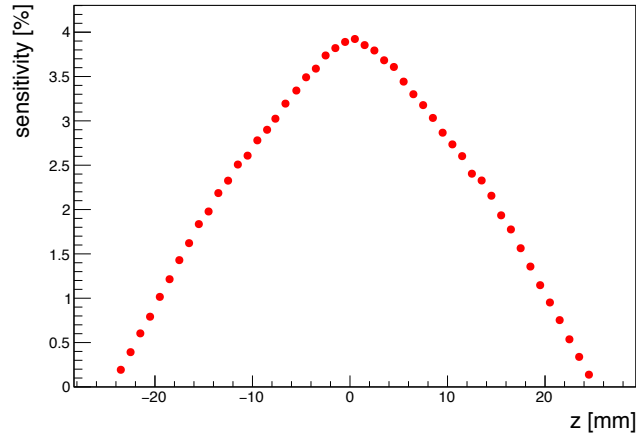


Figure 4.5: Sensitivity of the scanner.

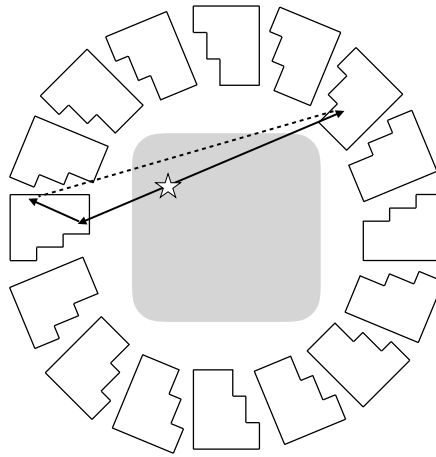


Figure 4.6: Compton scattering in the same tower. The fake coincidence, represented by the dashed line, are included into the random coincidence.

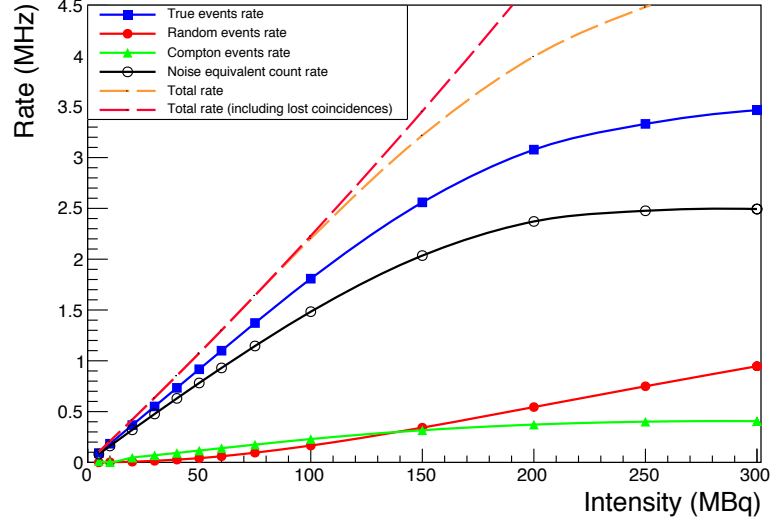


Figure 4.7: NECR of the scanner with cylindrical source.

acrylic cube of 10 cm extent on all sides, located in  $x = 0$ ,  $y = -5$  mm,  $z = 10$  mm was also studied. In addition to the coincidence selection discussed in Chapter 4.1.3, only LORs that intercepted a circle in the  $xy$  plane of radius 8 mm centered in  $x = 0$  and  $y = -5$  mm and  $|z_m - z_s| < 16$  mm, where  $z_m$  is the average point of the projection of the line of response along the axial view and  $z_s$  is the position of the source along the axial view. The result with the spherical source is shown in figure 4.8

### 4.3 Image Reconstruction

Analytical image reconstruction based on a filtered back projection (FBP) model [20] has a problem regarding to the artifacts due to the detector acceptance and statistical noise (see Appendix A). Therefore, a statistical image reconstruction algorithms based on an iterative method were developed. If the algorithms are based on a statistical model including the acceptance of the detector and the statistical effects, the images without those artifacts are expected to be reconstructed.

Customizable and Advanced Software for Tomographic Reconstruction (CAS-ToR) framework<sup>2</sup> [21] is a customizable open-source software and it supports iter-

<sup>2</sup>Version: 2.0.2

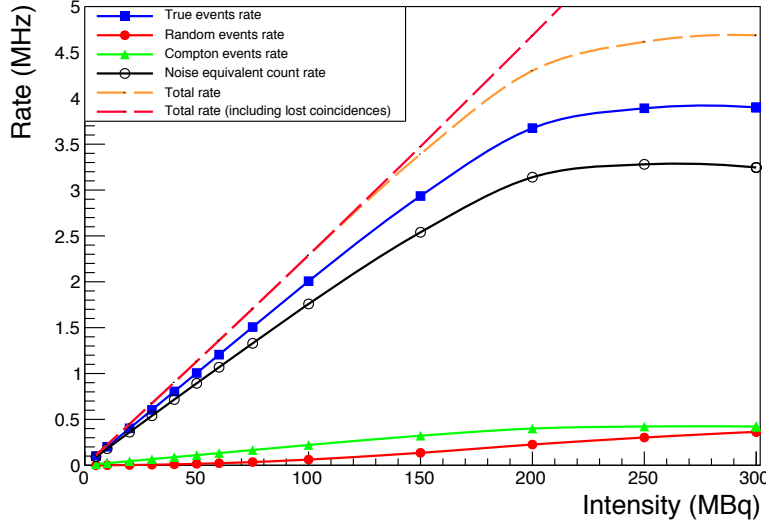


Figure 4.8: NECR of the scanner with spherical source.

active reconstruction with a statistical model and a parallel computing with open MP [22] (multi-threads) library to be practical for computing time. A standard iterative reconstruction algorithm, list-mode maximum likelihood expectation maximization (LM-MLEM) algorithm, will be presented in Chapter 4.3.1. Since the TT-PET scanner has high granularity, images were reconstructed with very small size of image elements. Therefore, the statistics in each image element is reduced. A defect of the MLEM algorithm, called "ill-posed problem", arises due to the fewer statistics in each image element. The LM-MLEM algorithm was improved to maximum a posteriori probability estimation (MAPS) to solve the ill-posed problem, as discussed in Chapter 4.3.3. Reconstructed images with the developed algorithm will be shown and discussed in Chapter 4.3.6.

### 4.3.1 Iterative Reconstruction with a Statistical Model

The relationship  $A$  between image  $\mathbf{x}$  and detection probability  $\mathbf{y}$  can be represented by

$$A\mathbf{x} = \mathbf{y}, \quad (4.3)$$

with

$$\mathbf{x} = (x_1, x_2, \dots, x_J)^T, \quad (4.4)$$

where  $x_j(j = 1, \dots, J)$  is the intensity in the  $j^{\text{th}}$  pixel in the image and

$$\mathbf{y} = (y_1, y_2, \dots, y_I)^T, \quad (4.5)$$

where  $y_i(i = 1, \dots, I)$  is the detection probability in the detector pair corresponding event  $i$ .

The element  $a_{ij}$  of the relationship  $A$ , which is called a system matrix, represents the detection probability of the  $\gamma$ -ray emitted from the image element  $j$  by the detector pair corresponding the event  $i$ . The model is based on the detection probability  $\mathbf{y}$  fluctuates around the mean value in Poisson distribution. The following conditional probability:

$$P(\mathbf{y}|\mathbf{x}) = \prod_{i=1}^I P(y_i|\mathbf{x}) \quad (4.6)$$

is corresponding to the likelihood of obtaining the detection probability  $\mathbf{y}$  when the image is  $\mathbf{x}$ . Noise of the image can be minimized by maximizing the likelihood.

Iterative method is a mathematical technique to obtain successive approximation by generating a sequence of improving approximate solutions. The list-mode maximum likelihood expectation maximization (LM-MLEM) algorithm [23] maximizes the probability (4.6). In the algorithm, intensity of  $j^{\text{th}}$  pixels at iteration  $k$ :  $x_j^k$  updates in the following equation:

$$x_j^{k+1} = \frac{x_j^k}{\sum_{i=1}^I a_{ij}} \sum_{i=1}^I a_{ij} \frac{p_i}{\sum_{j'=1}^J a_{ij'} x_{j'}^k}, \quad (4.7)$$

where  $p_i$  represents probability of gamma ray entering the detector. The iterative reconstruction (4.7) basically is consisted of the following steps:

1. Forward projection:

$$y_i = \sum_{j'=1}^J a_{ij'} x_{j'}^k \quad (4.8)$$

2. Comparison:

$$c_i = \frac{p_i}{y_i} \quad (4.9)$$

3. Backward projection:

$$b_j = \sum_{i=1}^I a_{ij} c_i \quad (4.10)$$

4. Update and normalization:

$$x_j^{k+1} = \frac{b_j}{\sum_{i=1}^I a_{ij}} x_j^k . \quad (4.11)$$

In theory, with the perfectly measured background-free data (  $\therefore p_i = 1$  ) and an exact system matrix, the algorithm eventually reach to the point where comparison  $c_i = 1$ . At that point, equation (4.7) becomes

$$x_j^{k+1} = x_j^k , \quad (4.12)$$

hence there is no further change in the iterative reconstruction, which is called full convergence.

### 4.3.2 System Matrix with TOF information

The system matrix  $a_{ij}$  in equation (4.7) is calculated by the integration along the LOR  $i$  over the image element  $j$  weighted by the TOF uncertainty Gaussian function, which has the spatial standard deviation  $\sigma$  and the center  $l_s$ :

$$a_{ij}(l_s) = \int \text{Gaussian}_{\sigma, l_s}(l) dl , \quad (4.13)$$

where  $l$  represents the position of the Gaussian function along the LOR and  $l_s$  represents the shift along the LOR with respect to the center:

$$l_s = \frac{c\Delta t}{2} , \quad (4.14)$$

where  $\Delta t$  is the difference of the time arrival of the photons.

The integration of equation (4.13) is done by Siddon algorithm [24] as shown in figure 4.9. The projection with the TOF information  $p_j$  at the image elements  $j$  is given by the integration for  $[l_j, l_{j+1}]$ :

$$p_j = \frac{1}{2} \left[ \text{erf} \left( \frac{l_{j+1} - l_s}{\sigma\sqrt{2}} \right) - \text{erf} \left( \frac{l_j - l_s}{\sigma\sqrt{2}} \right) \right] , \quad (4.15)$$

where  $\sigma$  is the standard deviation of the TOF uncertainty Gaussian function.

### 4.3.3 Maximum A Posteriori Probability Estimation

A method of obtaining an input from an output is known as an inverse problem. In an inverse problem, a stable solution can not be obtained unless the following three conditions are satisfied as follows:

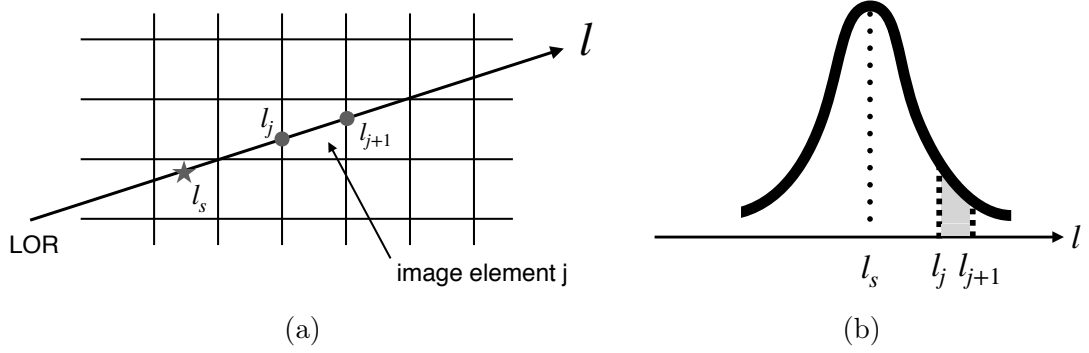


Figure 4.9: Backprojection with TOF information by Siddon algorithm. Schematic example of Siddon algorithm (a) and backprojection with TOF information (b). The points  $l_j, l_{j+1}$  at which the LOR and the image element  $j$  intersect determine the backprojection for the image element  $j$ . The shaded region represents the integration of the Gaussian function for  $[l_j, l_{j+1}]$ , which is given by equation (4.15).

1. the solution exists,
2. the solution is unique,
3. the solution's behavior changes continuously with the initial conditions.

Since the data has the statistical uncertainty and it is contaminated by the backgrounds, the MLEM algorithm often exhibits spurious high-frequency oscillations in the image due to the statistical issue, which is called an ill-posed problem [25]. The issue becomes more significant when the size of the image element is small since statistics in each image element reduces. In order to demonstrate the better granularity of the TT-PET scanner, a dedicated regularization, which reduces the influence by the ill-posed problem, was implemented in the CASToR framework.

A posteriori probability  $P(\mathbf{x}|\mathbf{y})$  is given from a Bayes theorem:

$$P(\mathbf{x}|\mathbf{y}) = \frac{P(\mathbf{y}|\mathbf{x}) P(\mathbf{x})}{P(\mathbf{y})}, \quad (4.16)$$

where  $P(\mathbf{y}|\mathbf{x})$  is the likelihood in equation (4.6),  $P(\mathbf{x})$  is a prior probability of an image  $\mathbf{x}$  and  $P(\mathbf{y})$  is a marginal likelihood. Since the marginal likelihood  $P(\mathbf{y})$  is independent from the image  $\mathbf{x}$ , the posteriori probability  $P(\mathbf{x}|\mathbf{y})$  can be maximized by

$$\arg \max_{\mathbf{x}} P(\mathbf{y}|\mathbf{x}) P(\mathbf{x}), \quad (4.17)$$

hence the prior probability  $P(\mathbf{x})$  has the role to regularize the reconstructed image, corresponding to smoothing the image.

In general, the prior probability  $P(\mathbf{x})$  is described by the following equation:

$$P(\mathbf{x}) = \frac{1}{Z} \exp(-\beta U(\mathbf{x})), \quad (4.18)$$

where  $U(\mathbf{x})$ , called energy function, is the model regarding to the smoothness of the reconstructed image,  $\beta$  expresses the strength of the regularization and  $Z$  is the normalization factor. In this study, the simplest and widely used model, which is based on the Gibbs distribution from the Markov Random Fields, was chosen for the energy function  $U(\mathbf{x})$ . The energy function of the Gibbs distribution is given by

$$U(\mathbf{x}) = \sum_{i,j} \omega_{ij} V(x_i - x_j), \quad (4.19)$$

where  $\omega_{ij}$  is described by

$$\omega_{ij} = \begin{cases} 1 & \text{(image elements } i \text{ and } j \text{ are in contact)} \\ 0 & \text{(others)} \end{cases}, \quad (4.20)$$

and  $V(r)$ , called a clique potential, is given by

$$V(r) = r^2. \quad (4.21)$$

The MLEM algorithm (4.7) can be simply adopted to maximize the posteriori probability by the one-step-late (OSL) method [26]:

$$x_j^{k+1} = \frac{x_j^k}{\sum_{i=1}^I a_{ij} + \beta \left. \frac{\partial U(\mathbf{x})}{\partial x_j} \right|_{\mathbf{x}=\mathbf{x}^{(k)}}} \sum_{i=1}^I a_{ij} \frac{p_i}{\sum_{j'=1}^J a_{ij'} x_{j'}^k}. \quad (4.22)$$

The penalty term  $\beta \left. \frac{\partial U(\mathbf{x})}{\partial x_j} \right|_{\mathbf{x}=\mathbf{x}^{(k)}}$  was added into the normalization step of the MLEM algorithm in the CASToR framework. This algorithm is called maximize a posteriori probability (MAPS) algorithm [26–28].

#### 4.3.4 Normalization

The normalization step in the iteration method (4.11) is done to correct the geometry acceptance of the detector, while the efficiency of the detector is not included in

the normalization step. The normalization factors based on the detector efficiency was calculated by the following techniques.

The image of a rod  $^{18}\text{F}$  source with a diameter of 36 mm and a length of 40 mm was reconstructed by MLEM algorithm and the normalization factor  $n_i$  is defined as the intensity of the  $i$ -th image element obtained. Figure 4.10 shows the normalization factor map.

### 4.3.5 Spatial Resolution

The point source with 0.6 mm diameter in the position 0, 5, 10, 15 mm at the center of the axial FOV and 0, 5, 10, 15 mm at  $z=12.5$  mm were used for the spatial resolution study. The width of the point spread function reconstructed by the iterative reconstruction is defined in the axial, tangential and radial component by its full width at half-maximum amplitude (FWHM) and full width at tenth-maximum amplitude (FWTM). The results are summarized in Table 4.1 and Table 4.2.

Table 4.1: Spatial resolution for four different radial positions at the center of the axial FOV.

Source radial position [mm]	0	5	10	15
FWHM radial [mm]	0.59	0.57	0.56	0.52
FWHM tangential [mm]	0.60	0.60	0.67	0.71
FWHM axial [mm]	0.50	0.49	0.50	0.51
FWTM radial [mm]	1.8	1.6	1.5	1.4
FWTM tangential [mm]	1.8	1.7	1.9	2.0
FWTM axial [mm]	1.1	1.1	1.1	1.1

### 4.3.6 Derenzo Phantom

An iterative image reconstruction with TOF information was performed for a Derenzo phantom with 6 different diameter of rods (0.5, 0.7, 1, 1.2, 1.5, 2 mm), as shown in figure 4.11. The distance between the rods with the same diameter is two times longer than the diameter. The axial length of the Derenzo phantom was shorten to 4 mm in the simulation in order to reduce the computing time. The total intensity of the phantom was set to be equivalent to approximately 50 MBq. The reconstructed image after 5, 10, 100 iterations, which is shown in figure 4.12, shows that the MAPS algorithm solves the problem of the ill-posed problem and



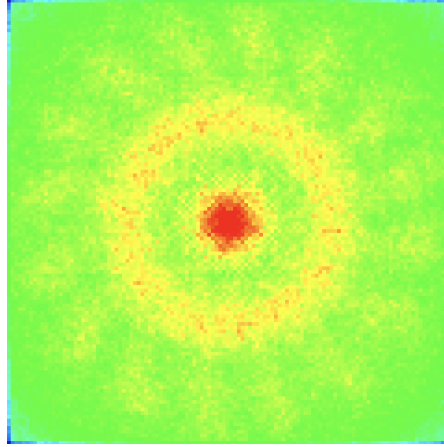


Figure 4.10: Normalization factor map.

Table 4.2: Spatial resolution for four different radial positions at  $z=12.5$  mm of the axial FOV.

Source radial position [mm]	0	5	10	15
FWHM radial [mm]	0.65	0.61	0.60	0.56
FWHM tangential [mm]	0.64	0.65	0.65	0.7
FWHM axial [mm]	0.45	0.45	0.45	0.45
FWTM radial [mm]	2.0	1.8	1.7	1.6
FWTM tangential [mm]	2.0	1.9	1.9	2.0
FWTM axial [mm]	0.94	0.96	1.0	1.0

the TT-PET scanner can resolve the structure of 0.7 mm diameter rods. Figure 4.13 shows the comparison of the reconstructed image with and without TOF information. The reconstructed image with TOF information has better contrast and SNR than without TOF information.

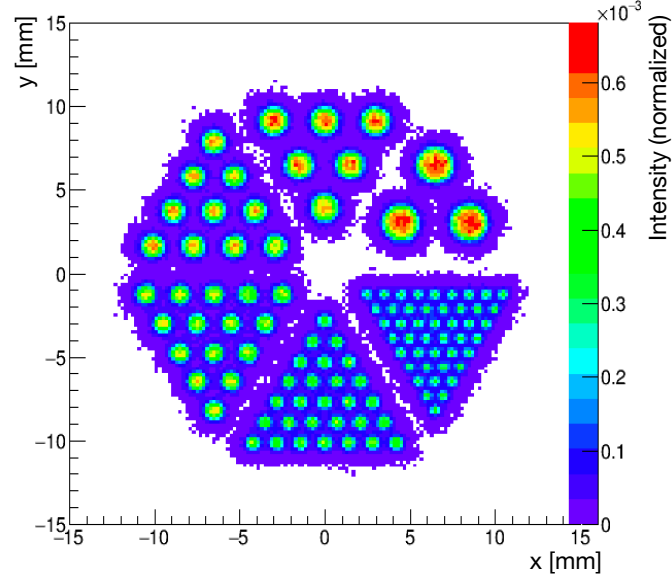


Figure 4.11: Truth position distribution of annihilations for Derenzo Phantom (normalized).

## 4.4 Discussion

Table 4.3 summarises the comparison of the expected performance of the TT-PET scanner and the performance of the existing small animal PET-MRI scanners, Hyperion IID[29], MADPET4 [30], University of Manitoba [31], Seoul [32]. The TT-PET scanner is expected to have the best spatial resolution and coincidence time resolution. This is because the conventional PET scanners are based on inorganic crystals and Si-PMs and the spatial resolution and the time resolution are limited by the scintillation crystals, as discussed in Chapter 3.1, while the photon detection of the TT-PET scanner has better granularity and time resolution. The competitive NECR is expected since the TT-PET scanner has higher sensitivity and better random coincidence background rejection thanks to the smaller coincidence time window, which is allowed by the better time resolution. As shown in figure 4.14, the NECR of the conventional scanners decrease above 50 MBq due to the high random coincidence rate and the high data transfer rate, while the NECR of the TT-PET scanner is expected to increase up to the 300 MBq thanks to the time resolution and the readout system, as shown in figure 4.7 and figure 4.8.

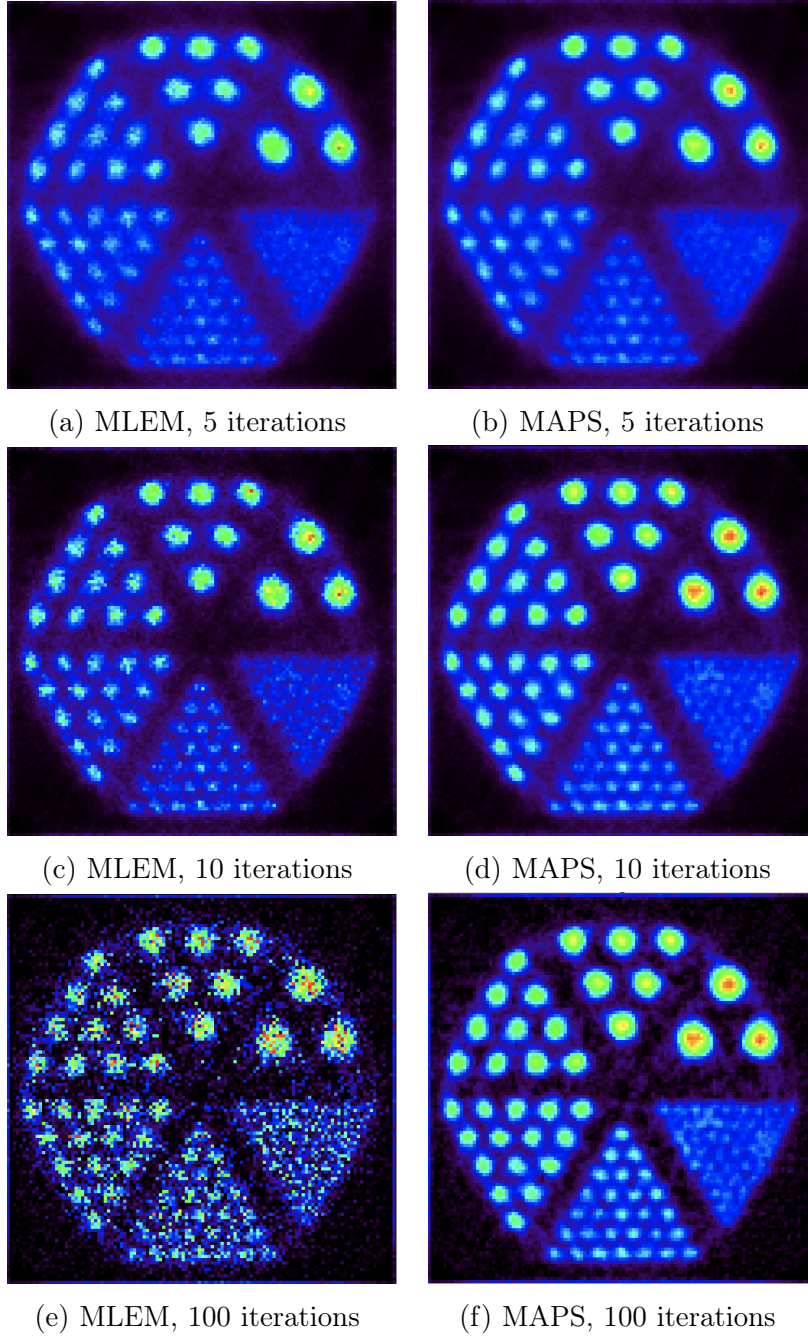


Figure 4.12: TOF Reconstruction with MLEM algorithm and MAPS algorithm of Derenzo phantom at the center along the axial FOV. The diameter of the rods are 0.5, 0.7, 1.0, 1.2, 1.5, 2 mm. High frequency noise can be seen in the image reconstructed in MLEM algorithm with 100 iterations (e). On the other hand, it cannot be seen in MAPS algorithm with 100 iterations thanks to the regularization (f).

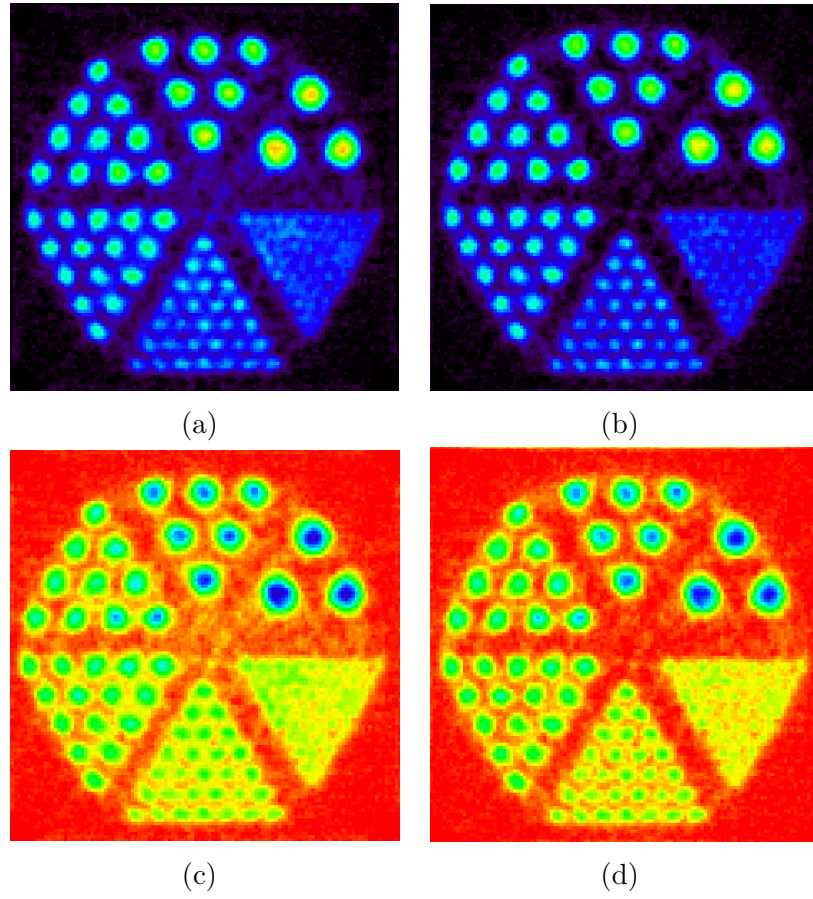


Figure 4.13: Reconstructed images without TOF information (a) (inverse scale: (c)) and with TOF information (b) (inverse scale: (d)). Scale is adjusted to compare the images.

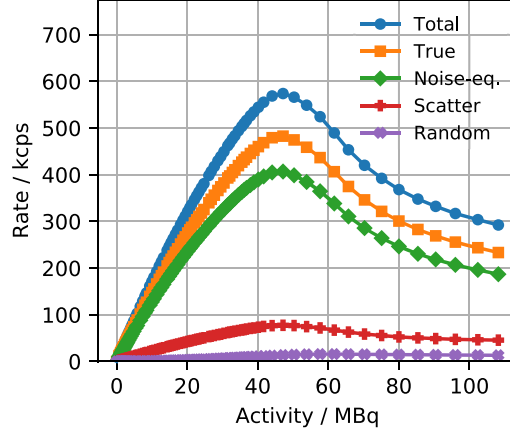


Figure 4.14: NECR of Hyperion IID. NECR at 50 MBq is approximately 400 kcps. (source: [29]).

Table 4.3: Comparison with the conventional small animal PET-MRI scanners. Spatial resolution is defined as the FWHM of the point spread function in the reconstructed image. NECR is calculated with two different phantoms, one is mouse-like phantom made of water and another one is made of acrylic. NECR is the maximum value with the source of 20 ~ 50 MBq. Sensitivity is the value at the central position along axial FOV: [29–32]

	TT-PET	Hyperion	MADPET4	Manitoba	Seoul
Spatial resolution [mm]	0.5 ~ 0.7	1.7	1 ~ 3	1 ~ 1.5	0.7 ~ 1.5
Coinc. time resolution [ps]	80	605	308	-	960
NECR (mouse-like) [kcps]	-	-	40	20	40
NECR (acrylic) [kcps]	800	400	-	-	-
Sensitivity [%]	4	4	0.72	2.2	3.5



## Part II

# Development of Annihilation Photon Detection with Fast Timing Monolithic Silicon Pixel Sensors





# Chapter 5

## Fundamental Semiconductor Sensor Properties

In this chapter, fundamental silicon sensor properties will be discussed for the design and the development of the fast timing monolithic silicon pixel sensor. Physics of charged particle interaction with matter will be introduced in Chapter 5.1. Semiconductor physics and devices in particular related to improvement of time resolution will be discussed in Chapter 5.2. In Chapter 5.3, time resolution of silicon pixel detector will resolve into several components and those will be discussed in detail. Semiconductor technologies used in this research will be introduced in Chapter 5.4. Furthermore, the target of the sensor design and the simulation framework of the design will be discussed in Chapter 5.5.

### 5.1 Charged Particle Interactions in Matter

#### 5.1.1 Bethe-Bloch Formula

Charged particles deposit their energy by collision with atomic electrons. Energy deposit in particles heavier than electrons can be expressed by Bethe-Bloch equation:

$$-\frac{dE}{dx} = Kz^2 \frac{Z}{A} \frac{1}{\beta^2} \left[ \frac{1}{2} \ln \frac{2m_e c^2 \beta^2 \gamma^2 T_{max}}{I^2} - \beta^2 - \frac{\delta}{2} \right], \quad (5.1)$$

where

$\frac{dE}{dx}$     energy loss of the particle

$K$     0.307 075 MeVcm<sup>2</sup>

- $z$  charge of the traversing particle in units of the electron charge
- $Z$  atomic number of absorption medium (14 for silicon)
- $A$  atomic mass of absorption medium (28 for silicon)
- $m_e c^2$  511 MeV
- $\beta$  velocity of the transversing particle in units of the speed of light
- $\gamma$  Lorentz factor
- $I$  mean excitation energy (137 eV for silicon).

In silicon, the deposited energy generates electron-hole pairs. Considering the same situation as the TT-PET scanner, a 511 keV electron generates approximately 20000 electron hole pairs for 100  $\mu\text{m}$  thickness silicon sensor, while a minimum ionizing particle (MIP) generates approximately 7000 electron hole pairs.

### 5.1.2 $\delta$ Electron

The electron-hole pairs generated along transversing particles are not distributed uniformly in a sensor. Figure 5.1 shows a physics process, called a  $\delta$  electron. The knock-on electron is emitted perpendicular to the path of the primary charged particle, and deposits non-negligible energy for a thin sensor. The effect adds a long tail for the energy loss distribution (Landau fluctuation), and degrades the performance of the spatial resolution of the sensor due to the perpendicular path of the  $\delta$  electron to the primary particles.

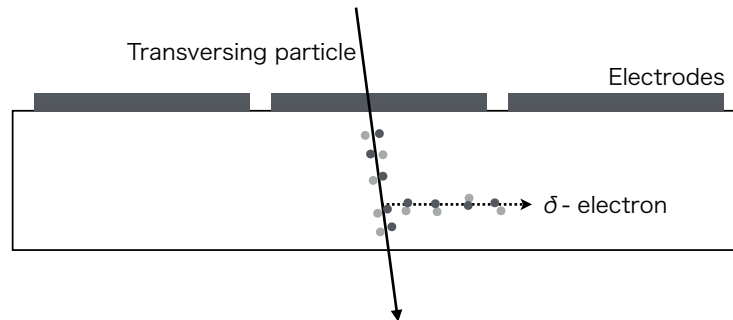


Figure 5.1: A  $\delta$  electron from transversing particle on a sensor. The additional energy deposits affects the uniformity of electron-hole pairs distribution.

## 5.2 Semiconductor Physics and Devices

### 5.2.1 Intrinsic Charge Carrier Concentration

Since silicon has a suitable band gap as a semiconductor (1.12 eV) and can be mass-produced, it is widely used as a semiconductor material. From Fermi-Dirac statistics, the charge carrier concentration in intrinsic silicon, which means that the impurity of the material is negligible, is given by

$$n_i^2 = N_C N_V \exp\left(\frac{-E_g}{kT}\right), \quad (5.2)$$

where  $N_C(N_V)$  is effective density of states in the conduction (valence) band,  $E_g$  is a band gap between the lowest energy of the conduction band and the highest energy of the valence band,  $k$  is Boltzmann constant and  $T$  is temperature. The intrinsic charge carrier concentration  $n_i$  of silicon at 300 K:

$$n_i = 1.45 \times 10^{10} \text{ cm}^{-3} \quad (5.3)$$

is too large compared to a signal produced by particle interaction in silicon, hence the charge carrier density is removed by pn-junction with reverse biased voltage, which will be discussed in section 5.2.2.

### 5.2.2 The pn-Junction

An electron-rich n-type (donor) semiconductor is processed by doping silicon crystal comprising tetravalent silicon with pentavalent element, e.g. phosphorus. A hole-rich p-type (acceptor) semiconductor is processed by doping silicon crystal with trivalent element, e.g. boron. As shown in figure 5.2, when an n-type semiconductor and a p-type semiconductor are bonded to each other, electrons and holes of respective semiconductors are connected in the vicinity of the junction. Ions of the n-type semiconductor and of the p-type semiconductor form an electric field. This diffusion process reaches equilibrium when the Fermi level of each semiconductor becomes the same. The region where electrons and holes are reduced due to diffusion is called depletion layer. When a positive voltage is applied to the n-type semiconductor or a negative voltage is applied to the p-type semiconductor, the distance between the electrons and the holes is increased and the depletion layer is widened. This voltage is called a reversed bias voltage.

The depletion depth  $W$  can be obtained by

$$W = x_n + x_p \quad (5.4)$$

$$= \sqrt{\frac{2\epsilon_0\epsilon_{\text{Si}}}{e} \left( \frac{1}{N_A} + \frac{1}{N_D} \right) (V + V_{\text{bi}})} , \quad (5.5)$$

where  $x_n$  and  $x_p$  are the depletion depth on n-side and p-side respectively,  $e$  is the elementary charge,  $\epsilon_0$  and  $\epsilon_{\text{Si}}$  are permittivity in vacuum and relative permittivity in silicon respectively,  $N_A$  and  $N_D$  are doping concentration of acceptors and donors respectively, and  $V$  and  $V_{\text{bi}}$  are applied external voltage and built-in voltage respectively. When the junction is generated by highly doped  $n^+$  implant in a low-doped bulk ( $N_A \ll N_D$ ) and the external voltage is applied much larger than the built-in voltage ( $V_{\text{bi}} \ll V$ ), the depletion depth  $W$  can be approximated as follows:

$$W \simeq x_p \simeq \sqrt{\frac{2\epsilon_0\epsilon_{\text{Si}}}{eN_A} V} . \quad (5.6)$$

The resistivity  $\rho$  of doped silicon is given by

$$\rho = \frac{1}{e\mu N} , \quad (5.7)$$

where  $\mu$  is the majority carrier mobility and  $N$  is the dopant density. Thus, the depletion length  $W$  in (5.6) is represented by

$$W \simeq \sqrt{2\epsilon_0\epsilon_{\text{Si}} V \mu \rho} . \quad (5.8)$$

For a sensor design with wide pixels, the bulk capacitance of the pixel sensor is determined by the pixel area  $A$  and the depletion length  $W$

$$C \simeq \epsilon_0\epsilon_{\text{Si}} \frac{A}{W} , \quad (5.9)$$

hence the capacitance  $C$  depends on the resistivity  $\rho$  and the reversed bias voltage  $V$  in (5.8).

### 5.2.3 Charge Carrier Transportation

#### Drift

When ionizing charged particles pass through the depletion region, electron-hole pairs are generated. Electrons and holes are separated and accelerated by the

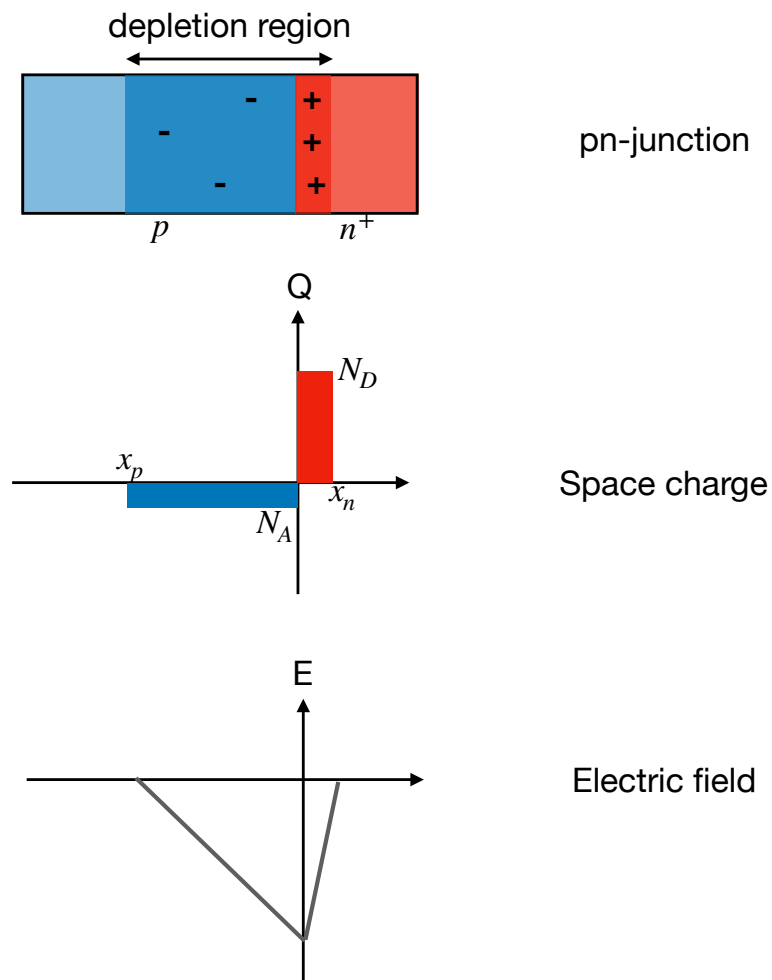


Figure 5.2: Charge carrier density, space charge and electric field at a pn-junction. The depletion region is widened to a low-doped implant when a reversed bias voltage is applied.

electric field  $\vec{E}$ , and collected in the electrodes of the sensor. The average drift velocity of the charge carriers are given by

$$\vec{v}_n = -\mu_n \vec{E} \quad \text{for electrons,} \quad (5.10)$$

$$\vec{v}_p = \mu_p \vec{E} \quad \text{for holes,} \quad (5.11)$$

where  $\mu_n(\mu_p)$  is the mobility of the electrons (holes).

The mobility at the low electric field in the intrinsic silicon given as

$$\mu_n = 1415 \text{ cm}^2/(\text{Vs}) \quad (5.12)$$

$$\mu_p = 480 \text{ cm}^2/(\text{Vs}) \quad (5.13)$$

At the higher electric field  $\vec{E}$ , the higher random collision rate of the carriers leads to a smaller mean free path of the carriers. The drift velocity finally saturates due to its effect. Figure 5.3 shows the drift velocity as a function of the external electric field. The drift velocity saturates at electric field larger than  $3 \times 10^4 \text{ V/cm}$ .

## Diffusion

Another charge carrier transport mechanism is the random movements of the carriers from high concentration region to low concentration region. The diffusion current of the charge carriers is given by

$$\vec{J}_n = -D_n \vec{\nabla}_n \quad \text{for electrons,} \quad (5.14)$$

$$\vec{J}_p = D_p \vec{\nabla}_p \quad \text{for holes,} \quad (5.15)$$

where  $D_n$  and  $D_p$  are diffusion constants of electron and hole,  $\vec{\nabla}_n$  and  $\vec{\nabla}_p$  are the gradients of the electron and hole concentration.

### 5.2.4 Avalanche Breakdown

When the speed of the charge carriers is high enough to knock out the bound electrons in the silicon, more free charge carriers are generated and the generated carriers creates further knock out processes. The iterative process, which is called avalanche breakdown, produces the huge current in a sensor. The electric field (voltage) sufficient to cause avalanche breakdown is called breakdown field (voltage). The avalanche mechanism can be used to increase the gain of the sensor, however in this research, it is difficult to optimize the mechanism due to limitations of the semiconductor process, hence a simple n-on-p diode is chosen for a sensor. Rather than using the avalanche mechanism, avoiding dark current due

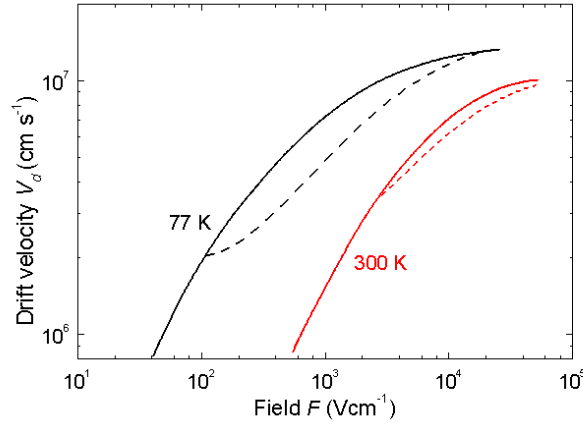


Figure 5.3: Drift velocity as a function of electric field in silicon. Drift velocity saturates at electric field larger than  $3 \times 10^4$  V/cm (source: [33]).

to avalanche breakdown is the key to this research. Figure 5.4 shows breakdown voltage and breakdown field as a function of doping concentration for an abrupt pn-junction. For a p-type  $1000 \Omega \text{ cm}$  resistivity sensor, the breakdown field is approximately  $2 \times 10^5$  V/cm<sup>1</sup>.

### 5.2.5 Guard Ring

Electronics surrounding pixel sensors can be influenced when the depletion region from the pixel sensors reaching the electronics, as shown in figure 5.5. Also, electric field near the surface of the chip is relatively larger than other areas since the electric potential drops suddenly around the sensor. Multiple guard rings are put around the pixels in order to control the depletion region, the electric field and the electric potential. Figure 5.6 shows a guard ring structure, which consists a floating metal and a doping well to suppress electric field and to reduce potential gradually.

## 5.3 Time Resolution of Silicon Pixel Detectors

Figure 5.7 shows the block diagram of a possible front-end electronics of a pixel sensor. The signal from the sensor, which is described as an ideal diode with a

<sup>1</sup>The breakdown field discussed here is for an abrupt pn-junction. If the multiplication region is thick, more realistic avalanche mechanism must be taken into account [34].

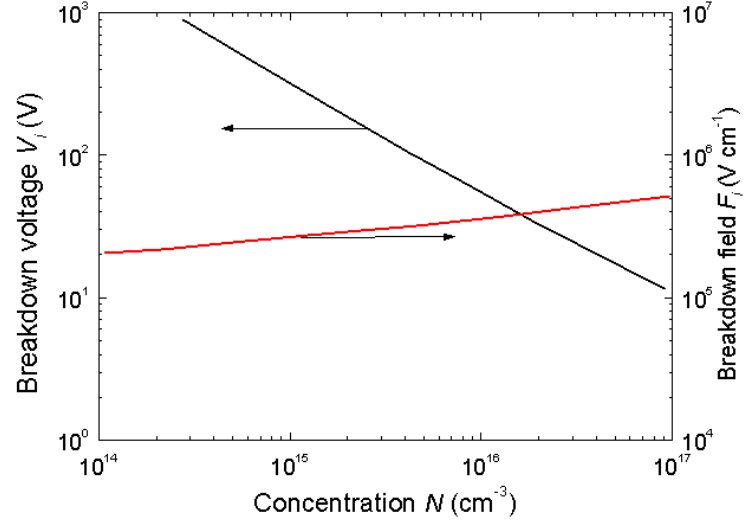


Figure 5.4: Breakdown voltage and field as a function of doping concentration for an abrupt pn-junction (source: [35]).

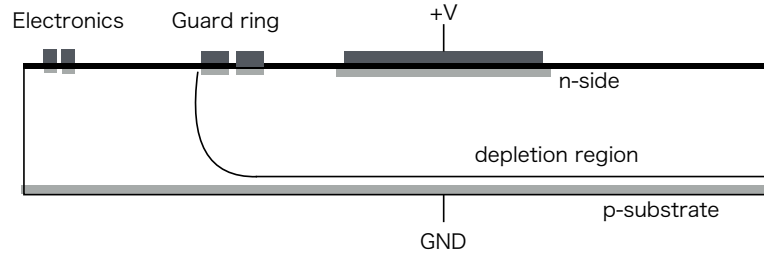


Figure 5.5: Schematic cross section of a sensor edge. The depletion region reaching the electronics may cause a problem regarding to the performance of the electronics. Multiple guard rings are put to control the depletion length, the electric field and the electric potential.



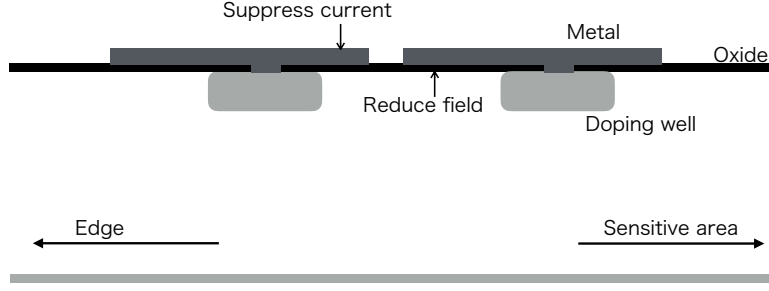


Figure 5.6: Schematic cross section of guard ring. The metals overlap implant doping wells to reduce electric field.

capacitor in parallel, is amplified at the pre-amplifier stage, and then converted into the digital signal at the discriminator. The digital signal contains the time over threshold (ToT) information (see figure 5.8) as well as the timing of arrival (TOA). The TOA information is then digitized with a Time-to-digital converter (TDC).

The total time resolution of the sensor is characterized by 5 different factors:

$$\sigma_{\text{total}}^2 = \sigma_{\text{jitter}}^2 + \sigma_{\text{time walk}}^2 + \sigma_{\text{charge collection}}^2 + \sigma_{\text{distortion}}^2 + \sigma_{\text{TDC}}^2, \quad (5.16)$$

where the time resolutions are due to the following factors,  $\sigma_{\text{jitter}}$ : jitter with electronics noise,  $\sigma_{\text{time walk}}$ : amplitude variation effect (time walk),  $\sigma_{\text{charge collection}}$ : non uniform charge collection,  $\sigma_{\text{distortion}}$  is by the distorted weighting field effect and  $\sigma_{\text{TDC}}$  is by the TDC performance [36]. The detail of each factor is discussed in the following chapters.

### 5.3.1 Jitter

The most important factor in equation (5.16) is the time resolution due to the jitter effect. Figure 5.9 shows a signal pulse including electronics noise and a threshold of a discriminator. The time uncertainty due to the electronics noise is proportional to the voltage noise at the output of the amplifier  $N$  divided by the slope of the signal  $dV/dt$  around the threshold. Suppose that the slope of the signal is constant, the time resolution due to the electronics noise can be expressed as

$$\sigma_{\text{jitter}} = \frac{N}{dV/dt} \quad (5.17)$$

$$\simeq \frac{t_{\text{rise}}}{S/N}, \quad (5.18)$$

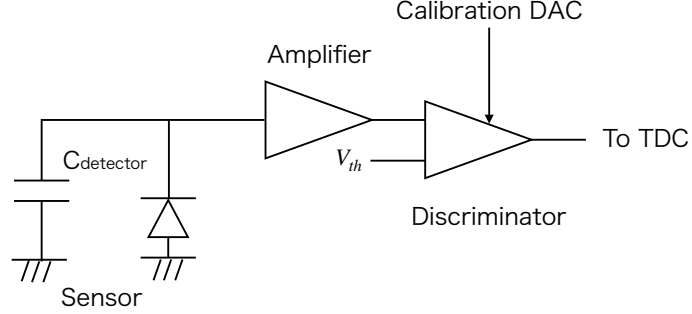


Figure 5.7: Block diagram of front-end electronics. The sensor is shown as an ideal diode with a capacitor in parallel. Its output is amplified and then discriminated. The calibration Digital-to-Analog Converter (DAC) adjusts the threshold  $V_{th}$  on the discriminator. The digital output signal is sent to the TDC.

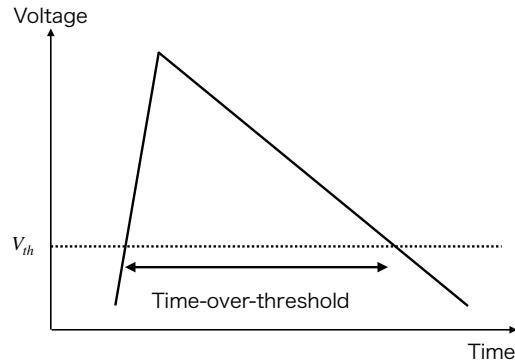


Figure 5.8: Time over threshold (ToT). A duration of a signal pulse above a threshold  $V_{th}$  is defined as time over threshold. Since ToT information is correlated with a signal pulse height, it can be used to estimate the total charge of a signal pulse.

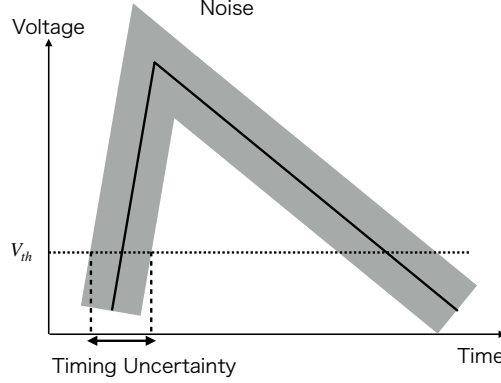


Figure 5.9: Jitter effect on timing resolution. The shaded region represents noise of a signal pulse. Timing uncertainty of ToA due to noise is shown.

where  $S$  is the amplitude of the signal and  $t_{\text{rise}}$  is the rise time of the signal.

The key elements to mitigate the jitter effect are listed as follows:

1. Maximize drift velocity of charge carrier to decrease the rise time  $t_{\text{rise}}$ . Electric field in depletion region is high enough to saturate drift velocity of charge carriers ( $> 3 \times 10^4$  V/cm)
2. Reduce electronics noise  $N$ 
  - (a) Minimize capacitance of sensors
  - (b) Develop low noise front-end electronics
3. Intrinsic signal  $S$  is determined by charged particle interactions. Approximately 3 times better time resolution is expected for 511 keV electron than for MIPs thanks to the larger energy deposits in a thin sensor.

### 5.3.2 Time Walk

Non-uniform energy deposits in a sensor cause time uncertainty due to the different signal amplitude, called time walk effect, as shown in figure 5.10. Although it is most accurate to estimate the signal height or area using ADC for the time walk correction, it is not possible to mount a circuit with these functions on the chip for the TT-PET scanner due to the insufficient space on the chip. For the TT-PET project, the time walk effect is corrected using ToT information since it is not difficult to add a function of measuring signal trailing edge time and the ToT information is correlated with the signal amplitude. However, the resolution of

ToT information is not good as of ADC and sensitive to noise on the signal pulse, hence understanding of the signal noise is essentially important for the time walk correction.

### 5.3.3 Charge Collection Noise

As mentioned in Chapter 5.1.2, the electron-hole pairs generated along the track are not distributed uniformly. Time resolution due to the influence, called charge collection noise, is not ignorable. The effect can be mitigated by reducing the thickness of the sensor. However, the thinning of a sensor increase its bulk capacitance, which results in increase in electronics noise. Monte Carlo simulations show that the effect is approximately 20 ps to MIPs for a 100  $\mu\text{m}$  thick sensor [37].

### 5.3.4 Distortion

A signal is detectable when the charge starts to move since the induced current is generated on the electrodes. The induced current  $i$  by the charge  $q$  is given by the following equation:

$$i = -q\vec{v} \cdot \vec{E}_w, \quad (5.19)$$

where  $\vec{v}$  is the drift velocity of the charge and  $\vec{E}_w$  is the weighting field given by Shockley-Ramo theorem [38, 39]. The uniformity of the drift velocity  $\vec{v}$  can be obtained by high electric field throughout the sensor since the drift velocity of the carrier is saturated. According to the Shockley-Ramo theorem, the weighting field  $\vec{E}_w$  is determined by the geometry of the electrodes. In this study, the weighting field with different geometry was estimated using simulation based on finite element method and the geometry which has negligible effect regarding to the distortion of the weighting field was chosen (see chapter 6.1.2).

### 5.3.5 TDC

The TDC designed for the TT-PET project is a hybrid TDC based on a free-running ring oscillator and a counter synchronous. The timing precision of the TDC is limited by a binning (LSB):

$$\sigma_{\text{TDC}} = \frac{\text{LSB}}{\sqrt{12}}. \quad (5.20)$$

Expected timing uncertainty of a 50 ps binning TDC is approximately 14 ps if the non-linearity effect of the TDC is negligible. A new TDC technique was developed to synchronize 1920 chips at  $\mathcal{O}(10)\text{ps}$  [40].

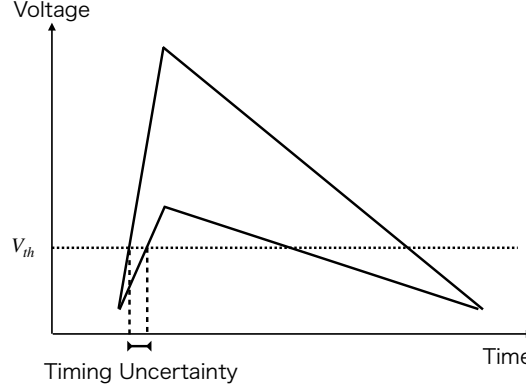


Figure 5.10: Timing uncertainty due to different signal amplitude is shown, called time walk effect.

## 5.4 Semiconductor Technologies

### 5.4.1 Amplifier

A signal pulse from a silicon pixel sensor is not strong enough to be noise-tolerant and not strong enough for a discriminator. Fast and low noise amplifier for a short integration time is the key to reduce timing resolution due to the jitter effect ( $\sigma_{\text{jitter}}$ ).

#### Bipolar Junction Transistor

Figure 5.11 represents a common-emitter npn-Bipolar Junction Transistor (BJT). The three regions of a BJT are called emitter, base and collector. The base-emitter junction and the collector-emitter junction are forward biased ( $V_{BE}$ ,  $V_{CE}$ ). Most of electrons flowing from emitter to base do not recombine with holes in base but reach the collector as the base is very thin. The rate of emitter current  $I_E$  reaching collector is called base transfer factor  $\alpha$ . A BJT is characterized by a current gain  $\beta$ , which is the fraction of collector current  $I_C$  and base current  $I_B$ :

$$\beta = \frac{I_C}{I_B} = \frac{\alpha I_E}{(1 - \alpha) I_E} = \frac{\alpha}{1 - \alpha} . \quad (5.21)$$

The current gain  $\beta$  decreases above a certain frequency and the frequency at which  $\beta = 1$  is called transition frequency  $f_T$ . The transition frequency  $f_T$  depends on the collector current  $I_C$  of the BJT. Power consumption of a BJT is given by  $P \sim V_{CE} \cdot I_C$ . The BJT technology for the TT-PET project must provide

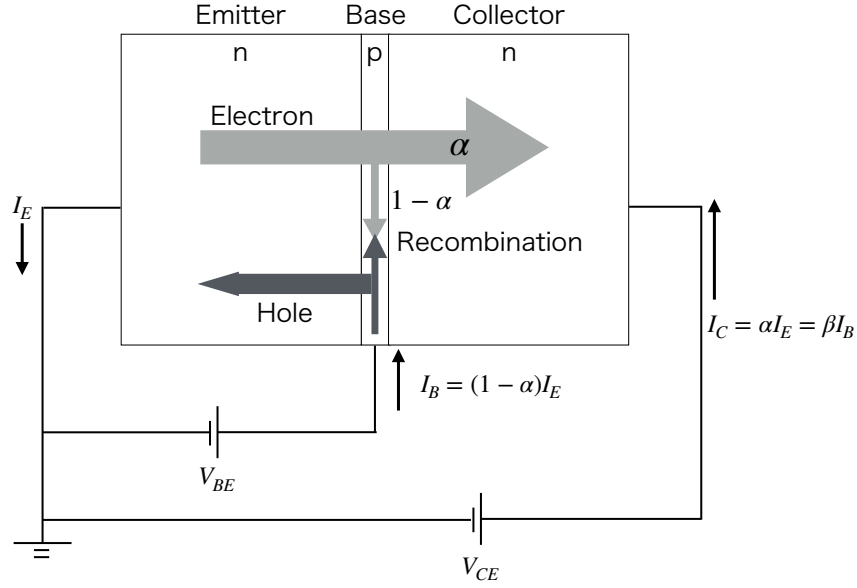


Figure 5.11: A common-emitter NPN bipolar transistor. Electrons in emitter reaches collector with probability  $\alpha$  and recombine holes at base with probability  $1 - \alpha$ .

$f_T > 100$  GHz for a fast amplification from silicon pixel sensor signal with low power consumption.

BJT technology is superior to field-effect transistor (FET) in both speed and noise for a short integration time ( $\tau < 10$  ns) [41], hence BJT is chosen for an amplifier.

### SiGe Hetero-junction Bipolar Transistor

The current gain  $\beta$  is improved by increasing the base transfer factor  $\alpha$ . Germanium has lower band gap (0.66 eV at 300 K) than silicon. In Silicon-Germanium Hetero-junction Bipolar Transistor (SiGe-HBT), the amount of germanium is graded in the base region, thus making the band gap narrower at the collector than at the emitter, hence the electrons injected from the emitter drift thanks to the electric field in the base (see figure 5.12). Therefore, changing the charge transport mechanism from diffusion to drift in base, the base transfer factor  $\alpha$  is successfully increased.

SiGe-HBT technology (SG13S [42] from IHP microelectronics, with common-emitter current gain  $\beta = 900$  and transition frequency  $f_T = 300$  GHz) was chosen to achieve a short integration time ( $\lesssim 1$  ns), low equivalent noise charge ( $< 600$

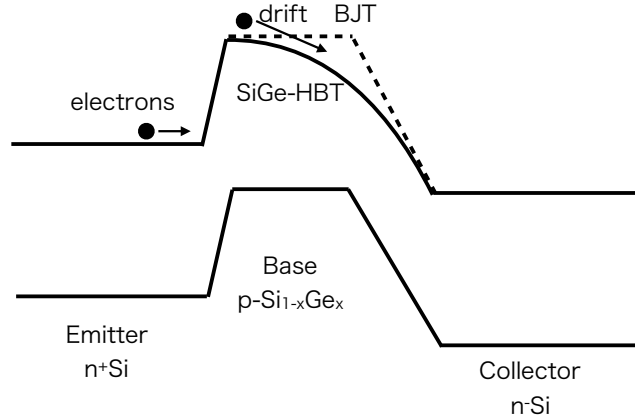


Figure 5.12: Band gap of SiGe Hetero junction bipolar transistor. The amount of Germanium  $x$  graded in the base region generates electric field in its region.

electrons on 0.8 pF capacitance) and low power consumption ( $135 \mu\text{W}/\text{mm}^2$ ) [43]. Figure 5.13 shows that the working point of the SiGe-HBT for the TT-PET scanner. For the fast amplification of the signals from the silicon pixel sensors and the budget of the power consumption, the working point is set to the different point from the technology nominal value. The performance of the SiGe-HBT depends on the collector current  $I_C$ , which determines the power consumption.

### 5.4.2 Monolithic Process

An integration of a readout chip and a pixel sensor can be done by connecting the two parts each of them, produced in dedicated semiconductor processes, by a high-density interconnection technique, most commonly bump-bonding [44]. However, the bump-bonding technique adds insensitive material and it is expensive to produce in a large area. For the TT-PET scanner, the silicon pixel sensor and the read out electronics are fabricated in the same process to be thin ( $100 \mu\text{m}$ ) and inexpensive for a large area production. However, the monolithic process was originally developed for the silicon devices in electronics, hence the process is not optimized to operate with high voltage. The behavior of the pixel sensor under high voltage must be precisely estimated before the production.

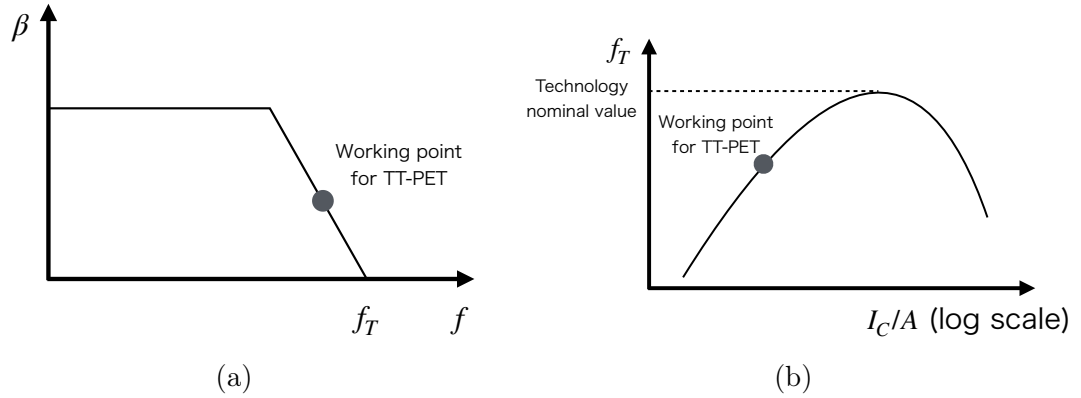


Figure 5.13: Working point of the SiGe-HBT for the TT-PET scanner. Current gain  $\beta$  as a function of frequency  $f$  (a) and transition frequency  $f_T$  as a function of collector current  $I_C$  normalized by area  $A$  (b). The working point for the TT-PET scanner is different from the technology nominal value.

## 5.5 Sensor Design

A simulation work was performed to design the fast timing monolithic silicon pixel sensor produced in the SG13S process by IHP microelectronics and to characterize the sensor performance. The targets of the sensor simulation for the TT-PET project are following:

1. High voltage must be applied to saturate drift velocity and to achieve full depletion. In particular, the guard ring surrounding the pixel sensors is the key to achieve high operation voltage within the monolithic process. The dedicated guard ring structure was designed using the sensor simulation.
2. The total capacitance of the pixel sensor including the parasitic capacitance must be less than 1 pF to fulfill the requirement for low noise from the front-end electronics. The distortion effect due to the weighting field can be mitigated by reducing the ratio between the pixel size  $S$  and the thickness  $d$  (i.e.  $S/d$ ), hence there is a trade-off between the weighting field and the capacitance regarding to the ratio. The weighting field and the capacitance of the pixel sensor was estimated using the simulation to optimize the sensor geometry.



### 5.5.1 TCAD Simulation

A Technology Computer Aided Design (TCAD) simulation framework is used to design silicon devices as well as to evaluate its performances. In this study, Synopsys Sentaurus TCAD (version I) is used [45]. TCAD is basically divided into a process simulator and a device simulator. A process simulator emulates semiconductor manufacturing process flows of semiconductor devices. However, the computation time is very long ( $> 10$  hours for each design of a device), hence it is not realistic to use a process simulation for an optimization of silicon sensor properties. Another way to reproduce a silicon device in TCAD is to design the structure of the device manually using a structure editor. A structure editor has advantages of parametrizing the structure of the device and of short computing time ( $< 10$  s). In this study, the doping profiles of the SG13S process were provided by IHP microelectronics and the structure of the sensor was simulated using a structure editor. A structure editor discretizes the device into a finite number of domains, called meshing, for a device simulation. Using a finite element method (FEM), approximate solutions of boundary value problems were obtained in a device simulator.

### 5.5.2 Physics Models and AC analysis

Physics models used in the device simulation will be introduced in the next paragraphs.

For a calculation of an electrostatic potential, Poisson equation was used:

$$\nabla \varepsilon \cdot \nabla \phi = -q(p - n + N_D - N_A) , \quad (5.22)$$

where  $\varepsilon$  is the electrical permittivity,  $\phi$  is the electrostatic potential,  $q$  is the charge,  $n$  and  $p$  is the electron and hole density, respectively and  $N_D$  and  $N_A$  is the donor and acceptor concentrations, respectively.

A carrier transport model for a semiconductor can be written in continuity equations:

$$\nabla \cdot \vec{J}_n = qR_{\text{net}} + q\frac{\partial n}{\partial t} \quad (5.23)$$

$$-\nabla \cdot \vec{J}_p = qR_{\text{net}} + q\frac{\partial p}{\partial t}, \quad (5.24)$$

where  $\vec{J}_n$  and  $\vec{J}_p$  are the electron and hole current density, respectively,  $R_{\text{net}}$  is the net recombination rate. In addition, a Hydrodynamic model [46] was used of current-voltage simulations and standard drift-diffusion model was used for the other simulations.

The generation and recombination rate is based on the Shockley–Read–Hall (SRH) recombination [47, 48]. The SRH model in Sentaurus TCAD can be customized to add doping and temperature dependencies. Since band-gap narrows and mobility decreases in the high doping region, a Slotboom model [49] and a doping-dependent mobility model [50, 51] were used.

Electronic circuit simulation (SPICE) integrated in Sentaurus TCAD was performed for a small signal AC analysis for a capacitance-voltage simulation.

# Chapter 6

## Analog Prototype Developments

The analog prototype chip was designed based on the sensor simulations and its performance was characterized by measurements with radioisotopes, a laser and hadron beams at CERN SPS. The target of the analog prototype is to characterize the performance of the sensor and the front-end electronics and to identify issues towards the production of the demonstrator, which has all features of the TT-PET sensor.

The design work using TCAD simulation and the layout of the analog prototype chip will be discussed in Chapter 6.1 and lab measurements and a test beam measurement will be discussed in Chapter 6.2

### 6.1 Design

As discussed in Chapter 5.5, a TCAD simulation work plays an important role for the sensor performance optimization. The TCAD simulation works will be discussed and the layout of the analog prototype based on the result of the TCAD simulation work will be shown.

#### 6.1.1 TCAD Simulation for Guard Ring Design

A dedicated guard rings structure was designed using TCAD simulations to be able to apply the high voltage of 200 V without incurring in breakdown in the silicon. The guard ring consists of six n-type implantations (n-Wells) alternating with seven shallow p-type implantations (p-Stop) to reduce the potential in the sensor gradually from the pixels to the outermost guard ring (see Figure 6.1). The n-Wells are covered by metal electrodes to reduce electric potential gradually and to suppress the current flow. The five outermost n-Wells are electrically floating.

Figure 6.2 shows the layout of the guard ring and simulation results for a potential at 200 V. The electric field in the sensor is expected not to reach a critical value ( $\sim 2 \times 10^5$  V/cm with 1 k $\Omega$  cm bulk resistivity from figure 5.4) for a potential up to 200 V applied to the pixel.

### 6.1.2 TCAD Simulation of Weighting Potential

As shown in figure 6.3, weighting potentials with different pixel sizes were simulated using TCAD simulation based on the Shockley-Ramo's theorem. The sensor thickness was fixed at 100  $\mu$ m and the pitch of the electrodes are 10% longer than the pixel size. According to the Shockley-Ramo's theorem, 1 V was applied to the pixel and 0 V to the neighboring pixels and the backside and the material of the space between the electrodes was set to vacuum in the simulation. The simulation confirms that uniform weighting field is expected when the pixel size is 2 times larger than the sensor thickness.

### 6.1.3 TCAD Simulation of Pixel Capacitance

The pixel capacitance is a critical parameter that affects the amplifier performance and ultimately the sensor time resolution. To facilitate the design it was estimated using TCAD simulation. Figure 6.4 shows the expected bulk capacitance and inter-pixel capacitance of neighboring pixels as a function of high voltage with the different pixel sizes and pitches. Less than 1 pF bulk capacitance is expected and the inter-pixel capacitance was found to be negligible compared to the bulk capacitance. The full depletion is expected at 100 V for a 100  $\mu$ m thickness sensor with 1000  $\Omega$ cm resistivity.

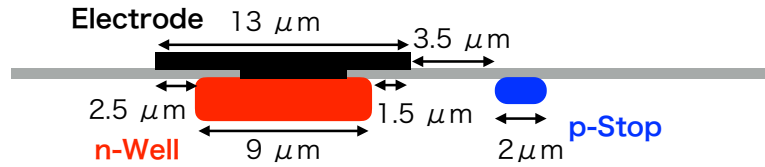
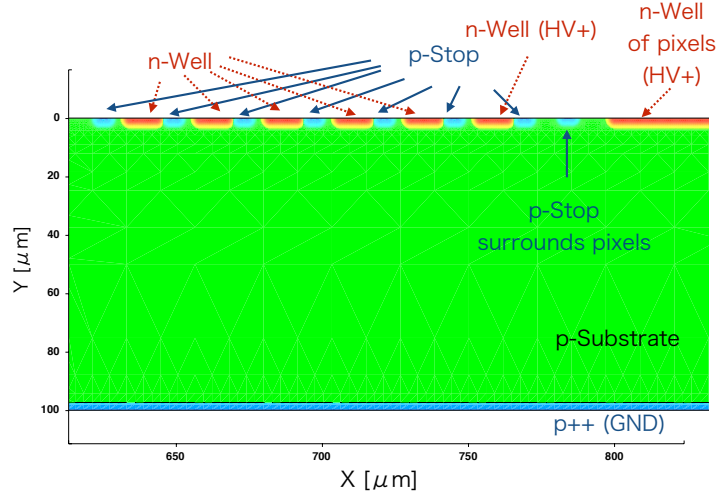
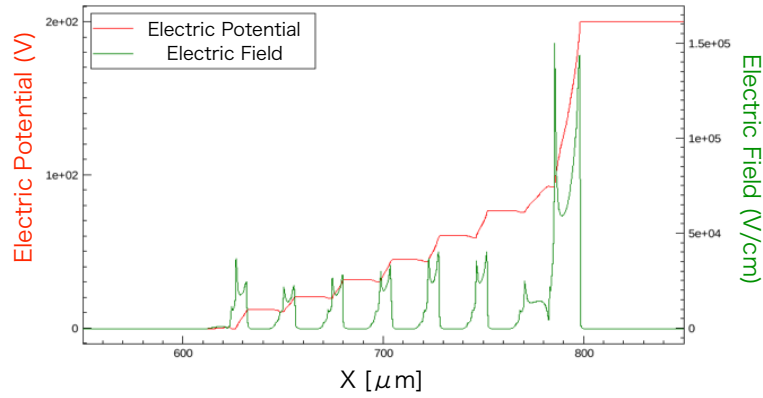


Figure 6.1: Schematic geometry of a guard ring. The geometry of a guard ring was optimized using TCAD simulation to reduce electric potential and to minimize electric field around n-Well and p-Stop.



(a)



(b)

Figure 6.2: Multiple guard rings for the 1st ASIC demonstrator. Cross section of a doping profile guard ring structure (a) and electric potential and field distributions at  $Y \sim 1 \mu\text{m}$ , where the highest electric field is observed (b). Color scale is not shown due to confidentiality. Positive high voltage can be applied on the pixel n-Well and on the innermost guard ring. For this simulation, all the guard rings are left floating and 200 V was applied on the pixel n-well.

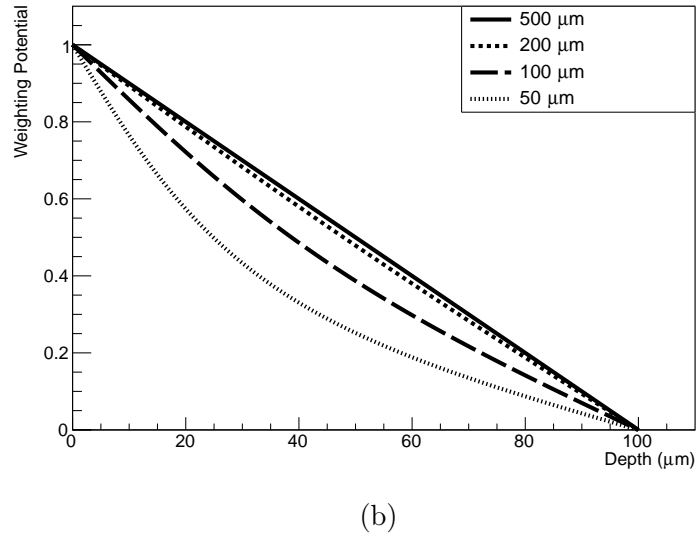
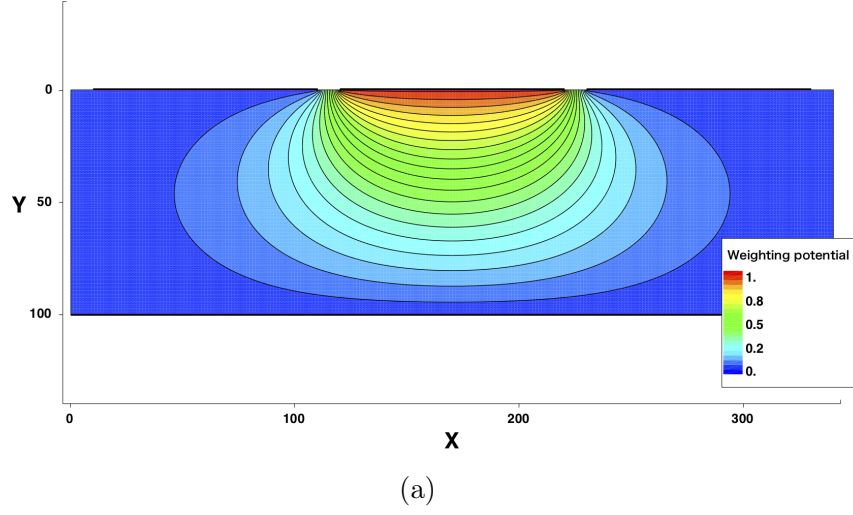


Figure 6.3: Simulation of weighting potential of a 50  $\mu\text{m}$  pixel sensor (a) and the weighting potential at the middle of the central pixel (b). The weighting potential is distorted in smaller pixels.

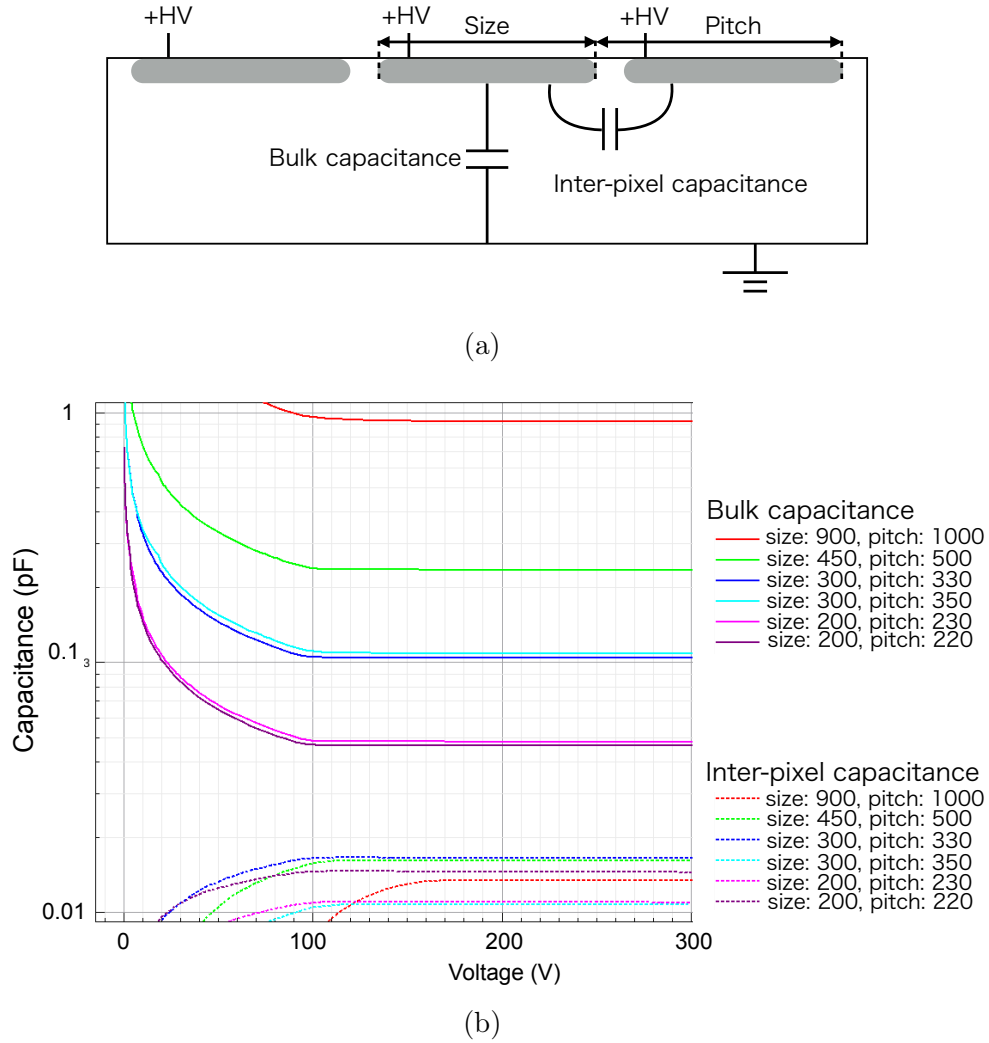


Figure 6.4: Schematic cross section of a C-V simulation setup (a) and simulation of bulk and inter-pixel capacitance as a function of voltage (b).

### 6.1.4 Layout of Analog Prototype Chip

The electric field is expected not to reach the breakdown for a potential up to 200 V thanks to the six guard rings structure designed for the analogy prototype. According to the TCAD simulation, highest electric field is expected between n-Well of pixels and p-Stops surrounding the pixels. This electric field cannot be controlled by optimizing the geometry of the guard ring design. To reduce the electric field, the possibility to apply high voltage to the n-Well of the innermost guard ring was implemented.

Less than 1 pF pixel capacitance is expected when the pixel area is smaller than  $900\text{ }\mu\text{m} \times 900\text{ }\mu\text{m}$  for 100  $\mu\text{m}$  thickness at full depletion voltage. Inter-pixel capacitance is expected to be negligible when the inter-pixel spacing is approximately 10% of the pixel size.

Figure 6.5 shows the layout of the analog prototype chip, which is designed based on the TCAD simulation works. It consists of a large pixel ( $900\text{ }\mu\text{m} \times 900\text{ }\mu\text{m}$ ) and a small pixel ( $450\text{ }\mu\text{m} \times 900\text{ }\mu\text{m}$ ), where the pixels are separated by 100  $\mu\text{m}$ , with integrated front-end electronics, guard rings, and 9 independent front-end channels. A 2  $\mu\text{m}$  width shallow p-Stop surrounds a pixel sensor at a distance of 15  $\mu\text{m}$  to introduce a p-Stop inter-pixel isolation technique. The technique is to guarantee a good isolation in case of oxide charge on surface due to a manufacturing process.

1000  $\Omega\text{cm}$  bulk resistivity wafer was chosen to achieve full depletion voltage at 100 V and sufficient electric field inside the sensor at high operation voltage. Even higher bulk resistivity is worthy to be considered, however the performance of the electronics is not guaranteed above 1000  $\Omega\text{cm}$  bulk resistivity.

## 6.2 Measurement

Two types of the analog prototype were fabricated with 1000  $\Omega\text{cm}$  bulk resistivity wafer and a SiGe-HBT process by the SG13S technology from IHP microelectronics. One is a thin backside processed chip (100  $\mu\text{m}$  thick, backside metallization to connect the backside to the ground), and the other is a standard-thickness chip (700  $\mu\text{m}$ ) without backside processing. Measurements with the thin chip were performed in order to study the functionality and the operating conditions for a test beam measurement of the efficiency and the time resolution with the un-thinned chip.



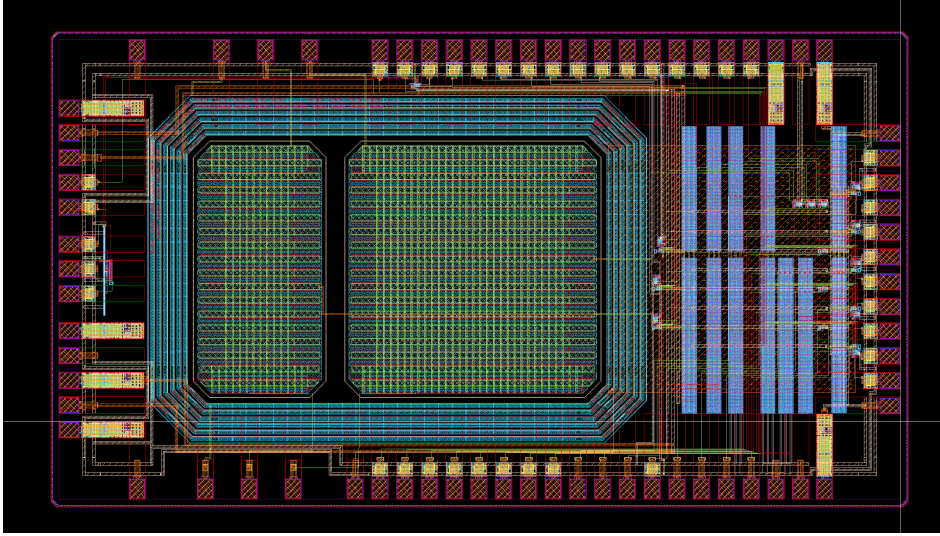


Figure 6.5: Layout of 1st ASIC demonstrator.

### 6.2.1 I-V Measurement of the Thin Chip

The functionality of the guard ring was measured with a wafer-probing station at University of Geneva, applying positive voltage to the pixels and the innermost guard ring of the thin chip. Figure 6.6 shows the measurement of the current as a function of the voltage, obtained for different values of the bias voltage to the innermost guard ring. The first current increase around 40 V is indicative of a problem with the backside processing of the chip. The breakdown voltage with the innermost guard ring floating was observed at 160 V, lower than expected in simulation, while it was beyond 200 V when 100 V were applied to the innermost guard ring. The discrepancy can be explained by the higher electric field at the corners of the pixel, which are shaped with an angle of 135 degrees instead of the straight edge used by the TCAD simulation. Nevertheless, the possibility to apply a bias voltage on the innermost guard ring allowed for compensation of this effect.

### 6.2.2 Edge Laser TCT Measurement of the Un-thinned chip

The thickness of the backend of the line (BEOL) is approximately 15  $\mu\text{m}$ , hence the 100  $\mu\text{m}$  thickness sensor is fully depleted when the depletion length is longer than 85  $\mu\text{m}$ . The full depletion voltage calculated from equation (5.8) for 1000  $\Omega\text{cm}$  resistivity and 85  $\mu\text{m}$  length is approximately 60 V, while the I-V curves indicate that full depletion is reached at 40 V. An edge laser TCT measurement was performed in order to observe the depletion length and to explain the discrepancy.

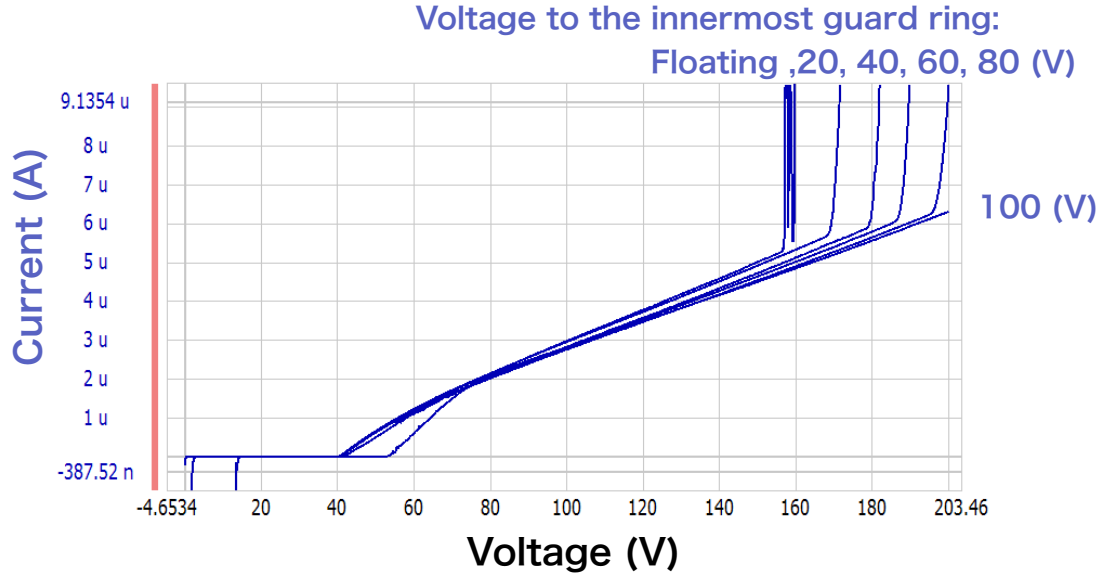


Figure 6.6: Current measurement as a function of voltage. The 6 lines from left to right correspond to the voltage applied to the innermost guard ring (Floating, 20, 40, 60, 80, 100 V).

A pulsed IR laser (1064 nm) was injected from the edge side of the large pixel and the collected charge in the electrodes was measured. Figure 6.7 shows the setup of the measurement. The laser beam divided by the mirror was monitored for the calibration. Since the PCB used in the measurement was designed originally for HV-CMOS sensor [52], positive high voltage cannot be applied to the chip. The PCB with device under test (DUT) chip is able to move with 1  $\mu\text{m}$  step to change the position of the laser beam injected. The chip was cooled at  $-30^\circ\text{C}$  during the measurement. As shown in figure 6.8, the charge was collected when the laser passed the depletion region. The dark region structured like a scratch in the center is due to the absence of the edge polish, however the effect is negligible for the measurement of the depletion length. The FWHMs of the charge collection distributions correspond to the depletion lengths at each high voltage. The resistivity given by the depletion lengths and the bias voltages corresponds to  $1500\ \Omega\text{cm}$ , which is 1.5 times larger than the designed value. The  $1500\ \Omega\text{cm}$  bulk resistivity is in good agreement with the 40V full depletion voltage for 85  $\mu\text{m}$  length.

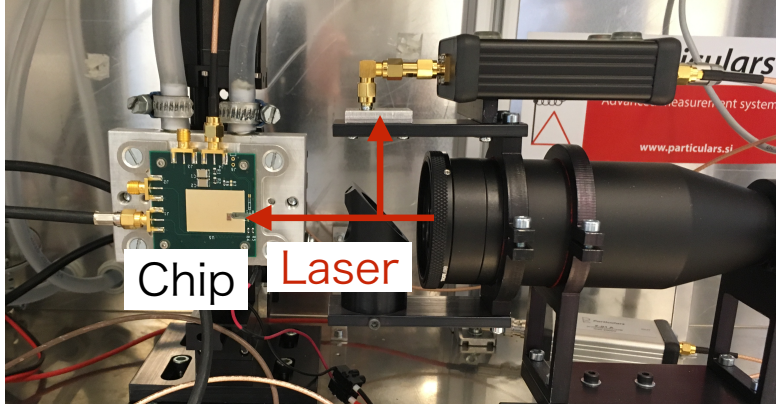


Figure 6.7: Setup of the edge laser TCT measurement.

### 6.2.3 Electronics Performance with an External Sensor

The performance of the front-end electronics of the chip was measured. The chip was connected to an external sensor, a matrix of  $5 \times 5$  pixels. The test chip and the external sensors (pixel size:  $1 \text{ mm} \times 1 \text{ mm}$ , thickness:  $100 \mu\text{m}$ ) were glued on a test board and wire-bonded.

Figure 6.9 shows the result of the threshold scan. The distribution is fitted as an error function, where  $\sigma_v$  corresponds to the standard deviation of the threshold value due to the front-end noise.

Measurements with electrons from a  $^{90}\text{Sr}$  source were performed to study the capability of the electronics to distinguish the signals generated by the particles from the electronics noise. Figure 6.10 shows the distribution of the amount of charge deposited in the sensor from a  $^{90}\text{Sr}$  source in Geant4 simulation. The most probable value (MPV) of the distribution  $Q_{\text{peak}}$  was estimated as following:

$$Q_{\text{peak}} = 1.776 \pm 0.008 \text{ fC} . \quad (6.1)$$

An Equivalent Noise Charge (ENC) of the preamplifier is given by

$$\text{ENC} = \frac{\sigma_v}{A} Q_{\text{peak}} , \quad (6.2)$$

where  $A$  (mV) is the amplitude of the signal pulse. Measurement with a  $^{90}\text{Sr}$  source showed  $A = 62 \pm 2 \text{ mV}$ , hence ENC of the amplifier  $717.9 \pm 0,007$  electrons RMS with  $1 \text{ pF}$  was derived.

### 6.2.4 A Testbeam Experiment of the Un-thinned Chip

The I-V measurement shows the possibility to perform a test beam measurement with the un-thinned chip at a high bias voltage. A testbeam experiment was

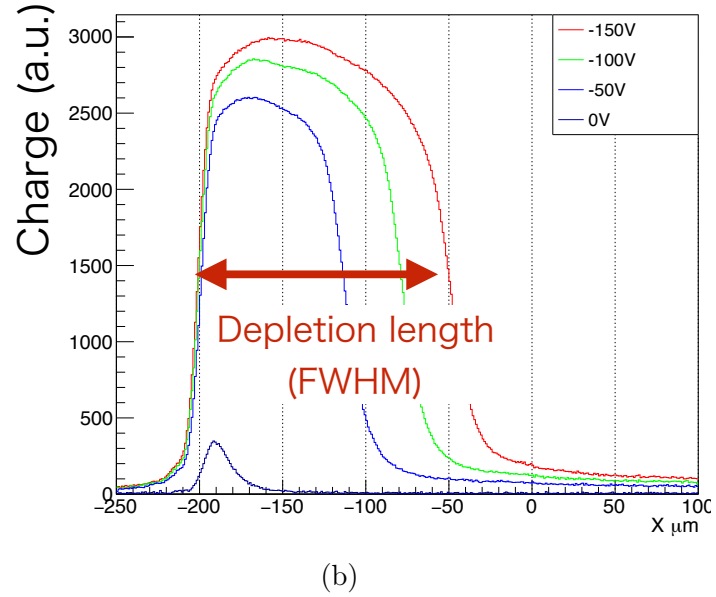
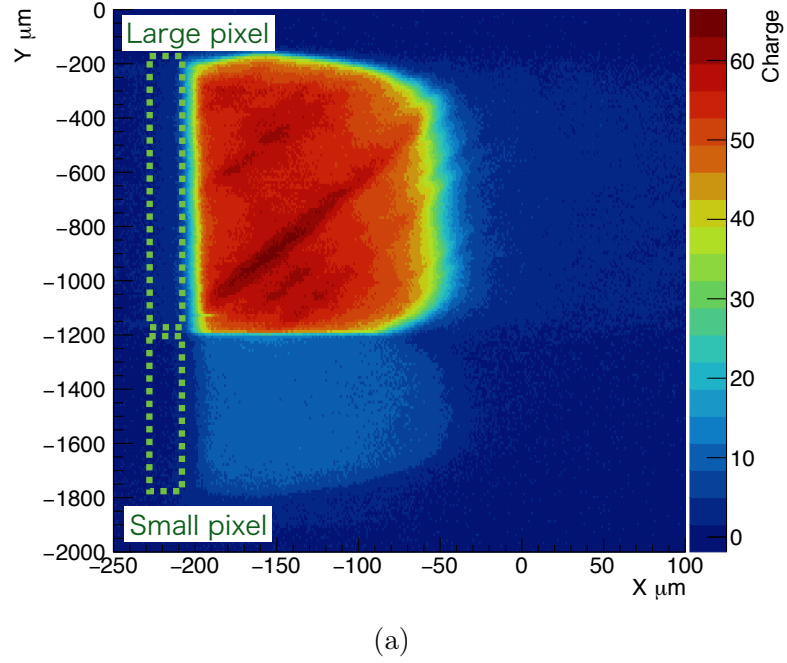


Figure 6.8: A charge collection distribution of edge laser TCT measurements with the potential at  $-100\text{ V}$  (a) and the projections of the charge collections for the large pixel sensor with the different potentials (b). Dashed rectangles represent the regions where the electrodes of the pixels are supposed to be placed. Charge collection was observed in the depletion region of the large pixel. The smaller charge collection in the depletion region of the small pixel is due to the charge sharing between the two pixels. The depletion lengths correspond to the FWHMs of the distributions.

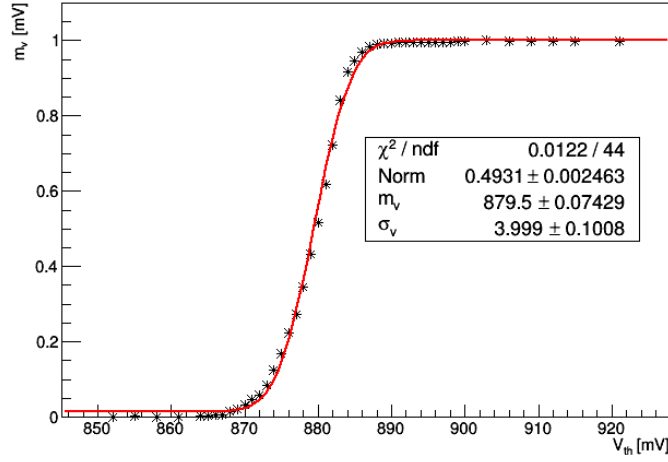


Figure 6.9: Threshold scan of the external sensor. The distribution is fitted as an error function to estimate the noise of the front-end electronics. An ideal sensor with no noise would produce a perfect step function.  $m_v$  is the mean value of the error function and  $\sigma_v$  is the standard deviation of the threshold value due to the front-end noise.

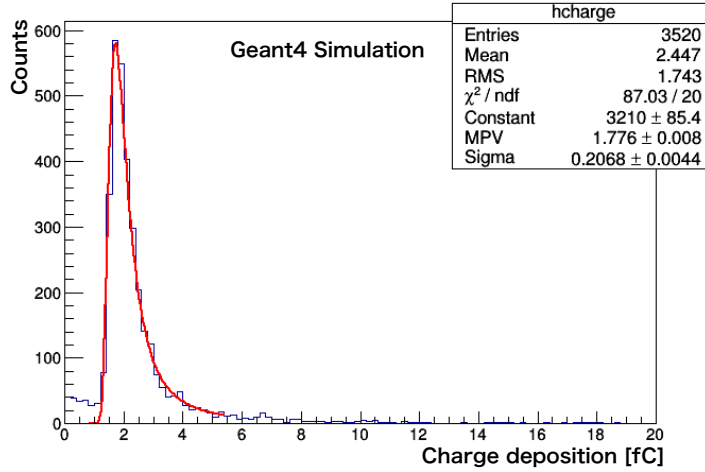


Figure 6.10: Charge deposition from a  $^{90}\text{Sr}$  source in Geant4 simulation. Most probable value (MPV) of the distribution is  $1.776 \pm 0.008$  fC.

performed with pions with momentum of 180 GeV/c at the CERN SPS to study the efficiency and time resolution of the un-thinned chip. The sensor was operated at a voltage of 160 V for the pixels and 120 V for the innermost guard ring. The electric field in the un-thinned analog prototype chip is not uniform in depth and is not large enough to saturate the carrier drift velocity, as shown in figure 6.11. These effects are expected to degrade the timing performance of the the un-thinned sensor.

Figure 6.12 shows the setup of the testbeam experiment. The two un-thinned chips were under test and the chips were aligned on the beam line. The discriminator threshold was set individually for each readout. A 50  $\mu\text{m}$ -thick Low Gain Avalanche Detector (LGAD) sensor produced by CNM [53] was placed downstream of the chips under test as a reference for the timing measurement. The LGAD sensor was operated at 230 V and is expected to have 30 ps time resolution with the hadron beam. The three sensors were placed downstream of the Geneva FE-I4 telescope [54], which provides the trigger and the tracking information of the beam.

## Efficiency

The tracks of the pions were reconstructed by hit informations from the telescope planes. The reconstructed tracks were required to pass through the region of the pixels on the chips under test and efficiency was obtained by calculating the fraction of the number of selected tracks detected by the sensor. Figure 6.13 shows the efficiency map of the chips under test. The areas contoured in black correspond to the region of the pixels to select the reconstructed tracks. The efficiency is  $(99.79 \pm 0.01)\%$  for the upstream chip and  $(99.09 \pm 0.04)\%$  for the small pixel of the downstream chip. The red dashed rectangle represents the LGAD active area on the sensors. The efficiency of the downstream chip increased to  $(99.88 \pm 0.04)\%$  after requiring hit on the LGAD sensor. This is because multiple scattering events on the upstream chip degraded the tracking performance of the telescope, hence the efficiency for the downstream chip was underestimated.

## Time Resolution

The area contoured in red solid line in figure 6.13 represents the region of interest for the timing study. ToT distribution of the small sensor of the upstream chip and time difference between the sensor and the LGAD sensor are shown in figure 6.14. A polynomial function was fitted to the time walk distribution (figure 6.14b) and the parameters of the fitted function were used to correct the time walk effect.



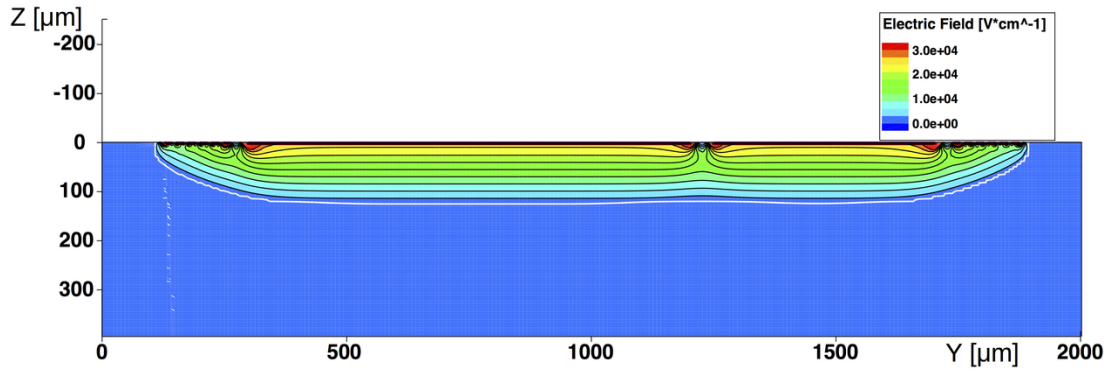


Figure 6.11: Simulation result of electric field distribution on the cross section of the un-thinned chip for a positive bias voltage of 160 V applied to the pixels. White line ( $\sim 130 \mu\text{m}$ ) shows the edge of the depletion region of the sensor.

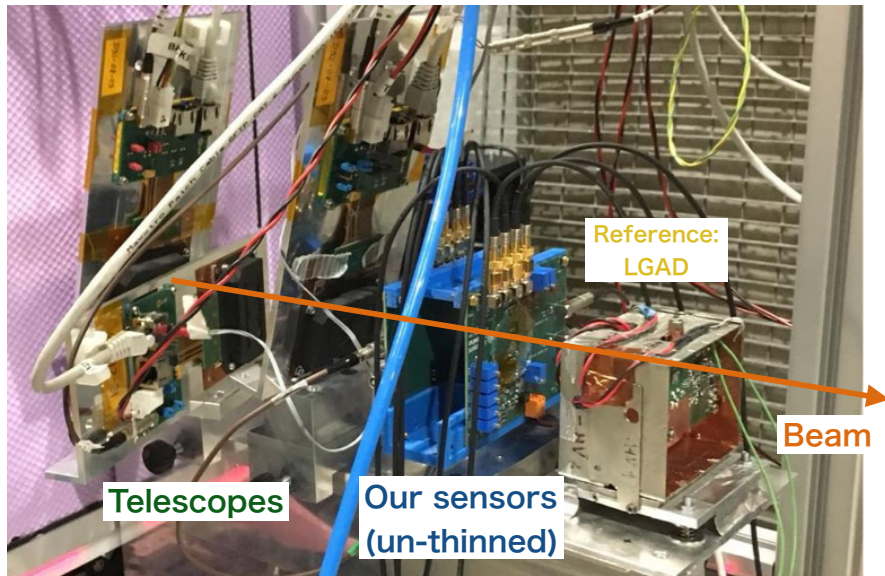
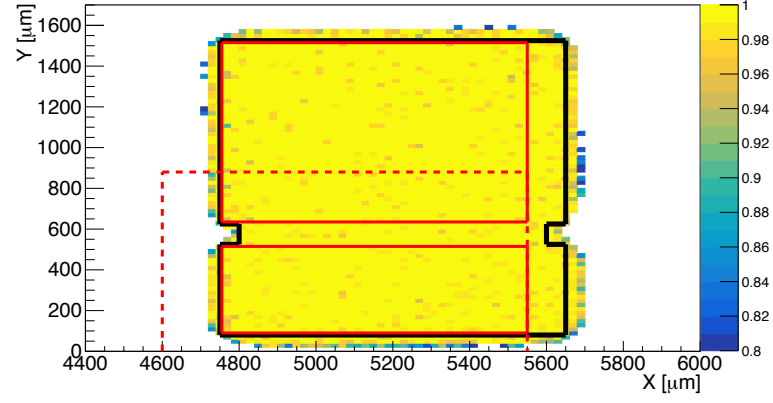
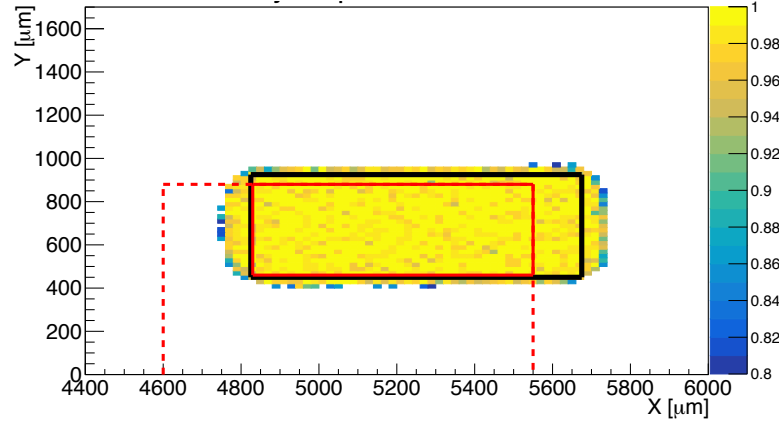


Figure 6.12: Setup of a test beam measurement



(a)



(b)

Figure 6.13: Efficiency map of the upstream sensor (a) and the downstream sensor (b). The area contoured in black represents the event selection of reconstructed tracks. The red dashed rectangle represent the projection of the LGAD active area on the monolithic chips. The rectangles in red solid line correspond to the region of interest for the timing study. Only small pixel was readout for the downstream sensor.



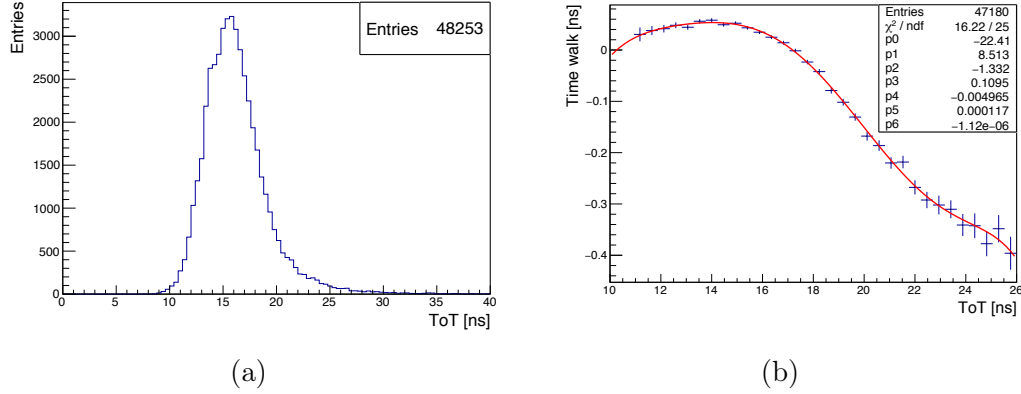


Figure 6.14: ToT distribution of the small pixel of the upstream sensor (a) and the time difference distribution between the small pixel and the LGAD as a function of ToT, fitting with a polynomial function (b).

Figure 6.15 shows the time difference between the small pixel from the upstream sensor and the LGAD sensor after the time walk correction. Approximately 220 ps time resolution of the small sensor of the upstream chip was measured. Measured time resolution is summarized in table 6.1. Approximately 20% worse time resolution for large sensor was observed with respect to small pixels, while the two small pixel sensors showed similar time resolution. This is probably caused by larger ENC, which depends on the pixel capacitance of the sensor. In addition, non-uniformity of the electric field due to the absence of the wafer thinning and the backside processing may further degrade the timing performance.

Table 6.1: Measured time resolution for the analog prototype chip

Pixel	Time resolution (ps)	Capacitance (pF)
Downstream small	$202.3 \pm 0.8$	0.8
Upstream small	$219.0 \pm 0.7$	0.8
Upstream large	$265 \pm 1$	1.2

### 6.3 Discussion

The achievements of the measurements of the analog prototype are summarized as follows:

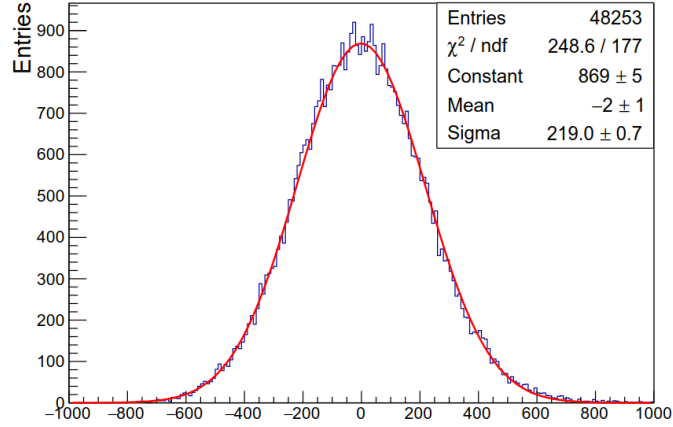


Figure 6.15: Time difference between the small pixel from the upstream sensor and the LGAD sensor.

1. Thanks to the dedicated guard ring, the prototype chips were operated at a high voltage of 160 V. The I-V measurement shows the possibility to control the breakdown voltage by applying the high voltage to the innermost guard ring.
2. Edge laser TCT measurement helped to understand the discrepancy of the full depletion voltage and showed the unexpected larger 1.5 times higher resistivity wafer ( $1500 \Omega\text{cm}$ ).
3. Test of electronics performance using a  $^{90}\text{Sr}$  source showed the expected noise performance of the preamplifier (700 electrons with 1 pF).
4. Efficiency and time resolution of the sensor were studied in detail at a test-beam experiment at CERN SPS. Almost full efficiency ( $> 99.7\%$  efficiency) was observed for the reconstructed tracks and approximately 200 ps time resolution was measured.

For the ASIC demonstrator, the number of pixels will be increased, hence the parasitic capacitance may increase due to more complex and dense routing from the pixel sensors to the front-end electronics. Therefore, it was decided to make the pixel size smaller ( $470 \mu\text{m} \times 470 \mu\text{m}$  with  $30 \mu\text{m}$ ) to reduce the total capacitance. The new inter-pixel spacing leads to a small modification of the guard ring design and p-Stop isolation, which will be discussed in Chapter 7.1.

# Chapter 7

## ASIC Demonstrator Development

### 7.1 Design

The ASIC demonstrator chip was designed in order to test the main elements of the final TT-PET chip. It has all the circuitry of the TT-PET sensor with a small size matrix and uses all the design blocks foreseen for the final chip. The ASIC post-processing is the same that is expected for the TT-PET sensor.

#### 7.1.1 Layout

Figure 7.1 shows the layout of the chip, which is composed of 30 n-on-p pixels of  $470 \times 470 \mu\text{m}^2$  area with  $30 \mu\text{m}$  inter-pixel spacing. Each pixel includes a SiGe-HBT preamplifier, a fast discriminator and an 8-bit calibration DAC for threshold equalization. A single 50 ps binning TDC, logic and serializers are placed in the periphery of the chip.

As shown in figure 7.2, the p-stop line between the pixels and the innermost guard ring was removed in order to improve the capability to control the electric field in the region by applying voltage to the inner most guard ring. Figure 7.3 shows the schematic cross section of the inter pixel region in the analog prototype and ASIC prototype. Due to the small inter pixel spacing, it becomes difficult to put p-Stop line surrounding each pixel. Hence, the p-Stop lines in the inter-pixel region were combined into a single line. Since the p-Stop line is highly doped, the isolation in case of oxide charge is expected to be functional enough even in a combined single line. The width of the p-Stop line and the distance from the pixel are not modified from the design of the analog prototype.

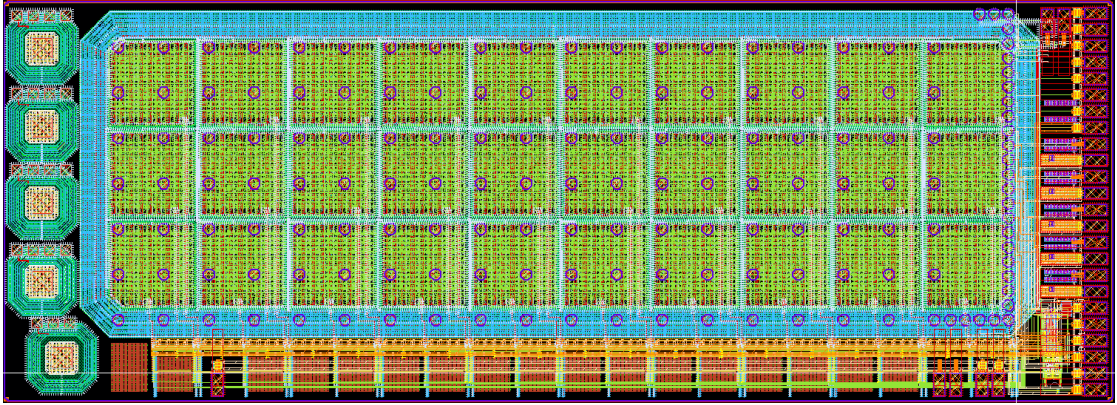


Figure 7.1: Layout of ASIC demonstrator chip. The  $3 \times 10$  pixel matrix (yellow green) is electrically isolated from the front-end electronics in the periphery of the chip by the guard rings (white blue). On the left, five guard ring structures are designed for test.

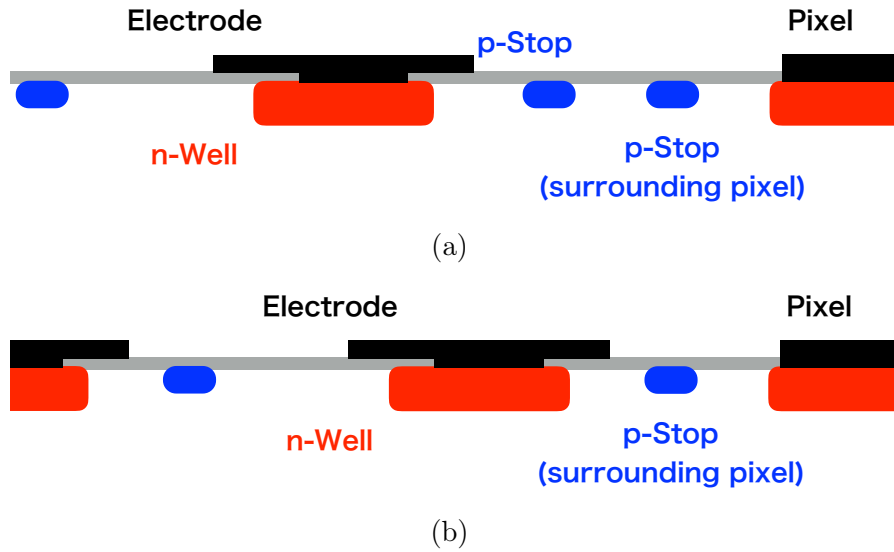


Figure 7.2: Design of the guard ring structure around the innermost guard ring for the analog prototype (a) and for the ASIC demonstrator (b). The p-Stop implant of the innermost guard ring was removed to suppress the electric field.

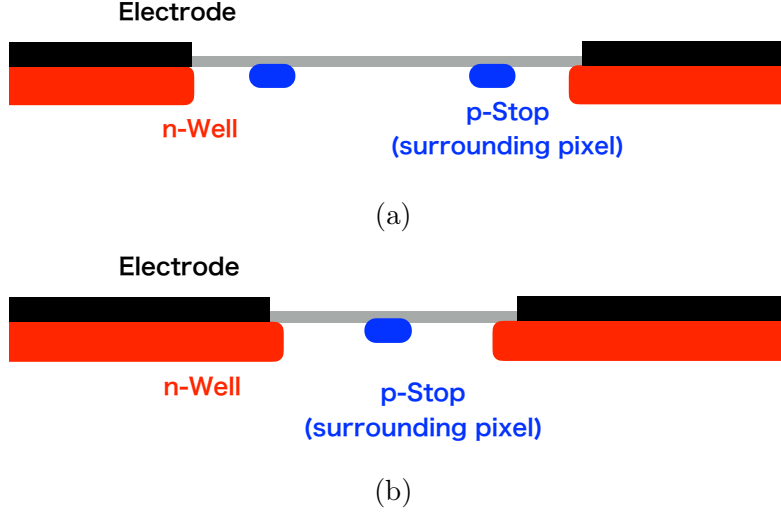


Figure 7.3: Schematic cross section of p-Stop isolation for the analog prototype (a) and for the ASIC demonstrator (b).

### 7.1.2 Readout logic

Figure 7.4 shows a block diagram of the readout logic of the chip. The digitized signals from the pixels are multiplexed to the single TDC. In case of multiple hits, only the hit from the pixel which has the lowest column and row identifier is registered, while the timing information of the first pulse is converted into the TDC. Hence, if the first hit is not from the pixel which has the lowest column and row identifier in the multiple hits, the identification of the pixel does not work properly. The 50 ps binning TDC measures both the time of arrival (ToA) and the time of threshold (ToT) for time walk correction.

The timing delay between the pixels exists due to the different time skew of the multiplexing paths. The time skew effect is minimized by the optimization in the layout and is corrected in the calibration in the offline analysis.

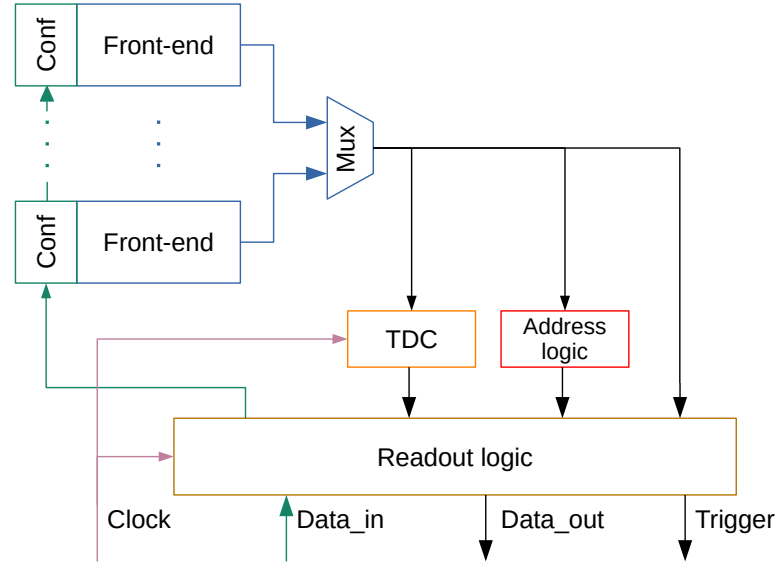


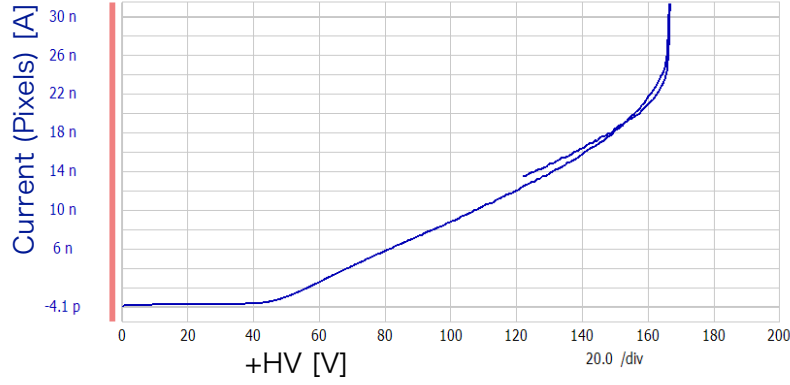
Figure 7.4: Block diagram of the readout logic of the 2nd ASIC demonstrator chip. Multiplexed digital signals are sent to the single TDC.

## 7.2 Measurement

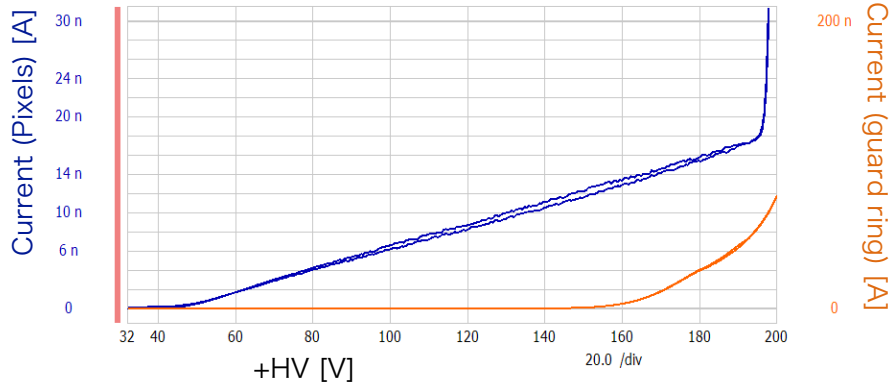
The monolithic chips were fabricated and thinned to 100  $\mu\text{m}$ . The backside was implanted with the p-side ohmic contact to avoid large leakage current at full depletion as seen in the analog prototype.

### 7.2.1 I-V Measurement

Figure 7.5 shows the the current of the chips as the function of the high voltage, measured on a wafer-probing station at room temperature (25  $^{\circ}\text{C}$ ). As for the analog prototype, current shift was observed at 45 V but the subsequent current increase was a factor 1000 times smaller than the analog prototype thanks to the p-side ohmic contact on the backside, that does not allow the depletion region to come in contact with the backside metallization. The measured leakage current, which is less than 0.6 nA/channel, has negligible impact on the chip performance since the sensor is capacitively coupled to the front-end electronics and the current is too small to introduce shot noise.



(a)



(b)

Figure 7.5: Current measurement as a function of voltage (HV) with the floating guard rings (a) and with the potential at  $(HV - 25)V$  for the innermost guard ring. (b). The blue lines show the current on the pixels and the orange line shows the current on the innermost guard ring as a function of voltage applied to the pixels.

## 7.2.2 A Testbeam Experiment

The ASIC demonstrator chip was tested with pions with a momentum of  $180 \text{ GeV}/c$  at the CERN SPS beam test facility to study the efficiency and the time resolution of the ASIC demonstrator chip. The same tracking telescope [55] used for the analog prototype provided external trigger (see figure 7.6) and particle track parameters and three demonstrator chips were read out by a system developed at the DPNC with a custom firmware. Positive  $180 \text{ V}$  was applied to the pixels and the backside of the chip was connected to ground. The amplifiers were operated at two working points with different power consumptions:  $160 \mu\text{W}/\text{channel}$  and  $350 \mu\text{W}/\text{channel}$ .

Four of the pixels (the three pixels of the rightmost column and the bottom pixel in the adjacent column in figure 7.7) were masked on hardware during the data acquisition due to noise induced from the the single-ended clock line. The small octagonal bump-bonding pads around the pixels causes electrical coupling between the pixels and the clock line through the I/O pads (see figure 7.7). In the final chip, these bump-bonding pads will be removed as a wire-bonding technique was chosen and the I/O and clock lines will be differential further reducing parasitic coupling.

### Efficiency

Figure 7.8 shows the pixel efficiency map of one of the chips at the  $160 \mu\text{W}/\text{channel}$  working point. The four masked pixels are indicated in figure. As for the test of the analog prototype, a region of interest, delimited by the black full line in figure 7.8 was used. The efficiency of the three chips with the two different power consumption working points is summarized in table 7.1.

Table 7.1: Efficiency of the three demonstrator chips

Power consumption [ $\mu\text{W}/\text{channel}$ ]	Efficiency		
	Chip 0	Chip 1	Chip 2
160	$99.933 \pm 0.007$	$99.986 \pm 0.003$	$99.985 \pm 0.003$
375	$99.924 \pm 0.006$	$99.980 \pm 0.003$	$99.973 \pm 0.003$



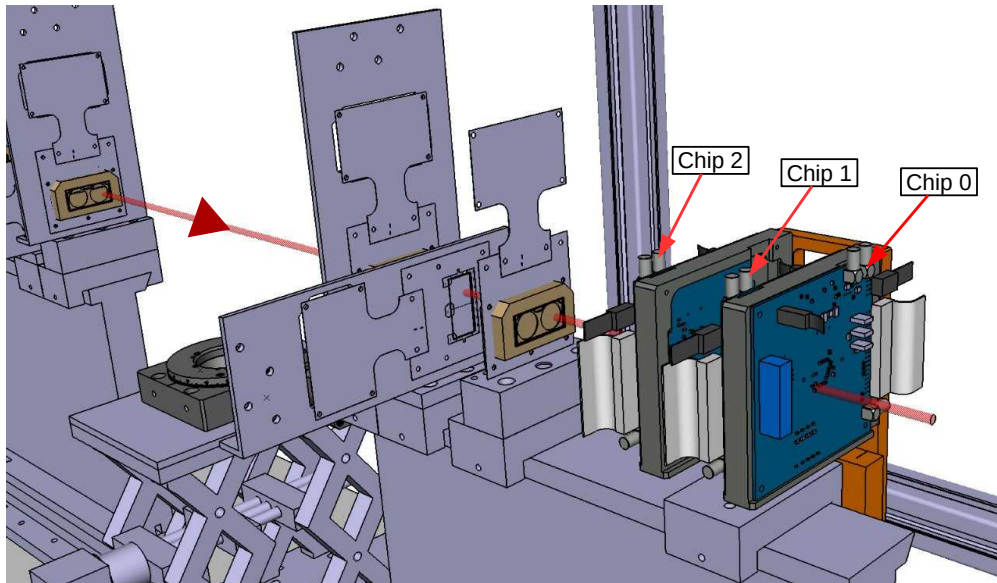


Figure 7.6: Setup at the test beam measurement. The particle beam (red arrow) passes through the devices under test after the tracking telescopes. The board of the chip 0 was rotated by  $180^\circ$  with respect to the other two boards.

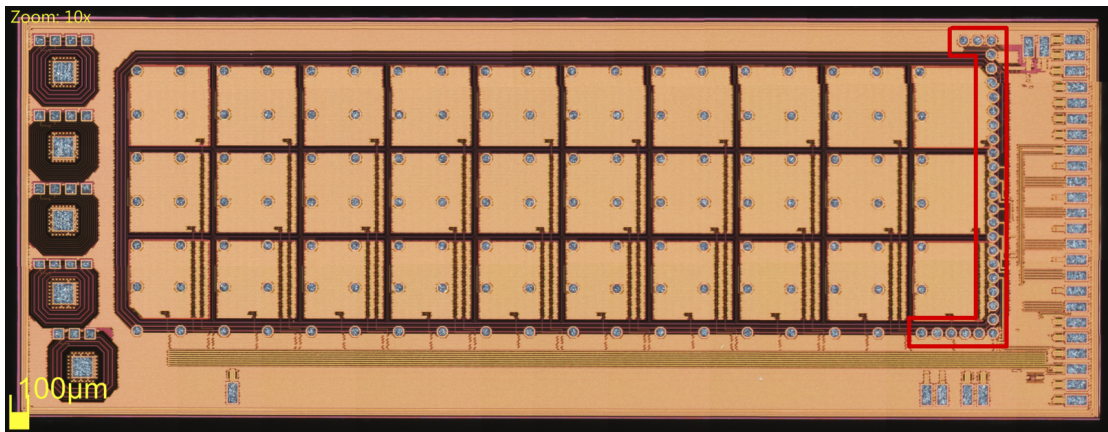


Figure 7.7: Microscope picture of the 2nd ASIC demonstrator chip. Small octagonal bump-bonding pads in red lines are connected to the rectangle wire-bonding pads on the right periphery of the chip.

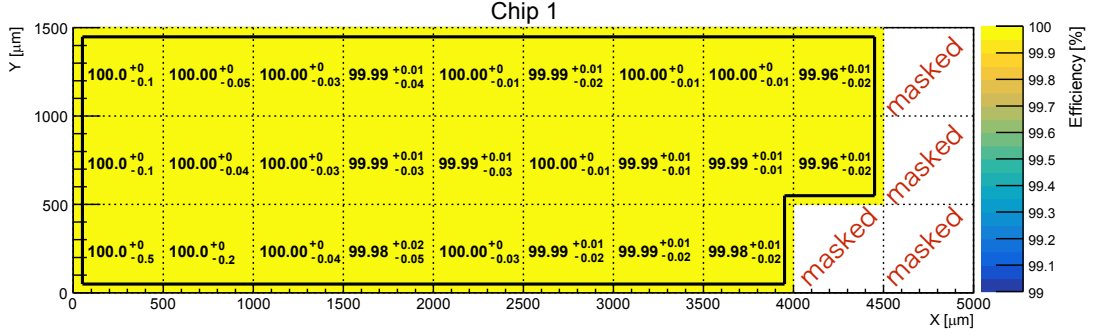


Figure 7.8: Efficiency map of the middle chip on the test setup (chip 1) with 160  $\mu\text{W}/\text{channel}$  working point. The dashed lines represent the separation between pixels. The continuous line represents the border of the area used for the efficiency calculation.

## Time Resolution

Figure 7.9a shows the ToT distribution for the hits recorded by one of the pixels of chip 1 at the low-power working point. Several peaks were found in the ToT distribution, which could be due to the new functions of the ASIC demonstrator since the effect did not exist in the analog prototype. The distribution peaking at 12 ns is considered as the charge deposition in the sensor by hadron beams. The bump visible between 14 ns and 17 ns can be explained by noise induced from the single-end clock line, affecting the grounding of the pixel matrix. The time walk correction was performed using ToT information from 2 ns to 40 ns, as shown in figure 7.9b. The red line is a polynomial function fitted to the distribution of the mean values of the time difference for TOT bins of 0.25 ns, represented by the green dots.

The average of the time-of-arrival for each pixel was adjusted to correct the time skew between different pixels of the same chip.

After the time calibrations, the time resolution was calculated from dividing the time difference between the two different chips by  $\sqrt{2}$ . Figure 7.10 shows the time resolution of the pixels for the chip in the center. A steady small worsening of the time resolution ( $\sim 10\%$  of the time resolution) towards the left of the map is visible. A hypothesis to explain the effect is the larger impedance of the ground line for the front-end channels far from the chip ground connection that is done in the right side of the chip.

The time resolution for the three chips with two different working point is summarized in table 7.2.

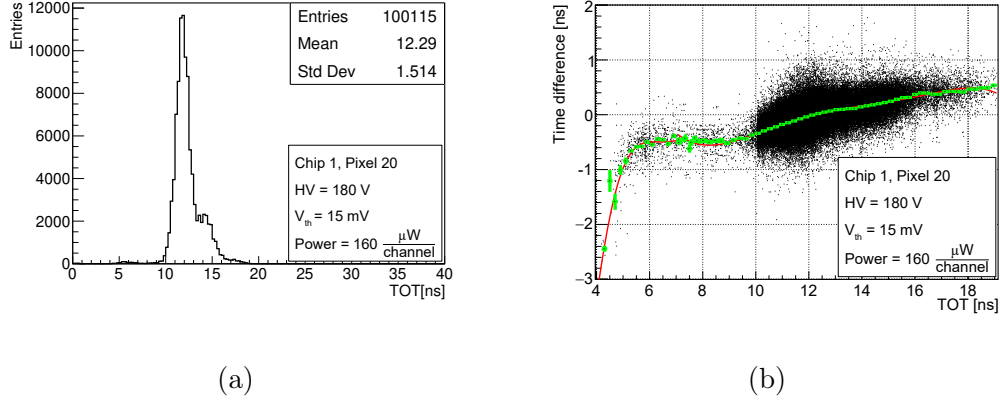


Figure 7.9: ToT distribution for the one of the pixels of chip 1 (a) and the time walk correction for the one of the pixels of chip 1 (b).

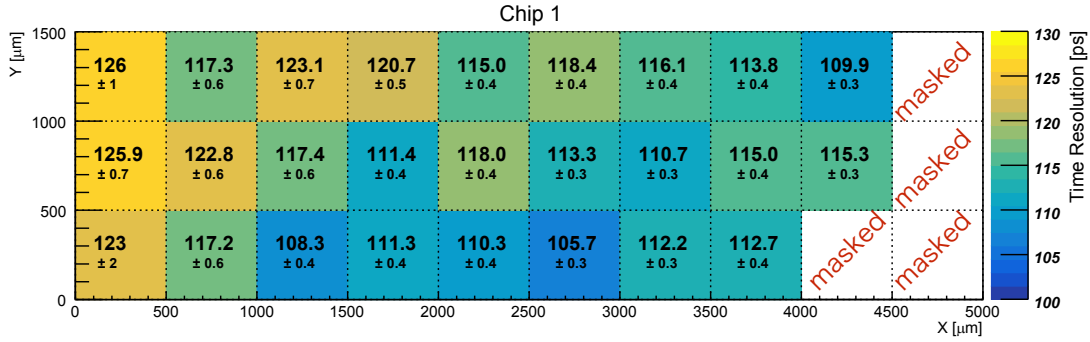


Figure 7.10: Time resolution (standard deviation) of the chip 1 in the test setup with  $350 \mu\text{W}/\text{channel}$  working point. The dashed lines represent the separation between different pixels. Only the statistical error is shown.

Table 7.2: Time resolution (standard deviation) of the three demonstrator chips

Power consumption [ $\mu$ W/channel]	Time resolution [ps]		
	Chip 0	Chip 1	Chip 2
160	127.3(2)	134.2(2)	137.2(2)
375	111.3(1)	116.7(1)	111.2(1)

## 7.3 Discussion

For the ASIC demonstrator, efficiency ( $> 99.9\%$ ) is improved compared to the analog prototype, which showed approximately 99.7% efficiency. It is inferred that the three times smaller inter pixel spacing and the combined single p-Stop line in the inter pixel region contribute to reduce the insufficient region of the sensor.

The time resolution is also improved thanks to the backside processing. Approximately 10% better time resolution was measured with larger power consumption working point, as expected in figure 5.13.

The measured time resolution is unprecedented result for the monolithic silicon pixel sensor without internal gain. However, four of the pixels must be masked on hardware due to the defects regarding to the single-end clock line and I/O. The defects would be related to the ToT distribution, which may degrade the time walk correction, though the issues will be addressed in the future processes.

## Chapter 8

# Characterization of the Annihilation Photon Detection System of the TT-PET Scanner

From the lab measurements and the test beam experiments, it was found that the ASIC demonstrator shows very high efficiency and time resolution. As part of this work, an experiment was performed to detect the photons from the  $\beta^+$  emission of a  $^{22}\text{Na}$  radioactive source and to measure the time resolution obtained by a pair of our demonstrator sensors. Chapter 8.1 will describe the detector and the experimental setup. The result of the time resolution and the annihilation photon detection efficiency will be discussed in Chapter 8.2 and Chapter 8.3, respectively.

## 8.1 Experimental Setup

### 8.1.1 Detector

The photon detector used for this test was designed based on the single photon detection layer of the TT-PET scanner, as shown in figure 8.1. The chip was glued on the  $50\text{ }\mu\text{m}$  lead foil, and then on the PCB, which has a rectangle hole to pass through annihilation photons. The epoxy glue was loaded with a powder of silver coated hollow glass microspheres. This electrically conductive glue was selected to produce an electrical connection between the chip backside metallization and the lead converter without absorbing the conversion electrons in high density silver grains. The thickness of the glue layer is expected to be approximately  $35\text{ }\mu\text{m}$  and very low density ( $\sim 1\text{ g/cm}^3$ ). A second  $50\text{ }\mu\text{m}$  lead foil was placed after the sensor to detect the electron bouncing back, as discussed in Chapter 5.3.2. The

lead foil was glued with the double-sided adhesive insulating tape (50  $\mu\text{m}$ ) to avoid electrical coupling between the pixels and the lead.

### 8.1.2 $^{22}\text{Na}$ Source

A  $^{22}\text{Na}$  source of 3.7 MBq produced by Eckert & Ziegler was used in the measurement. The decay scheme of the  $^{22}\text{Na}$  radioisotope is shown in figure 8.2. Approximately 90% of the disintegrations of  $^{22}\text{Na}$  consist of a  $\beta^+$  decay into an excited state of  $^{22}\text{Ne}$ , followed by emission of a  $^{22}\text{Na}$ . Figure 8.3 shows the geometry of the source. The radioactive isotope is distributed within 1 mm diameter sphere.

### 8.1.3 Experiment

The experiment was performed in a clean room of the department of nuclear and particle physics of University of Geneva, where radiation protection regulation requires having a dose rate in the environment surrounding the setup below 0.1  $\mu\text{S/h}$ . Thus, the experiment was performed in a lead box, as shown in figure 8.4. A metal was attached to the  $^{22}\text{Na}$  source "to be fished" from a container by a stick with a magnet, as described in figure 8.5. The position of the source was aligned by a micrometer screw, which sets the height of the stick.

The two detectors were placed at 14 mm distance from each other to detect annihilation photons in coincidence. The source was placed between the two detectors and the vertical position was aligned to maximize the coincidence rate of the two sensors. The chips were operated at 180 V with low power consumption working point (160  $\mu\text{W/channel}$ ), which is the target of the power consumption of the TT-PET scanner. The thresholds of the pixels were calibrated before the data acquisition to be a single hit noise rate lower than 0.1 Hz.

## 8.2 Annihilation Photon Detection Efficiency

### 8.2.1 Measurement

Since an additional 1275 keV photon is emitted with approximately 90% probability in a  $\beta^+$  decay of a  $^{22}\text{Na}$  radio isotope, the number of hits on a chip is given by

$$(2\epsilon_0 + 0.9\epsilon_1) \times A \times N_e , \quad (8.1)$$

## CHAPTER 8. CHARACTERIZATION OF THE ANNIHILATION PHOTON DETECTION SYSTEM OF THE TT-PET SCANNER

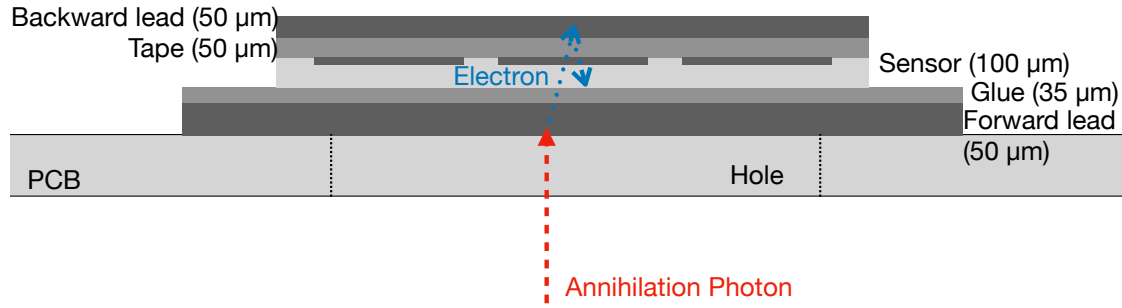


Figure 8.1: Schematic cross section of the annihilation photon detection system. The ASIC demonstrator was glued on the PCB with 35  $\mu\text{m}$  glue and 50  $\mu\text{m}$  lead foil for conversion from annihilation photon to electron. A second 50  $\mu\text{m}$  lead foil was stuck with 50  $\mu\text{m}$  double-sided adhesive tape for the case of electron reflection.

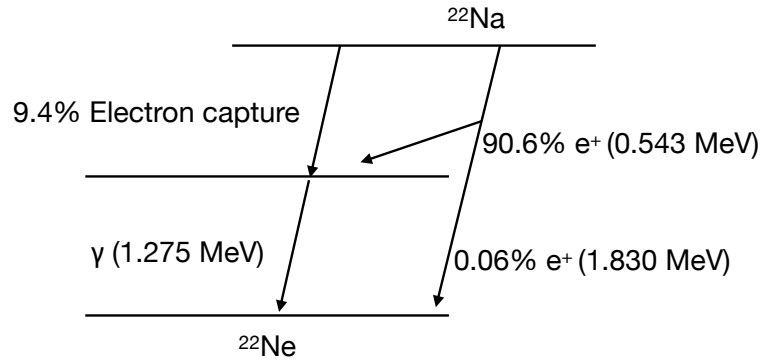


Figure 8.2:  $\beta^+$  decay scheme of the  $^{22}\text{Na}$

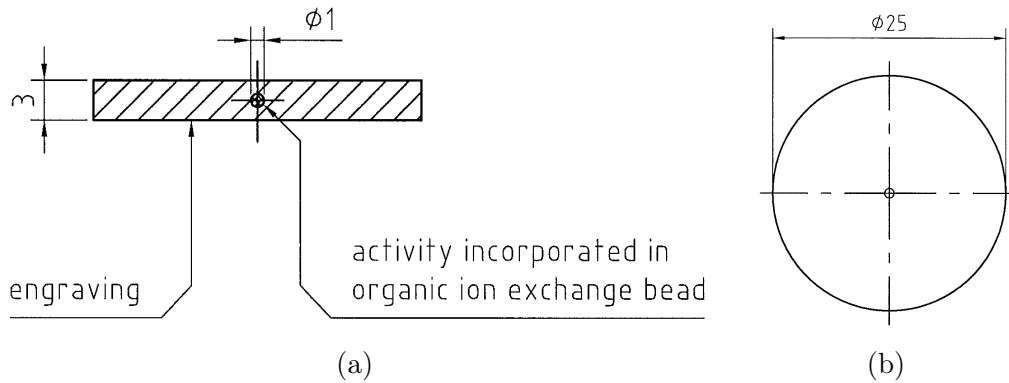


Figure 8.3: Front view (a) and top view (b) of geometry of a  $^{22}\text{Na}$  source. The radioactive source (1 mm diameter sphere) is embedded into the cylindrical acrylic case.



Figure 8.4: Experimental setup of the annihilation photon detection. A lead box for radiation protection (a) and the inside of the box (b). The two boards with the metal support structure were fixed and monitored by USB cameras after closing the cover of the box.

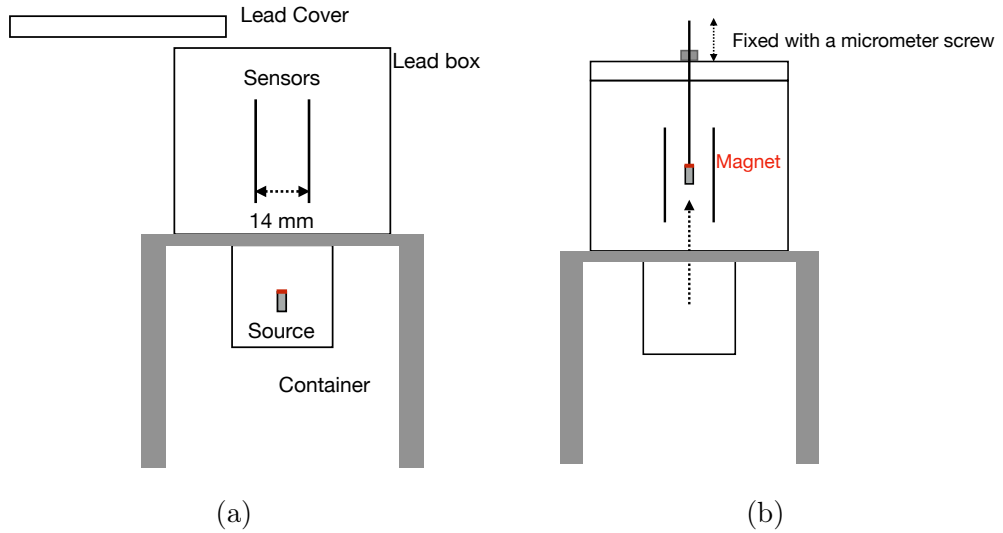


Figure 8.5: Schematic design of the experimental setup of the annihilation photon detection system. The radioactive source is isolated from the setup when opening the cover of the lead box (a). The source was extracted by a stick with a magnet and placed between the sensors during the measurement (b). The position of the source was aligned with a micrometer screw.



where  $\epsilon_0$  and  $\epsilon_1$  are the efficiency for a 511 keV photon and for a 1275 keV photon, respectively and  $A$  represents the acceptance of the chip for the source and  $N_e$  is the number of  $\beta^+$  decay.

Assuming that the accidental coincidences between one of the two 511 keV photons and the 1275 keV photon is negligible, the number of coincidences is represented by

$$2\epsilon_0^2 \times A \times N_e, \quad (8.2)$$

hence the ratio between the number of coincidences and hits on chip 1 is given by

$$R = \frac{\text{Number of coincidences}}{\text{Number of hits on chip 1}} \quad (8.3)$$

$$\sim \frac{2\epsilon_0^2}{2\epsilon_0 + 0.9\epsilon_1}, \quad (8.4)$$

hence the ratio  $R$  does not depend on the acceptance  $A$  and the  $\beta^+$  decay rate  $N_e$ <sup>1</sup>. As shown in figure 8.6, only one pixel of chip 1 was readout and provided the trigger. The ratio  $R$  on chip 0 was measured with different source positions along the z-axis. The origin position ( $z = 0$  mm) was defined as the position where the highest coincidence hit rate was observed. Figure 8.7 shows the measured hit distribution on chip 0 with the <sup>22</sup>Na source placed at  $z = 80$   $\mu$ m.

Figure 8.8 shows the efficiency as a function of source positions along the z-axis. The efficiency reaches the maximum value of 0.19% when the source was placed around  $z = 0$   $\mu$ m.

### 8.2.2 Simulation

A Geant4 Monte Carlo simulation was performed to verify the measurement and the effect of the mechanical misalignment of the source position. As shown in figure 8.9, the geometry of the measurement was reproduced in Geant4 simulation. The same physics interaction model as the one for the TT-PET scanner simulation was used. Figure 8.10 shows the ratio  $R$  defined in (8.3) with different source positions along the z axis. Simulation results with different horizontal source positions are summarized in Appendix B. 0.25% efficiency is expected at  $z = 0$   $\mu$ m and 0.15% efficiency is expected within  $\pm 500$   $\mu$ m of the source position variation along z-axis. Since the source position was fixed with a micrometer screw on the lead box,  $\mathcal{O}(100)$   $\mu$ m the simulation results are consistent with the measurement within a possible mechanical misalignment.

---

<sup>1</sup> $R = \epsilon_0$  when  $\epsilon_1 = 0$ , thus ratio  $R$  becomes efficiency for 511 keV photon  $\epsilon_0$ . In this study,  $R$  was used as tagged efficiency to characterize the performance of efficiency since 511 keV photon and 1275 keV photon cannot be distinguished.

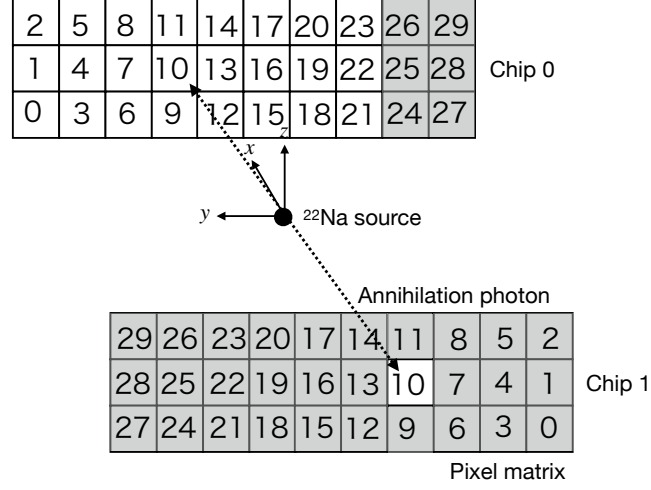


Figure 8.6: Pixel matrix for the efficiency measurement. Shaded pixels were masked.

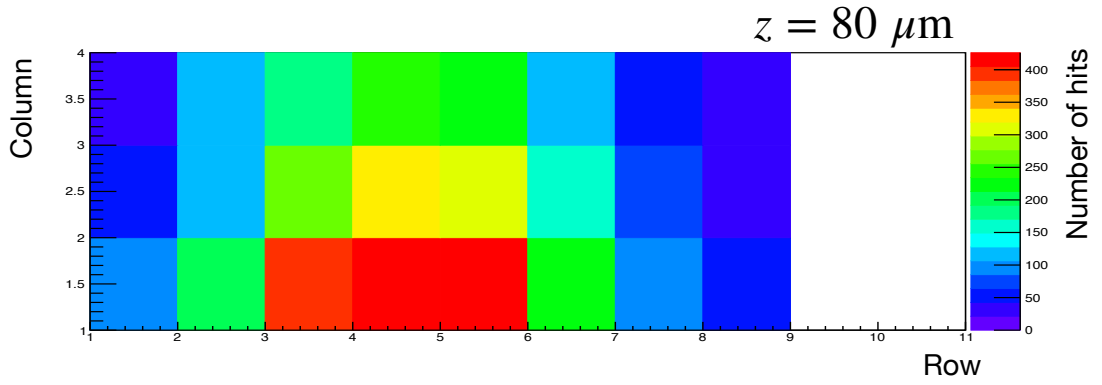


Figure 8.7: Hit distribution on chip 0 with the  $^{22}\text{Na}$  source positioned at  $z = 80 \mu\text{m}$

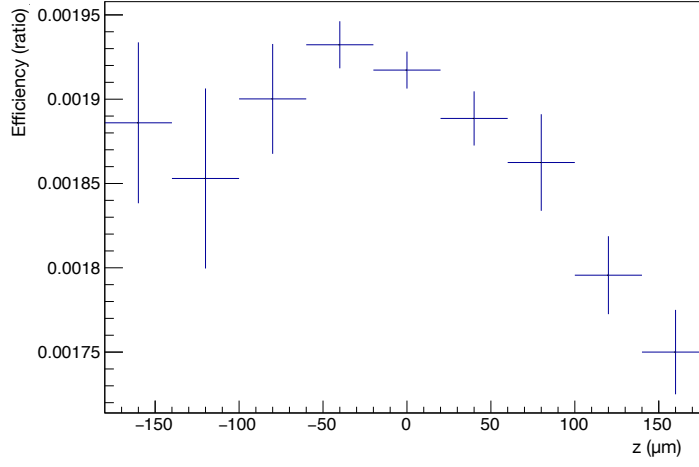


Figure 8.8: Annihilation photon detection efficiency as observed with the source in different positions along the  $z$ -axis. Approximately 0.19% efficiency was observed at  $z = 0 \mu\text{m}$  and the efficiency dropped as the source was moved away from the origin position. Only the statistical error is shown.

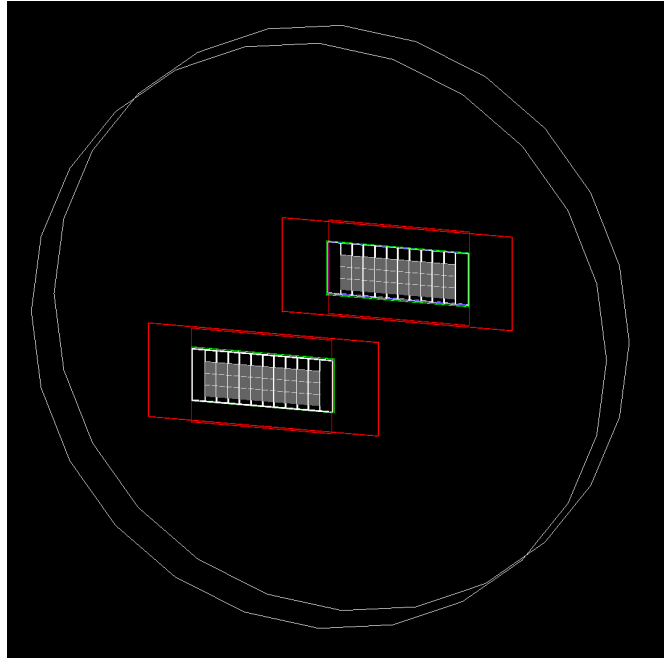


Figure 8.9: Visualization of the simulation setup of the annihilation photon detection system and the radioactive source.

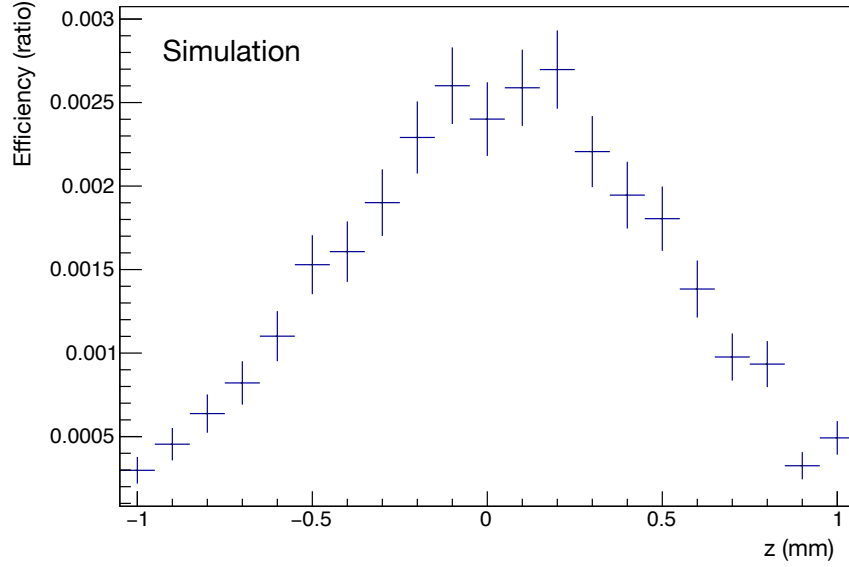


Figure 8.10: Simulation results of the annihilation photon detection efficiency with different positions along the z-axis (see Appendix B for horizontal positions).

### 8.3 Time Resolution

The time resolution of the annihilation photon detection system was measured in the same setup. The chips were operated at power consumption of  $160 \mu\text{W}/\text{channel}$ , which is the target of the TT-PET scanner and corresponds to 130 ps time resolution measured for minimum ionizing particles in the test beam experiment. 4 pixels in each chip were unmasked to avoid multiple hits on neighboring pixels, as shown in figure 8.11. The source position was aligned where the highest coincidence rate was observed.

A small defect on chip 1 was found on the TDC ring oscillator, as shown in figure 8.12. Due to the minor design flaw of the TDC, the counter had an uncertainty of 1 bit for the events recorded in one of the fourteen states (bin 9) of the TDC ring oscillator. The issue was removed by cutting the events of the bin number 9 in the analysis, and will be addressed in the final design of the chip.

Figure 8.13 shows the ToT distributions. A modulation of the ToT distribution for this demonstrator (which was already observed at the testbeam experiment) was observed, which limits the precision of the time walk correction and therefore the time resolution of this version of the sensor. The ToA was correlated with ToT0 and ToT1, both of which show a strong modulation effect, hence the time walk

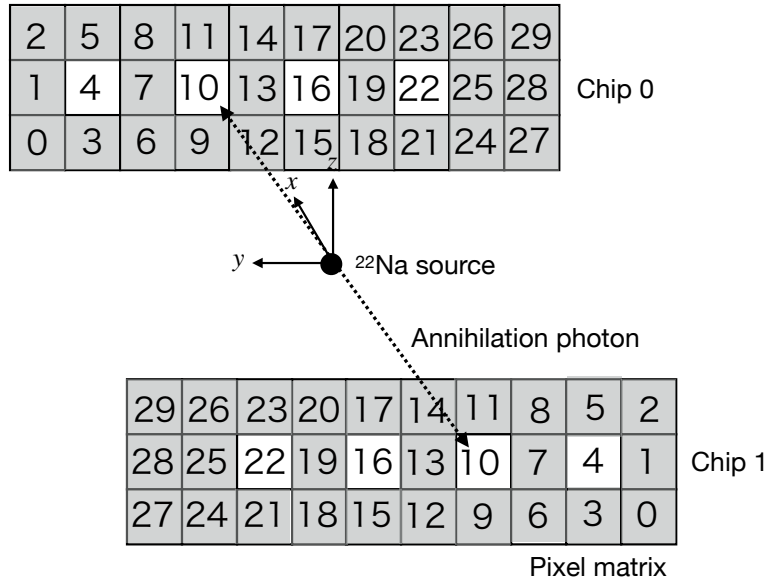


Figure 8.11: Pixel matrix for the timing measurement. Shaded pixels were masked.

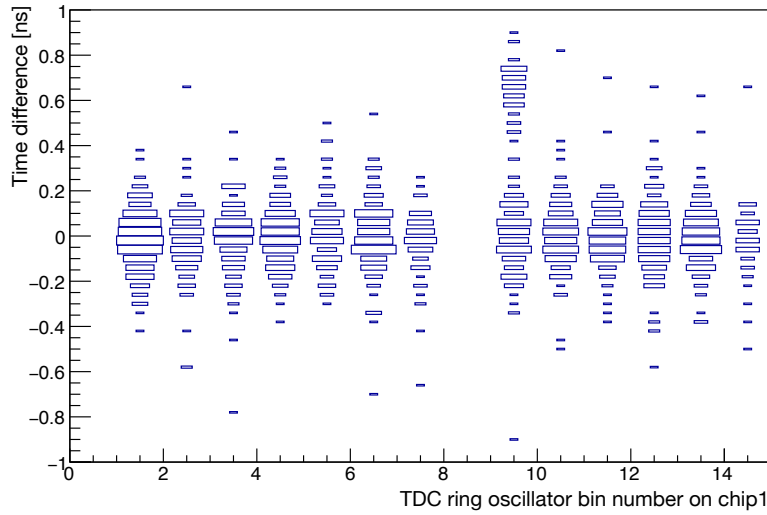


Figure 8.12: Time difference between chip 0 and chip 1 as a function of the status measured by the TDC ring oscillator on chip 1. The events of the bin number 9 were removed in the offline analysis.

correction of a chip affects the time walk correction of another chip. Therefore, the time walk correction for each individual chip, which was performed in the test beam experiment, does not work in this case. Two dimensional time walk correction was developed in this analysis to perform the time walk correction simultaneously on both chips. Assuming that the time informations between the two chips are not correlated, the time walk correction was performed with the fit function:

$$f(x, y) = c + a_1x + a_2x^2 + a_3x^3 + a_4x^4 + b_1y + b_2y^2 + b_3y^3 + b_4y^4, \quad (8.5)$$

where  $a_n$ ,  $b_n$  ( $n = 1, 2, 3, 4$ ) and  $c$  are the fitting parameters and  $x$  and  $y$  are the ToT values of the chip 0 and the chip 1, respectively. As shown in figure 8.14, the time walk effect was corrected with the two dimensional function  $f(x, y)$ .

Figure 8.15 shows the time difference after the time walk correction. A gaussian function was fitted in the region  $[-200 \text{ ps}, 200 \text{ ps}]$ . The time resolution of the sensor was derived by dividing the time difference by  $\sqrt{2}$ . The measured time resolution  $\sigma_t$  is given by

$$\sigma_t^2 = \sigma_{\text{sensor}}^2 + \sigma_{\text{TDC}}^2, \quad (8.6)$$

where  $\sigma_{\text{sensor}}$  is the time resolution of the sensor and  $\sigma_{\text{TDC}}$  is the time resolution of the 50 ps TDC expected to be approximately 14 ps. The sensor time resolution after the correction are summarized in table 8.1.

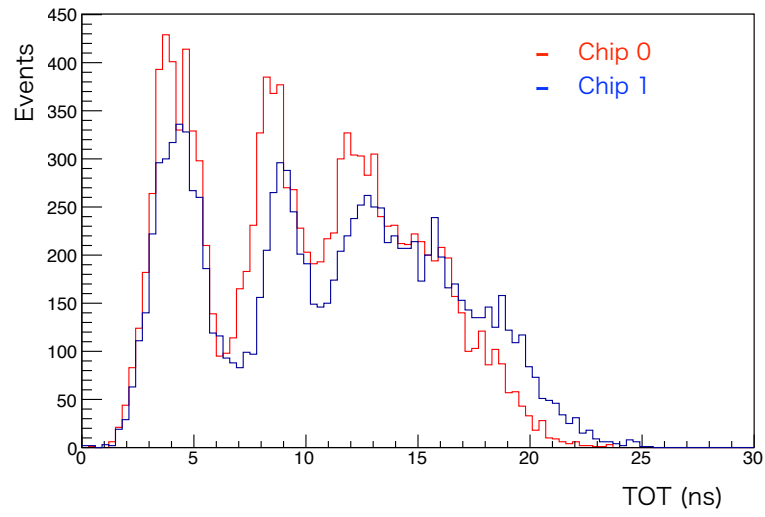


Figure 8.13: Time-over-threshold distributions on two chips. The ToT distribution shows peaks due to the defect of the single-end trigger line.

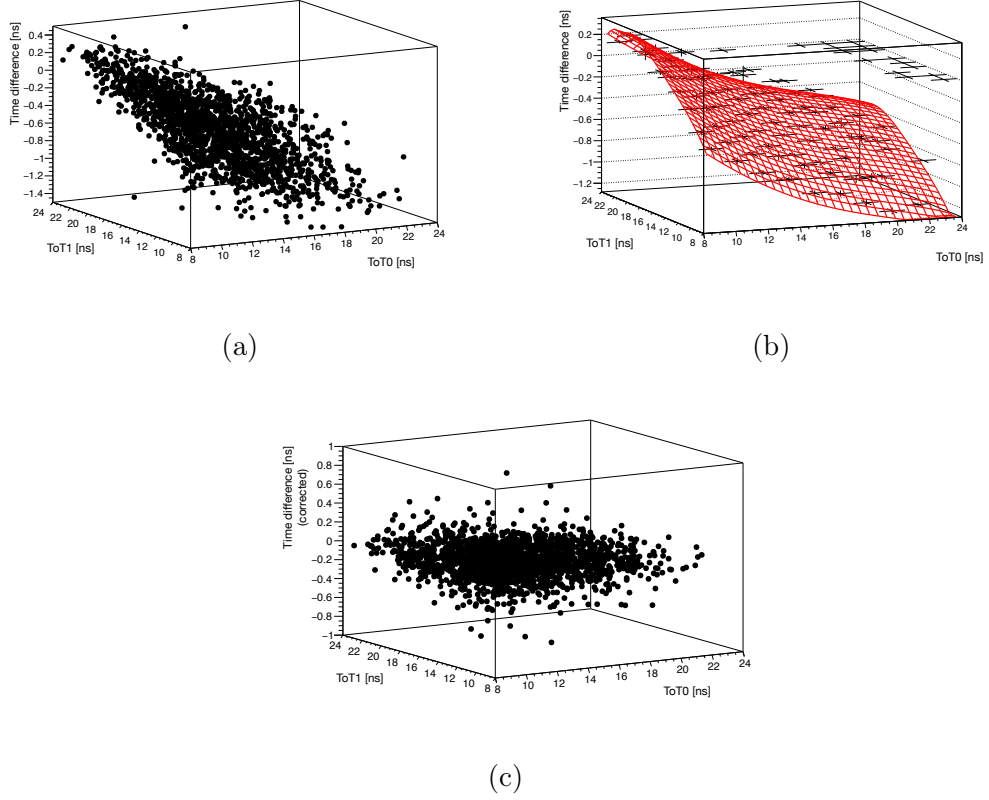


Figure 8.14: Two dimensional time walk correction. Time difference between chip 0 and chip 1 as a function of ToT on chip 0 (ToT0) and chip 1 (ToT1) (a), the two dimensional time walk correction function (b) and the distribution after the time walk correction (c).



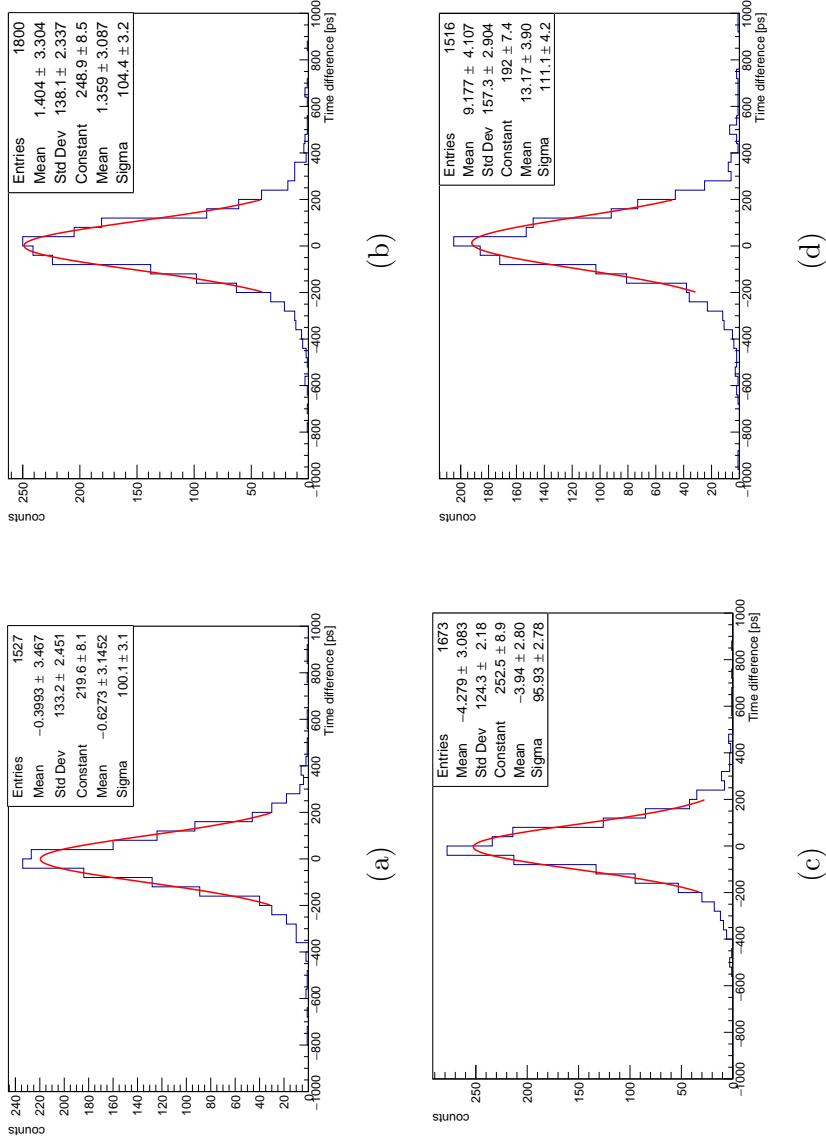


Figure 8.15: Time difference between chip 0 and chip 1 after time walk correction for pixels (4, 4): (a), (10, 10): (b), (16, 16): (c) and (22, 22): (d). The gaussian functions were fitted in the region  $[-200 \text{ ps}, 200 \text{ ps}]$  to calculate the time resolution of the chips.

Table 8.1: Time resolution (standard deviation) of the annihilation photon detection system. Only the statistical error is shown.

Pixels	Sensor time resolution ( $\sigma_{\text{sensor}}$ ) [ps]
(4, 4)	$68.0 \pm 2.2$
(10, 10)	$71.1 \pm 2.3$
(16, 16)	$64.8 \pm 2.0$
(22, 22)	$76.7 \pm 3.0$

## 8.4 Discussion

The result of the efficiency measurement is consistent with Monte Carlo simulation, hence the annihilation photon coincidence mechanism confirmed the feasibility of the TT-PET scanner. Measurement with  $\beta^+$  decay source without contamination of different photon emission and more mechanical precise measurement would improve the sensitivity of the efficiency measurement.

Approximately 70 ps (RMS) time resolution was observed and it is approximately two times better than the result of the testbeam experiment (130 ps at 160 pW/channel) thanks to the larger energy deposits from the 511 keV photons with regard to the minimum ionizing particles of the testbeam. Nevertheless the time walk correction was not fully effective due to the ToT modulation observed in this prototype. This effect due to minor issues in the sensor logic and I/O signal generation will be corrected in the final ASIC design.

# Chapter 9

## Conclusions

In this thesis, the expected performance of the Thin-TOF PET (TT-PET) scanner and the developments of the annihilation photon detection system with the fast timing monolithic silicon pixel sensors were studied.

The TT-PET scanner was designed to have very good Time-of-Flight (ToF) resolution (70 ps FWHM coincidence time resolution) and sensitivity for photon Depth-of-Interaction (DOI). Monte Carlo simulation was performed to study the expected performance of the TT-PET scanner. The expected Noise Equivalent Count Rate (NECR), which is proportional to the square of the Signal-to-Noise Ratio (SNR) of the reconstructed image, is 800 kcps with 50 MBq Fluorine-18 source. Thanks to the very good time resolution, the expected NECR can be even higher with stronger intensity of radioisotope. Image reconstruction with a maximum a posteriori probability estimation (MAPS) algorithm based on an iterative method with a statistical model was developed to see the full potential of the TT-PET scanner. The reconstructed image of a Derenzo phantom resolves 0.7 mm diameter structure on the whole view of the scanner thanks to the high granularity of the sensor and sensitivity of photon DOI. The comparison with the conventional scanners shows the outstanding performance of the TT-PET scanner for both spatial resolution and SNR.

Fast timing silicon monolithic pixel sensor and the annihilation photon detection system with the pixel sensors were developed. Silicon Germanium Hetero Bipolar Junction Technology (SiGe-HBT) from IHP microelectronics (SG13S process) was chosen for fast integration with large current gain and low power consumption. A Technology CAD simulation (TCAD) simulation was performed to design the sensor part of the SiGe-HBT process. The guard rings structure, the weighting potential and the capacitance (bulk and inter-pixel) of the sensor were studied with TCAD simulation to satisfy the requirement of the 100 ps time

resolution (standard deviation) for minimum ionizing particles (MIPs).

An analog prototype was produced made by two pixels and front-end electronics (bulk resistivity:  $\sim 1\text{ k}\Omega$ ) to prove the functionality of the guard rings and its performance. I-V measurements of an un-thinned prototype ( $700\text{ }\mu\text{m}$  thickness) were performed with a probe station. The breakdown voltage with innermost guard ring floating was measured at  $160\text{ V}$ . It is expected to be greater than  $200\text{ V}$  when  $100\text{ V}$  is applied to the innermost guard ring. Edge-laser Transient Current Technique (TCT) measurement was performed to study the depletion length of the sensor, which is equivalent to the bulk resistivity of  $1.5\text{ k}\Omega\text{cm}$ . Threshold scan with  $^{90}\text{Sr}$  showed an equivalent noise charge (ENC) of the preamplifier of approximately 700 electrons RMS with  $1\text{ pF}$  capacitance. A testbeam experiment at CERN SPS showed 99.8% efficiency and  $220\text{ ps}$  time resolution for MIPs in spite of the absence of thinning and the backside metallization.

The ASIC demonstrator, composed of 30 pixels and full electronics (preamplifier, discriminator, 8-bit calibration DAC and  $50\text{ ps}$  binning TDC), was designed to test the main elements of the final TT-PET chip. I-V measurements of a thinned demonstrator ( $100\text{ }\mu\text{m}$  thickness) confirmed the robustness of the chip up to a bias voltage of  $195\text{ V}$  and negligible leakage current ( $< 0.6\text{ nA/channel}$ ). A testbeam experiment at CERN SPS showed full efficiency and approximately  $130\text{ ps}$  time resolution with  $160\text{ }\mu\text{W/channel}$  power consumption and  $110\text{ ps}$  time resolution with  $375\text{ }\mu\text{W/channel}$  power consumption.

A small experiment was setup to measure the efficiency and the time resolution for  $511\text{ keV}$  photons from a  $^{22}\text{Na}$  source. Approximately 0.19% efficiency for the annihilation photons from the  $\beta^+$  decay was measured, which is in good agreement with Monte Carlo simulations within errors. A  $70\text{ ps}$  time resolution with  $160\text{ }\mu\text{W/channel}$  power consumption was measured, which was limited by the modulation in the time-over-threshold distributions of this prototype that affected the time walk correction.

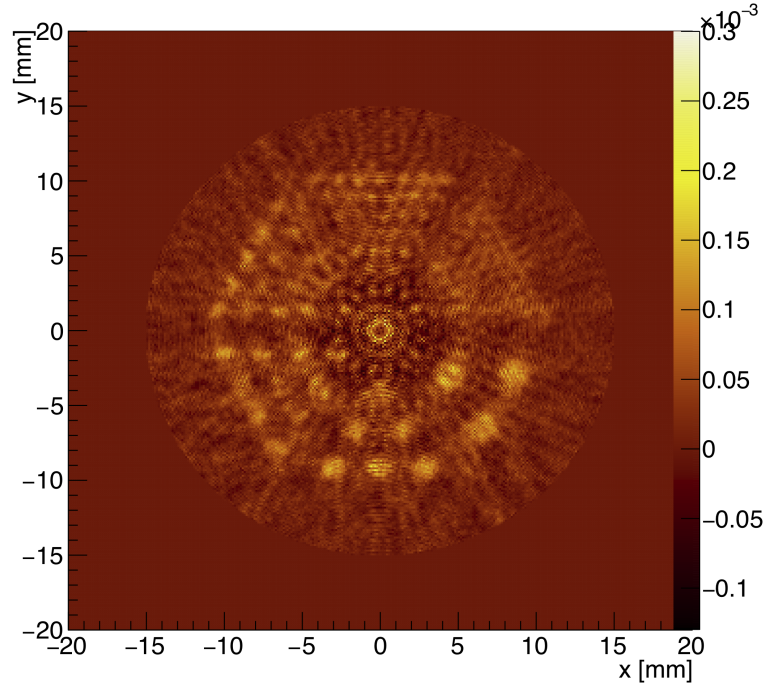
# Appendices



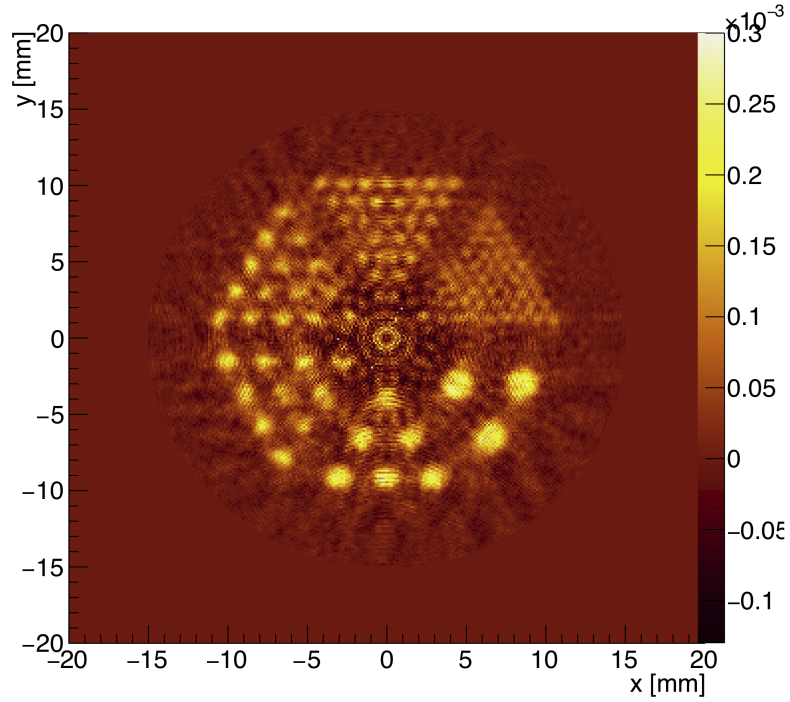
## Appendix A

# Analytical Image Reconstruction

Figure A.1 shows the images reconstructed from the data obtained in hit processing in a filtered back projection (FBP) model [20]. The FBP model analytically reconstructs the image with Fourier transformation and it has an advantage of fast computing. However, the artifacts can be seen in the center of the reconstructed images since the acceptance of the TT-PET scanner is not uniform for the radial direction.



(a) FBP reconstruction without TOF information



(b) FBP reconstruction with TOF information

Figure A.1: Analytical image reconstruction of Derenzo phantom at the center along the axial FOV without TOF information (a) and with TOF information (b). The diameter of the rods are 0.5, 0.7, 1.0, 1.2, 1.5, 2 mm. Artifacts can be seen in both reconstructed images due to the acceptance of the scanner.



## Appendix B

Simulation results of the tagged  
efficiency (ratio) with horizontal  
positions

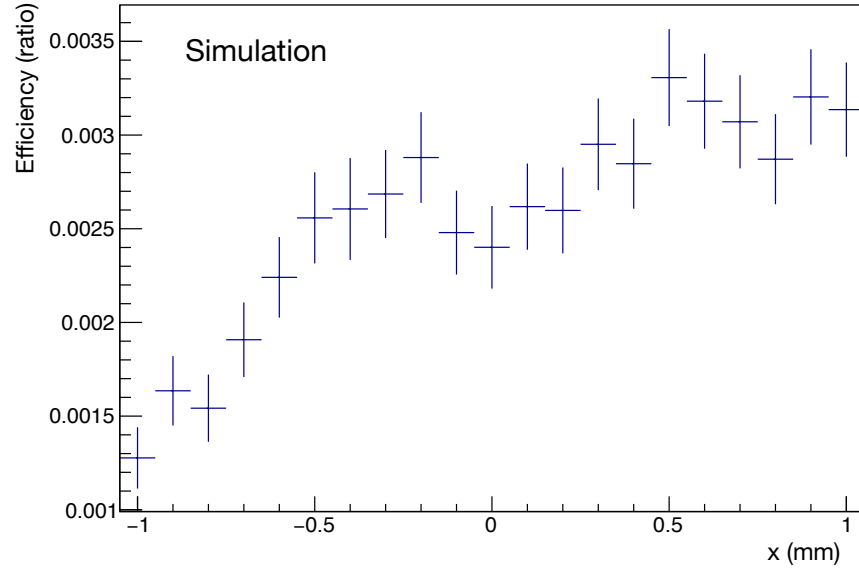


Figure B.1: Simulation result of the annihilation photon detection efficiency with different position along x-axis.

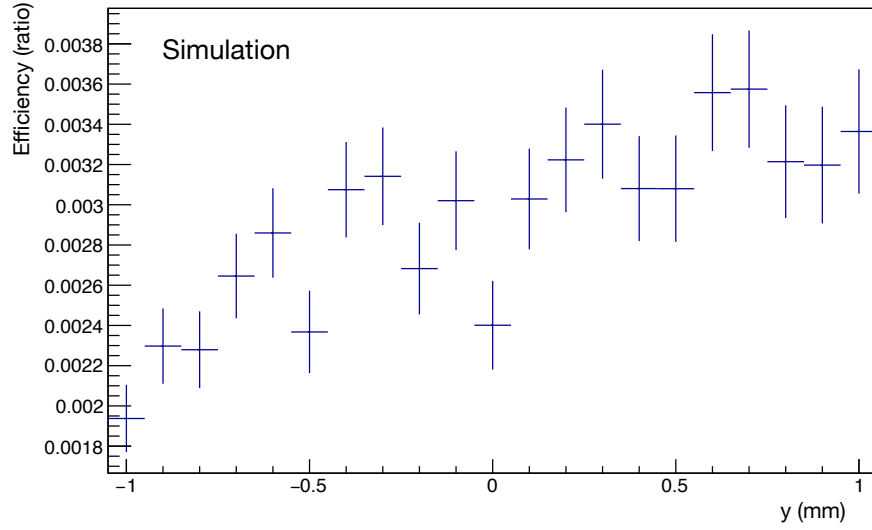


Figure B.2: Simulation result of the annihilation photon detection efficiency with different position along y-axis.

# Bibliography

- [1] Sanjiv Sam Gambhir. “Molecular imaging of cancer with positron emission tomography”. In: *Nature Reviews Cancer* 2.9 (2002), p. 683.
- [2] R. Duara et al. “Positron emission tomography in Alzheimer’s disease”. In: *Neurology* 36.7 (1986), pp. 879–879. ISSN: 0028-3878. DOI: 10.1212/WNL.36.7.879. eprint: <https://n.neurology.org/content/36/7/879.full.pdf>. URL: <https://n.neurology.org/content/36/7/879>.
- [3] Thomas Beyer et al. “A combined PET/CT scanner for clinical oncology”. In: *Journal of nuclear medicine* 41.8 (2000), pp. 1369–1379.
- [4] Martin S Judenhofer et al. “Simultaneous PET-MRI: a new approach for functional and morphological imaging”. In: *Nature medicine* 14.4 (2008), p. 459.
- [5] Andreas Boss et al. “Hybrid PET/MRI of intracranial masses: initial experiences and comparison to PET/CT”. In: *Journal of Nuclear Medicine* 51.8 (2010), pp. 1198–1205.
- [6] SC Strother, ME Casey, and EJ Hoffman. “Measuring PET scanner sensitivity: relating countrates to image signal-to-noise ratios using noise equivalents counts”. In: *Ieee transactions on nuclear science* 37.2 (1990), pp. 783–788.
- [7] Maurizio Conti. “State of the art and challenges of time-of-flight PET”. In: *Physica Medica* 25.1 (2009), pp. 1–11.
- [8] William W Moses. “Fundamental limits of spatial resolution in PET”. In: *Nuclear Instruments and Methods in Physics Research Section A: Accelerators, Spectrometers, Detectors and Associated Equipment* 648 (2011), S236–S240.
- [9] Craig S Levin and Edward J Hoffman. “Calculation of positron range and its effect on the fundamental limit of positron emission tomography system spatial resolution”. In: *Physics in Medicine & Biology* 44.3 (1999), p. 781.
- [10] Simon R Cherry, James A Sorenson, and Michael E Phelps. *Physics in nuclear medicine e-Book*. Elsevier Health Sciences, 2012.

- [11] TT-PET project, SNSF grant CRSII2-160808.
- [12] Didier Ferrere et al. “Module concept and thermo-mechanical studies of the silicon-based TT-PET small-animal scanner”. In: *arXiv preprint arXiv:1812.00788* (2018).
- [13] Kálmán Nagy et al. “Performance evaluation of the small-animal nanoScan PET/MRI system”. In: *Journal of Nuclear Medicine* 54.10 (2013), pp. 1825–1832.
- [14] Y Bandi et al. “The TT-PET Data Acquisition and Trigger System”. In: *arXiv preprint arXiv:1812.03958* (2018).
- [15] Albert X. Widmer and Peter A. Franaszek. “A DC-balanced, partitioned-block, 8B/10B transmission code”. In: *IBM Journal of research and development* 27.5 (1983), pp. 440–451.
- [16] Andrew L Goertzen et al. “NEMA NU 4-2008 comparison of preclinical PET imaging systems”. In: *Journal of Nuclear Medicine* 53.8 (2012), pp. 1300–1309.
- [17] Giuseppe Battistoni et al. “The FLUKA code: Description and benchmarking”. In: *AIP Conference proceedings*. Vol. 896. 1. AIP. 2007, pp. 31–49.
- [18] Emanuele Ripiccini et al. “Expected performance of the TT-PET scanner”. In: *arXiv preprint arXiv:1811.12381* (2018).
- [19] Sea Agostinelli et al. “GEANT4—a simulation toolkit”. In: *Nuclear instruments and methods in physics research section A: Accelerators, Spectrometers, Detectors and Associated Equipment* 506.3 (2003), pp. 250–303.
- [20] Lawrence A Shepp and Benjamin F Logan. “The Fourier reconstruction of a head section”. In: *IEEE Transactions on nuclear science* 21.3 (1974), pp. 21–43.
- [21] Thibaut Merlin et al. “CASToR: a generic data organization and processing code framework for multi-modal and multi-dimensional tomographic reconstruction”. In: *Physics in Medicine & Biology* 63.18 (2018), p. 185005.
- [22] Leonardo Dagum and Ramesh Menon. “OpenMP: An industry-standard API for shared-memory programming”. In: *Computing in Science & Engineering* 1 (1998), pp. 46–55.
- [23] Lawrence A Shepp and Yehuda Vardi. “Maximum likelihood reconstruction for emission tomography”. In: *IEEE transactions on medical imaging* 1.2 (1982), pp. 113–122.

- [24] Peter M Joseph. “An improved algorithm for reprojecting rays through pixel images”. In: *IEEE transactions on medical imaging* 1.3 (1982), pp. 192–196.
- [25] Finbarr O’Sullivan et al. “A statistical perspective on ill-posed inverse problems”. In: *Statistical science* 1.4 (1986), pp. 502–518.
- [26] Peter J Green. “Bayesian reconstructions from emission tomography data using a modified EM algorithm”. In: *IEEE transactions on medical imaging* 9.1 (1990), pp. 84–93.
- [27] Tom Hebert and Richard Leahy. “A generalized EM algorithm for 3-D Bayesian reconstruction from Poisson data using Gibbs priors”. In: *IEEE transactions on medical imaging* 8.2 (1989), pp. 194–202.
- [28] Charles Bouman and Ken Sauer. “A generalized Gaussian image model for edge-preserving MAP estimation”. In: *IEEE Transactions on image processing* 2.3 (1993), pp. 296–310.
- [29] Patrick Hallen et al. “PET performance evaluation of the small-animal Hyperion IID PET/MRI insert based on the NEMA NU-4 standard”. In: *Biomedical physics & engineering express* 4.6 (2018), p. 065027.
- [30] Negar Omidvari et al. “PET performance evaluation of MADPET4: a small animal PET insert for a 7 T MRI scanner”. In: *Physics in Medicine & Biology* 62.22 (2017), p. 8671.
- [31] Greg Stortz et al. “Performance of a PET insert for high-resolution small-animal PET/MRI at 7 tesla”. In: *Journal of Nuclear Medicine* 59.3 (2018), pp. 536–542.
- [32] Guen Bae Ko et al. “Evaluation of a silicon photomultiplier PET insert for simultaneous PET and MR imaging”. In: *Medical physics* 43.1 (2016), pp. 72–83.
- [33] Canali Jacoboni et al. “A review of some charge transport properties of silicon”. In: *Solid-State Electronics* 20.2 (1977), pp. 77–89.
- [34] RJ McIntyre. “A new look at impact ionization-Part I: A theory of gain, noise, breakdown probability, and frequency response”. In: *IEEE Transactions on Electron Devices* 46.8 (1999), pp. 1623–1631.
- [35] Simon M Sze and Kwok K Ng. *Physics of semiconductor devices*. John wiley & sons, 2006.

- [36] Nicolo Cartiglia et al. “Design optimization of ultra-fast silicon detectors”. In: *Nuclear Instruments and Methods in Physics Research Section A: Accelerators, Spectrometers, Detectors and Associated Equipment* 796 (2015), pp. 141–148.
- [37] W. Riegler and G. Aglieri Rinella. “Time resolution of silicon pixel sensors”. In: *Journal of Instrumentation* 12.11 (2017), P11017–P11017. ISSN: 17480221. DOI: 10.1088/1748-0221/12/11/P11017. arXiv: 1706.04883. URL: <http://stacks.iop.org/1748-0221/12/i=11/a=P11017?key=crossref.27fe13c5ffc88024a2f8cbcdec5488cd>.
- [38] William Shockley. “Currents to conductors induced by a moving point charge”. In: *Journal of applied physics* 9.10 (1938), pp. 635–636.
- [39] Simon Ramo. “Currents induced by electron motion”. In: *Proceedings of the IRE* 27.9 (1939), pp. 584–585.
- [40] Roberto Cardarelli et al. “PLL-less TDC & synchronisation system”. Pat. Europe Patent EP 18181123.3. 2 July 2018.
- [41] Emilio Gatti and Pier Francesco Manfredi. “Processing the signals from solid-state detectors in elementary-particle physics”. In: *La Rivista del Nuovo Cimento (1978-1999)* 9.1 (1986), pp. 1–146.
- [42] H. Rucker et al. “A 0.13  $\mu\text{m}$  SiGe BiCMOS technology featuring  $f_T/f_{\text{max}}$  of 240/330 GHz and gate delays below 3 ps”. In: *2009 IEEE Bipolar/BiCMOS Circuits and Technology Meeting*. 2009, pp. 166–169. DOI: 10.1109/BIPOL.2009.5314251.
- [43] P. Valerio et al. “A high-Precision Timing ASIC for TOF-PET Applications”. In: *Topical Workshop on Electronics for Particle Physics (TWEPP-17)*. Vol. 313. DOI: 10.22323/1.313.0043.
- [44] P Delpierre. “A history of hybrid pixel detectors, from high energy physics to medical imaging”. In: *Journal of Instrumentation* 9.05 (2014), p. C05059.
- [45] Sentaurus User’s Manual and I Version. “Synopsys”. In: *Inc., Mountain View, CA* 2009 (2010).
- [46] R Stratton. “Diffusion of hot and cold electrons in semiconductor barriers”. In: *Physical Review* 126.6 (1962), p. 2002.
- [47] WTRW Shockley and WT Read Jr. “Statistics of the recombinations of holes and electrons”. In: *Physical review* 87.5 (1952), p. 835.
- [48] Re N Hall. “Electron-hole recombination in germanium”. In: *Physical review* 87.2 (1952), p. 387.

- [49] JW Slotboom and HC De Graaff. “Measurements of bandgap narrowing in Si bipolar transistors”. In: *Solid-State Electronics* 19.10 (1976), pp. 857–862.
- [50] Guido Masetti, Maurizio Severi, and Sandro Solmi. “Modeling of carrier mobility against carrier concentration in arsenic-, phosphorus-, and boron-doped silicon”. In: *IEEE Transactions on electron devices* 30.7 (1983), pp. 764–769.
- [51] Narain D Arora, John R Hauser, and David J Roulston. “Electron and hole mobilities in silicon as a function of concentration and temperature”. In: *IEEE Transactions on electron devices* 29.2 (1982), pp. 292–295.
- [52] Ivan Perić et al. “High-voltage pixel detectors in commercial CMOS technologies for ATLAS, CLIC and Mu3e experiments”. In: *Nuclear Instruments and Methods in Physics Research Section A: Accelerators, Spectrometers, Detectors and Associated Equipment* 731 (2013), pp. 131–136.
- [53] H. F.-W. Sadrozinski et al. “Ultra-fast silicon detectors”. In: *Nuclear Instruments and Methods in Physics Research Section A: Accelerators, Spectrometers, Detectors and Associated Equipment* 730 (2013), pp. 226–231. ISSN: 0168-9002. DOI: 10.1016/J.NIMA.2013.06.033.
- [54] M. Benoit et al. “The FE-I4 telescope for particle tracking in testbeam experiments”. In: *Journal of Instrumentation* 11.07 (2016), P07003–P07003. ISSN: 1748-0221. DOI: 10.1088/1748-0221/11/07/P07003.
- [55] M. Benoit et al. “100 ps time resolution with thin silicon pixel detectors and a SiGe HBT amplifier”. In: *Journal of Instrumentation* 11.3 (2016), P03011–P03011. ISSN: 17480221. DOI: 10.1088/1748-0221/11/03/P03011.